Doctoral Thesis

MONOLITHICALLY INTEGRATED, PRINTED SOLID-STATE RECHARGEABLE BATTERIES WITH AESTHETIC VERSATILITY

Keun-Ho Choi

Department of Energy Engineering

(Battery Science and Technology)

Graduate School of UNIST

2017

MONOLITHICALLY INTEGRATED, PRINTED
SOLID-STATE
RECHARGEABLE BATTERIES
WITH AESTHETIC VERSATILITY

Keun-Ho Choi

Department of Energy Engineering

(Battery Science and Technology)

Graduate School of UNIST

MONOLITHICALLY INTEGRATED, PRINTED SOLID-STATE RECHARGEABLE BATTERIES WITH AESTHETIC VERSATILITY

A thesis/dissertation

submitted to the Graduate School of UNIST

in partial fulfillment of the

requirements for the degree of

Doctor of Philosophy

Keun-Ho Choi

06. 13. 2017

Approved by
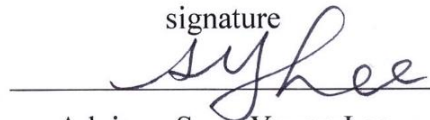
_____

Advisor

Sang-Young Lee

MONOLITHICALLY INTEGRATED, PRINTED
SOLID-STATE
RECHARGEABLE BATTERIES
WITH AESTHETIC VERSATILITY

Keun-Ho Choi

This certifies that the thesis/dissertation of Keun-Ho Choi is approved.
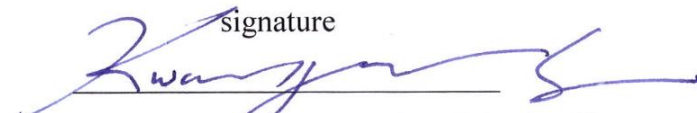
06/13/2017

signature

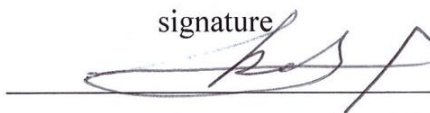Advisor: Sang-Young Lee

signature
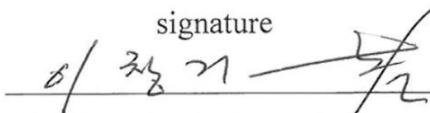
Soojin Park: Thesis Committee Member #1

signature

Kwanyong Seo: Thesis Committee Member #2

signature

Chang Hyun Kim: Thesis Committee Member #3

signature

Chang Kee Lee: Thesis Committee Member #4

Contents

Abstract

With the advent of flexible/wearable electronics and Internet of Things (IoT) which are expected to drastically change our daily lives, printed electronics has drawn much attention as a low cost, efficient, and scalable platform technology. The printed electronics requires so-called "printed batteries" as a monolithically integrated power source that can be prepared by the same printing processes. The printing technology is a facile and reproducible process in which slurries or inks are deposited to make pre-defined patterns. The slurries/inks should be designed to fulfill requirements (such as rheology and particle dispersion) of the printing process. Development of printed batteries involves the design and fabrication of battery component slurries/inks. Most studies of the printed batteries have been devoted to the development of printed electrodes. However, in order to reach an ultimate goal of so-called "all-printed-batteries", printed separator membranes and printed electrolytes should be also developed along with the printed electrodes.

The objective of the research presented in this dissertation is to develop materials and printing-based strategies to fabricate a new class of monolithically integrated, printed solid-state rechargeable batteries with aesthetic versatility to address the aforementioned formidable challenges, with particular attention to comprehensive understanding of colloidal microstructure and rheological/electrochemical properties of printable battery component slurries/inks. Colloidal microstructure of the battery component slurries/inks is expected to play a viable role in realizing the monolithically integrated printed batteries, as it can significantly affect fluidic characteristics of the slurries/inks and also electrochemical properties. In particular, our interest is devoted to concentrated colloidal gels that exhibit thixotropic fluid behavior (i.e., they readily flow upon being subjected to external stress and quickly return to a quiescent state). Driven by such unique viscoelastic response, the slurries/inks show good dimensional stability and shape diversity on various objects. In addition to the viscoelasticity control of the slurries/inks, the interaction between colloidal conductive particles should be carefully tuned in order to secure facile ion and electron transport pathways. When the attractive interaction is dominant, the colloidal particles tend to be aggregated in disordered and dynamically arrested forms, yielding the highly reticulated three-dimensional networks. In an electrochemical system, these interconnected conductive particle networks act as electron conduction channels while the interstitial voids formed between the particle networks allows ion transport.

In this dissertation, as a proof-of-concept, lithium-ion batteries (LIBs), electric double layer capacitors (EDLCs), and Zn-air batteries are chosen to explore the feasibility of this approach. The resultant solid-state printed batteries are fabricated through various printing processes such as stencil printing, inkjet printing, and pen-based writing. Notably, the printed batteries can be seamlessly integrated with objects or electronic devices, thus offering unprecedented opportunities in battery design and form factors that lie far beyond those achievable with conventional battery technologies.

List of figures

Figure 13. Rheological properties of LFP cathode suspension (LFP/carbon black additive/SCE matrix precursor = 38/4/58 (w/w/w): (a) viscosity; (b) storage modulus (G') and loss modulus (G"). Rheological properties of LTO anode suspension (LTO/carbon black additive/SCE matrix precursor = 27/7/66 (w/w/w): (c) viscosity; (d) G' and G".

Figure 14. Rheological properties (viscosity and viscoelasticity): (a) solid content (= 20 wt%); (b) solid content (= 42 wt%). (c) At higher solid content (= 50 wt%), a photograph showing the glass transition in the cathode suspension.

Figure 15. Morphological characterization (cross-sectional view) of (a) printable LFP cathode and (b) printable LTO anode: SEM images; EDS images.

Figure 16. Change in the FT-IR spectra of acrylic C=C double bonds of ETPTA before/after UV irradiation: (a) printable LFP cathode; (b) printable LTO anode.

Figure 17. (a) Photographs showing mechanical flexibility of printable electrodes upon physical deformation such as folding and winding (rod diameter = 5 mm). (b) Photographs of the LFP cathode slurry with solid content = 42% (upper image) and LFP cathode slurry with solid content = 20% (lower image). The LFP cathode slurry with lower solid content failed to maintain the letter form when it was tilted toward vertical position.

Figure 18. Major characteristics of printable SCE layers: (a) viscosity; (b) G' and G"; (c) mechanical flexibility; (d) temperature-dependent ionic conductivity.

Figure 19. Galvanostatic charge/discharge profiles as a fuction of cycle number, where the gravimetric charge/discharge capacity was estimated based on the mass of active materials: (a) a LFP

half cell (= printable LFP cathode/(1M LiPF$_6$ in EC/PC)-soaked PE separator/lithium metal anode); (b) a LTO half cell (= printable LTO anode/(1M LiPF$_6$ in EC/PC)-soaked PE separator/lithium metal anode).

Figure 21. (a) A SEM image (cross-sectional view) of a PRISS full cell (= printable LFP cathode (LFP/carbon black/SCE matrix = 38/4/58 w/w/w)/printable SCE layer (ETPTA/1M LiPF$_6$ in EC/PC/Al$_2$O$_3$ nanoparticles = 5/28/67 w/w/w)/printable LTO anode (LTO/carbon black/SCE matrix = 27/7/66 w/w/w)), wherein the EC/PC-based liquid electrolyte was removed prior to the SEM analysis. (b) Galvanostatic charge/discharge profiles of a PRISS full cell as a function of cycle number. The cell was cycled between 1.0 and 2.5 V at a constant charge/discharge current density (= 0.05 C/0.05 C), where gravimetric charge/discharge capacity was estimated based on the mass of LFP active materials. (c) SEM images (cross-sectional view) of the printable electrodes after the cycling test (30 cycles).

Figure 21. A photograph showing direct fabrication of a PRISS cell on paper-made eyeglasses. The PRISS cell-unitized wearable eyeglasses operated a LED lamp.

Figure 22. A photograph showing direct fabrication of a heart-shaped PRISS cell on a transparent glass cup with curvilinear surface. The PRISS cell, under being mounted on the round-shaped glass cup, delivered normal charge/discharge behavior (at charge/discharge current density of 0.05 C/0.05 C under voltage range of 1.0 - 2.5 V, gravimetric charge/discharge capacity was estimated based on the mass of LFP active materials).

Figure 22. (a) Digital photograph (front) of SiPV-LIB device featuring a monolithic tandem cell configuration. Inset shows the back of the SiPV-LIB device. (b) Schematic representation of the internal structure and operating principle of the SiPV-LIB device under sunlight illumination.

Figure 23. A photograph of "PRISS" letters-shaped PRISS cell (left side) and its charge/discharge profiles at charge/discharge current density of 0.05 C/0.05 C under voltage range of 1.0 - 2.5 V (right side, gravimetric charge/discharge capacity was estimated based on the mass of LFP active materials), which were measured under being completely wound along the rods having different diameters (= 5, 10, 15 mm), not a planar configuration.

Figure 24. (a) Digital photograph (front) of SiPV-LIB device featuring a monolithic tandem cell configuration. Inset shows the back of the SiPV-LIB device. (b) Schematic representation of the internal structure and operating principle of the SiPV-LIB device under sunlight illumination.

Figure 25. (a) Schematic illustration of the printing-based stepwise fabrication of the solid-state bipolar LIB cell directly on a c-Si PV module. (b, c) Cross-sectional SEM images of 2-stack bipolar LIB cell (b) and seamlessly unitized interface between bipolar LIB cell and c-Si PV module (c). (d) Galvanostatic charge/discharge profiles of 1-stack (grey lines) and 2-stack (blue lines) LIB cells. (e) OCV profiles of the SiPV-LIB device and bare bipolar LIB cell as a function of elapsed time. (f) Galvanostatic charge/discharge profiles of bipolar LIB cell in SiPV-LIB device as a function of the cycle number at a constant charge/discharge current density of 1.0 C/1.0 C.

Figure 26. Assembly of high-voltage compact c-Si PV module. (a) Schematic illustration of transfer-free c-Si PV module assembly using UV-curable polymer and adhesive tapes. (b) Digital photograph (backside) of the compact c-Si PV module showing the interconnection of 25 solar cells in series. (c) Optical microscopy image (red square region in Fig. 2b) showing the interconnected solar cells formed by the thermally deposited Al film. (d) Voltage (black line) and power (blue line) of compact c-Si PV module as a function of the number of mini-cells.

Figure 27. (a) Equivalent circuit of the SiPV-LIB device upon photo-charging/galvanostatic discharging. (b) Photo-charge/galvanostatic discharge profiles of the SiPV-LIB device, where the SiPV-LIB device was photo-charged from 3.0 to 5.4 V for 45 sec under a light intensity of 100 mW cm^{-2} (1 Sun) and was galvanostatically discharged to 3 V at a discharge current rate of 1.0 C (= 0.5 mA cm^{-2}). (c) Photo-charge/galvanostatic discharge cycling performance (expressed by the capacity retention (black line with hollow circle) and photo-electric conversion/storage efficiency (blue line with filled circles)) of SiPV-LIB device under a light intensity of 100 mW cm^{-2} (1 Sun) and a discharge current rate of 1.0 C (= 0.5 mA cm^{-2}). Inset shows photo-charge/galvanostatic discharge profiles with repeated cycling.

Figure 28. (a) Photo-charge capacity (black line with hollow circles) and photo-electric conversion/storage efficiency (blue solid line with filled circles) of the SiPV-LIB device as a function of photo-charging time. (b) Comparison of photo-electric conversion/storage efficiencies between this work (the SiPV-LIB device) and previously reported PV-battery systems with similar single-unit architectures (organic solar cell (OPV)-supercapacitor[24], DSSC-LIB[20], and DSSC-supercapacitor[14-16,18,19,27,52]).

Figure 29. (a) Digital photograph showing the operation of the SiPV-LIB-embedded smartcard. Inset shows the overall thickness of the resulting smartcard. (b) Galvanostatic

discharge rate capability of the SiPV-LIB device (after photo-charging for 120 sec under a light intensity of 100 mW cm^{-2}) over a wide range of discharge current densities from 0.5 to 5.0 C. (c) Photo-charging/galvanostatic discharging profiles of SiPV-LIB devices at a fixed discharge current rate of 1.0 C as a function of light intensity (8, 40, and 100 mW cm^{-2}).

Figure 30. (a) Digital photographs showing the dimensional change of the SiPV-LIB device (with a focus on the LIB part) after it is placed in a hot oven for 1 h with the temperature varied from 60 to 120°C. (b) Capacity retention of SiPV-LIB device with cycling as a function of temperature under a light intensity of 100 mW cm^{-2} and a discharge current rate of 1.0 C.

Figure 31. (a) Galvanostatic discharge profiles of the SiPV-LIB device as a function of discharge current density (28, 30, 48, and 60 C). Inset shows the discharge profiles of the SiPV-LIB device in the dark environment. (b) Internal resistances ($R_{internal}$) of LIB cells in SiPV-LIB devices under sunlight illumination (red line) and in the dark environment (black line).

Figure 32. Volumetric (a) and Gravimetric (b) ragone plots of SiPV-LIB devices under sunlight illumination (red line) and in the dark environment (black line). The EV target goal announced by the US Department of Energy[46] is marked by the star symbol.

Figure 33. Digital photograph showing a smartphone (a) and MP3 player (b) that are being charged by the SiPV-LIB device under sunlight illumination.

Figure 34. (a) Schematic illustration depicting the architectural uniqueness of the inkjet-printed SCs, wherein the cell components were consecutively inkjet-printed in a layered configuration. (b) Effect of substrates on the resolution of the inkjet printing process: wetting substrate (left upper side, random spreading of ink droplets), non-wetting substrate (left lower side, coffee-ring formation), and CNF nanomat on A4 paper (right side, high-resolution print pattern).

Figure 35. Apparent viscosity (η, measured at a shear rate of 1 s^{-1}) of the CNF suspension solution as a function of CNF concentration, where the insets are a photograph and TEM image of the CNF suspension solution.

Figure 36. Schematics and SEM images of the stepwise fabrication procedure of the CNF nanomat-based primer layer: (a) A4 paper, (b) inkjet-printed (wet-state) CNF layer deposited on A4 paper, (c) inkjet-printed CNF nanomat deposited onto A4 paper. The highly developed nanoporous structure was generated after the solvent exchange between ethanol/acetone mixture and water.

Figure 37. 3D laser scanning microscope images of: (a) CNF nanomat-based primer layer (R_a (surface roughness) ~ 0.4 µm); (b) A4 paper (wetting substrate, R_a (surface roughness) ~ 4.8 µm); (c) PET film (non-wetting substrate, R_a ~ 0.2 µm).

Figure 38. (a) Variation in the water contact angles of different substrates with time. (b) SEM images (surface view) of the inkjet-printed ((SWNT/AC) + Ag NWs) electrodes on different substrates. (c) SEM image (cross-sectional view) showing the preferential deposition of the ((SWNT/AC) + Ag NWs) electrode onto the CNF-paper surface. (d) Electric resistances of the inkjet-printed ((SWNT/AC) + Ag NWs) electrodes on different substrates.

Figure 39. (a) Schematic illustration of the fabrication procedure of the inkjet-printed SC electrodes. The insets are the photographs of an electrochemically active ink (SWNT/AC in water) and an electrically conductive ink (Ag NWs in water/IPA = 1/1 (v/v)). (b) Photograph of the inkjet-printed, letter ("UNIST")-shaped electrodes of different sizes (ranging from centimeter to micrometer scale) on A4 paper.

Figure 40. (a) Schematic illustration depicting the CNT-assisted photonic sintering (i.e., interwelding) of Ag NWs. (b) SEM image of the inkjet-printed electrodes before (see the inset) and after the SWNT-assisted photonic sintering. (c) Electric resistances of the inkjet-printed electrode and control electrode (= AC + Ag NW) as a function of UV irradiation time. (d) Raman spectra of the inkjet-printed electrodes before/after the SWNT-assisted photonic sintering.

Figure 41. (a) Tape (using commercial Scotch tape) test and mechanical rubbing test of the inkjet-printed electrodes. (b) Variation in the relative electrical resistance (= R (electrical resistance upon bending deformation) / R_0 (electrical resistance before bending deformation)) of the inkjet-printed electrodes as a function of bending cycles with different bending radii (= 1.0, 3.0, and 5.0 mm). (c) Chemical stability of the inkjet-printed electrodes in various solvents (water, ethanol, and acetone).

Figure 42. (a) FT-IR spectra showing the change of characteristic peaks assigned to C=C double bonds of ETPTA, before/after the UV crosslinking reaction. (b) Linear sweep voltammetry (LSV) profile of [BMIM][BF$_4$]/ETPTA mixture (after removal of the residual water).

Figure 43. (a) Viscosity of the electrolyte ink ([BMIM][BF$_4$]/ETPTA = 85/15 (w/w) mixture in solvents, concentration = 10 wt%) as a function of shear rate. (b) Schematics and EDS images (red dots represent F elements of [BMIM][BF$_4$]) of the inkjet-printed solid-state electrolytes (ethanol (upper side) vs. water (lower side)). (c) Nyquist plots of the inkjet-printed solid-state electrolytes (ethanol vs. water). (d) TGA profile (dynamic mode, heating rate = 10 ^{o}C min^{-1} under nitrogen atmosphere) of the inkjet-printed ([BMIM][BF$_4$]/ETPTA) solid-state electrolyte.

Figure 44. Schematic illustration of the stepwise fabrication procedure of the inkjet-printed SCs, and a photograph of the desktop inkjet printer used herein.

Figure 45. (a) CV profiles (scan rate = 1.0 mV s^{-1}) of the inkjet-printed SCs with different dimensions (insets are their photographs). (b) Cycling performance of the inkjet-printed SC at a constant charge/discharge current density of 0.2 mA cm^{-2}. (c) CV profiles (scan rate = 1.0 mV s^{-1}) of the inkjet-printed SC after the repeated bending deformation (bending radius = 2.5 mm and 1,000 cycles). The inset shows the deformed state of the SC.

Figure 46. (a) Galvanostatic charge/discharge profiles (current density = 0.2 mA cm^{-2}) of the inkjet-printed SCs connected in series or parallel without the use of metallic interconnects. Schematics and photographs of the inkjet-printed SCs: (b) 5 cells connected in series and (c) 5 cells connected in parallel.

Figure 47. (a) Schematic and (b) photograph of the inkjet-printed, letter ("BATTERY")-shaped SC that was seamlessly connected with the inkjet-printed electrical circuit. (b) Charge/discharge profiles of the inkjet-printed, letter ("BATTERY")-shaped SC.

Figure 48. (a) Schematic and (b) photograph of the inkjet-printed, traditional Korean "Taegeuk" symbol-like SC (marked by a red circle) that was seamlessly connected with the inkjet-printed electrical circuits and a LED lamp. The inset is a photograph of the SC after

being placed on a hot plate (set at 150 °C) for 0.5 h. (c) Charge/discharge profiles of the inkjet-printed, "Taegeuk" symbol-like SC.

Figure 49. (a) Photograph of the inkjet-printed Korea map, wherein the inkjet-printed SCs (marked by red boxes) were seamlessly connected to LED lamps (marked by blue boxes) via the inkjet-printed electric circuits. (b) SEM image of the LED lamp connected to the inkjet-printed electric circuits. (c) CV profile (scan rate = 1.0 mV s^{-1}) of the inkjet-printed SC in the map.

Figure 50. (a) Photograph of the inkjet-printed, letter ("OR")-shaped SCs that were seamlessly connected to the letter ("HOT" and "COLD")-shaped electric circuits onto A4 paper. (b) Galvanostatic charge/discharge profile (current density = 1.0 mA cm^{-2}) of the inkjet-printed, letter ("OR")-shaped SCs that were composed of 4 cells connected in series. (c) Photograph depicting the operation of the blue LED lamp in the smart cup (for cold water (~ 10 °C)), wherein the inset is a photograph of a temperature sensor assembled with an Arduino board. (d) Photograph depicting the operation of the red LED lamp in the smart cup (for hot water (~ 80 °C)).

Figure 51. (a) Photograph of writable Zn-air batteries in two series connection to power a LED lamp mounted on the printed circuit, wherein the cell components were consecutively drawn in a layered configuration. (b) Schematic representation depicting the working principle of the writable Zn-air battery.

Figure 52. Photographs showing the stepwise fabrication procedure of writable Zn-air batteries in 2-series connection.

Figure 53. (a) Photograph of a rollerball pen loaded with a Zn anode ink, where the inset shows the rollerball pen tip during writing a Zn anode track. The background shows metallic Zn text directly written on A4 paper. (b) Optical microscope image demonstrating the dispersion state of Zn nanoparticles in the Zn anode ink. The Zn anode ink was composed of Zn nanoparticles, linseed oil as a carrier solvent and functional binder, and turpentine oil as a thinning agent.

Figure 54. Apparent viscosity (η, measured at a shear rate of 1 s^{-1}) of Zn anode inks as a function of Zn concentration.

Figure 55. Effect of adding wood turpentine oil as a shear-thinning medium on the rheological properties of the Zn anode ink: (a) viscosity; (b) moduli (G', G'').

Figure 56. Photograph showing the dispersion stability of the Zn anode ink, where the pen writing was performed after a month when stored in a sealed container.

Figure 57. (a) Schematic illustration of UV-curing mechanism of the Zn anode after writing was performed, where the linseed oil is susceptible to crosslinking under UV irradiation. (b) Fluorescence spectra of the written Zn anodes as a function of UV irradiation time. (c) Fluorescence mapping images of the written Zn anodes before (see the inset) and after UV irradiation.

Figure 58. (a) The mechanical rubbing test of the written Zn anodes before (see the inset) and after UV irradiation. (b) Photograph showing the water-repelling nature of the written Zn anodes. (c, d) SEM images (c) and photographs (d) showing the variation in the surface morphology of the UV-cured Zn anode and the uncured Zn anode (see the insets) after the high-humidity and high-temperature test (at 95% RH/80 $^{\circ}$C for 10 hr).

Figure 59. (a) Discharge profiles (current density = 1.0 mA cm^{-2}) of the writable Zn-air batteries before/after exposure to ambient conditions for a month. (b-c) The mechanical stability of the writable Zn-air batteries upon bending as a function of bending radii: (b) photographs; (c) discharge profiles at a discharge current density of 1.0 mA cm^{-2}.

Figure 60. (a) Discharge profiles (current density = 1.0 mA cm^{-2}) of the writable Zn-air batteries connected in series or parallel. (b) Photographs of the writable Zn-air batteries: (top) 2-cells in series connection; (bottom) 2-cells in parallel connection.

Figure 61. (a) Photograph of the electronic sketch of the light bulb, wherein the writable Zn-air batteries in 2-series connection (marked by a red box) were connected to a LED lamp via direct writing. (b) Discharge profile (current density = 1.0 mA cm^{-2}) of the 2-series connected Zn-air batteries in the electronic sketch.

Figure 62. (a) Photographs depicting the light sensing circuit integrated with the 3-series connected Zn-air batteries on the kirigami paper, where the inset is the opposite side; it does

show a seamless integration of electrical components with the kirigami paper. (b) Discharge profile (current density = 1.0 mA cm^{-2}) of the 3-series connected Zn-air batteries in the kirigami paper. (c) Photographs depicting the smart paper lamp that was off in the present of light. The kirigami paper integrated with the circuit was successfully transformed into the pre-designed 3D architecture to produce the smart paper lamp, while the inset shows that the paper cannot support its 3D structure when applying a conventional AAA-sized battery due to its higher mass. (d) Photograph depicting the operation of the smart paper lamp in the absence of the light illumination.

CHAPTER I. Introduction

1.1. Motivation

With the advent of flexible/wearable electronics and Internet of Things (IoT) which are expected to drastically change our daily lives, printed electronics has drawn much attention as a low cost, efficient, and scalable platform technology[1-3]. The printed electronics requires so-called "printed batteries" as a monolithically integrated power source that can be prepared by the same printing processes (Figure 1).
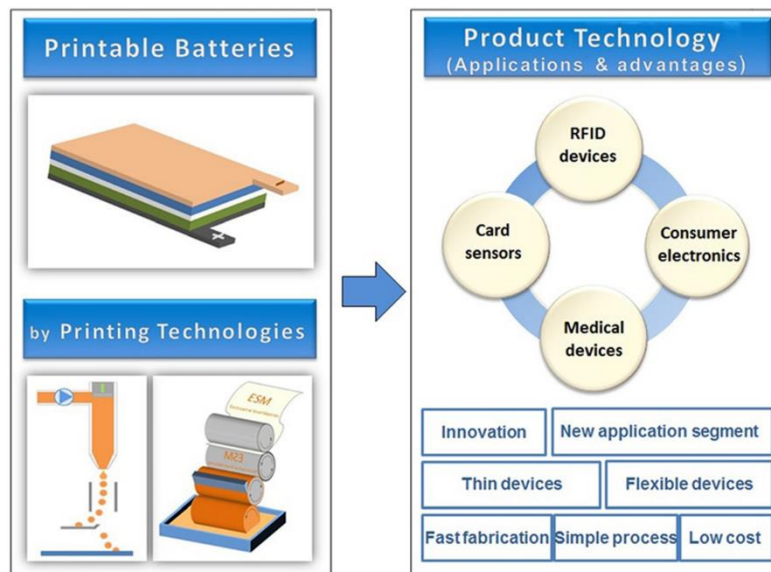
Figure 1. Schematic of printed battery architecture and printing technologies. Examples and features of printed battery-electronics integration are also described.

From the battery manufacturing point of view, conventional batteries with fixed shapes and sizes are generally fabricated by winding or stacking cell components (such as anodes, cathodes, and separator membranes) and then packaging them with (cylindrical-/rectangular-shaped) metallic anisters or pouch fimls, finally followed by injection of liquid electrolytes[3-4]. In particular, the use of liquid electrolytes gives rise to serious concerns in cell assembly because they require strict packaging materials to avoid leakage problems and also separator membranes to prevent electrical contact between electrodes. For these reasons, the conventional battery materials and assembly processes have pushed the batteries to lack of variety in form factors, thus imposing formidable challenges on their integration into versatile-shaped electronic devices. In contrast, the printed batteries are thinner, lighter, and can be easily produced through a variety of cost-effective printing processes[4]. More importantly, they offer unprecedented opportunities in diversifying battery design, dimension, and form factors, which lie far beyond those achievable with conventional battery technologies.

The printing technology is a facile and reproducible process in which slurries or inks are

deposited to make pre-defined patterns[4-5]. The slurries/inks should be designed to fulfill requirements (such as rheology and particle dispersion) of the printing process. Development of printed batteries involves the design and fabrication of battery component slurries/inks. Most studies of the printed batteries have been devoted to the development of printed electrodes. However, in order to reach an ultimate goal of so-called "all-printed-batteries", printed separator membranes and printed electrolytes should be also developed along with the printed electrodes.

1.2. Objectives and Strategies

The objective of the research presented in this dissertation is to develop materials and printing-based strategies to fabricate a new class of monolithically integrated, printed solid-state rechargeable batteries with aesthetic versatility to address the aforementioned formidable challenges, with particular attention to comprehensive understanding of colloidal microstructure and rheological/electrochemical properties of printable battery component slurries/inks. Colloidal microstructure of the battery component slurries/inks is expected to play a viable role in realizing the monolithically integrated printed batteries, as it can significantly affect fluidic characteristics of the slurries/inks and also electrochemical properties. In particular, our interest is devoted to concentrated colloidal gels that exhibit thixotropic fluid behavior (i.e., they readily flow upon being subjected to external stress and quickly return to a quiescent state). Driven by such unique viscoelastic response, the slurries/inks show good dimensional stability and shape diversity on various objects. In addition to the viscoelasticity control of the slurries/inks, the interaction between colloidal conductive particles should be carefully tuned in order to secure facile ion and electron transport pathways. When the attractive interaction is dominant, the colloidal particles tend to be aggregated in disordered and dynamically arrested forms, yielding the highly reticulated three-dimensional networks. In an electrochemical system, these interconnected conductive particle networks act as electron conduction channels while the interstitial voids formed between the particle networks allows ion transport.

In this dissertation, as a proof-of-concept, lithium-ion batteries (LIBs), electric double layer capacitors (EDLCs), and Zn-air batteries are chosen to explore the feasibility of this approach. The resultant solid-state printed batteries are fabricated through various printing processes such as stencil printing, inkjet printing, and pen-based writing. Notably, the printed batteries can be seamlessly integrated with objects or electronic devices, thus offering unprecedented opportunities in battery design and form factors that lie far beyond those achievable with conventional battery technologies.

1.3.   References

(1) S. H. Kim, K. H. Choi, S. J. Cho, S. Choi, S. Park, S. Y. Lee, *Nano Lett.* **2015**, *15*, 5168.

(2) K.-H. Choi, J. Yoo, C. K. Lee, S.-Y. Lee, *Energy Environ. Sci.* **2016**, *9*, 2812.

(3) A. M. Gaikwad, A. C. Arias, D. A. Steingart, *Energy Technol.* **2015**, *3*, 305.

(4) R. E. Sousa, C. M. Costa, S. Lanceros-Mendez, *ChemSusChem* **2015**, *8*, 3539.

(5) D. Tian, Y. Song, L. Jiang, *Chem. Soc. Rev.* **2013**, *42*, 5184.

CHAPTER II. Backgrounds on Printed Batteries

2.1. Printing Techniques

2.1.1. Stencil Printing

Stencil printing is an on-contact process where a pre-patterned metal or plastic mask is placed in contact with the substrate[1]. A squeegee is dragged across the ink over the mask to remove the excess ink (Figure 2). The stencil is removed from the substrate and the ink is left on the substrate. The concentration of the ink or the thickness of the mask can be adjusted to change the resulting film thickness.
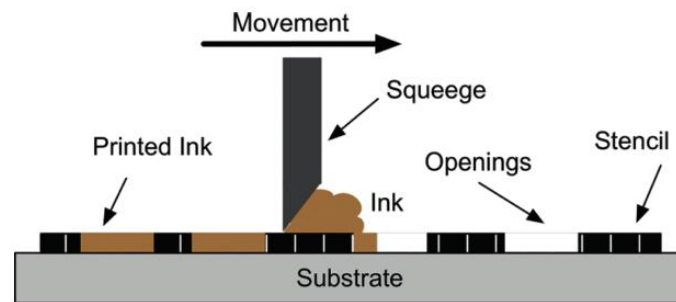
Figure 2. Schematic of the stencil printing process.

2.1.2. Screen Printing

Screen printing is commonly used to deposit ink materials, such as inks for T-shirts and logos. The screen printing process allows for the deposition of multiple layers[1]. In the screen printing technique, a screen with meshes of various sizes is filled with an ink. The ink used for screen printing has a high viscosity (1,000-50,000 cP) and low volatility. A squeegee is dragged across the screen surface to transfer the ink from the screen to the substrate (Figure 3). As the squeegee moves across the screen, the ink is squeezed out of the mesh by capillary action onto the substrate. The film thickness is determined by the ink properties and mesh size.
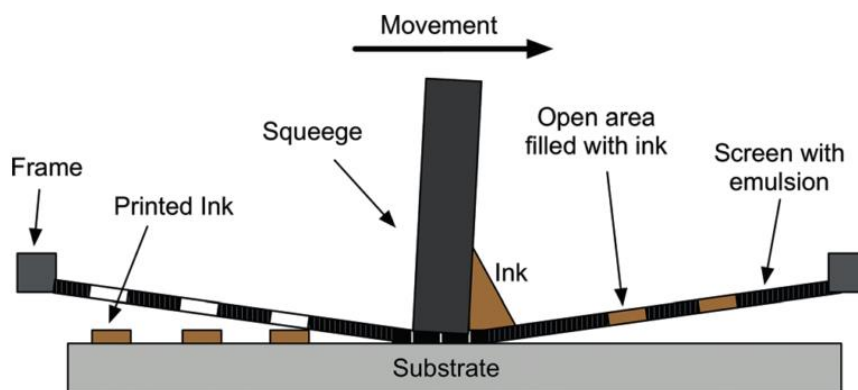
Figure 3. Schematic of the screen printing process.

2.1.3. Inkjet Printing

Inkjet is a digital printing using which the desired image can be printed by dropping ink droplets onto the substrate (Figure 4)[1]. Inkjet requires inks of relatively low viscosity (2-30 cP) to be printable. The ultimate feature size is dependent on the ink properties, printing technique, surface properties, printhead and substrate temperatures[2]. For example, smaller features can be made by tuning the surface properties of the substrate, such as making areas hydrophobic or hydrophilic to control wetting of the ink on the substrate.
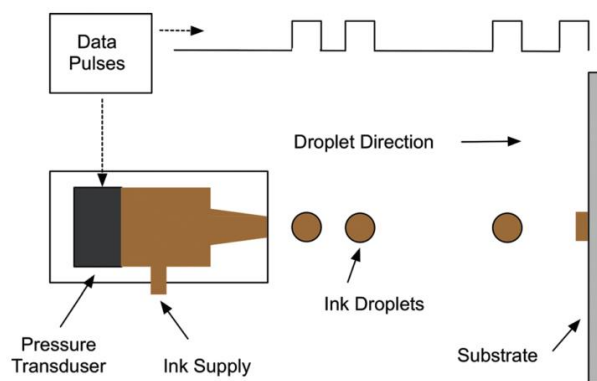
Figure 4. Schematic of the inkjet printing process.

2.1.4. Extrusion Printing

Extrusion printing or direct write pneumatic dispenser printing is a printing technique that is used to print relatively thick films[1,3]. Extrusion printing or flow-based printing uses a pneumatic-controlled injector to create a positive pressure to dispense ink through a syringe needle (Figiure 5). This technique is capable of printing feature sizes of 50 µm and film thicknesses of 10-100 µm. The feature size is determined by the needle size, the ink properties and the print spacing. The inner diameter of the syringe needle can be chosen down to 100 µm, and smaller diameter needles can be made by pulling borosilicate glass.   The ink, or slurries, can have high viscosities ranging from 5 to 1,000,000 cp and can contain material that has large particle sizes, for example, on the order of 1-20 µm. The slurries are typically a suspension consisting of the material one wishes to deposit, the solvent and filling materials such as polymers.
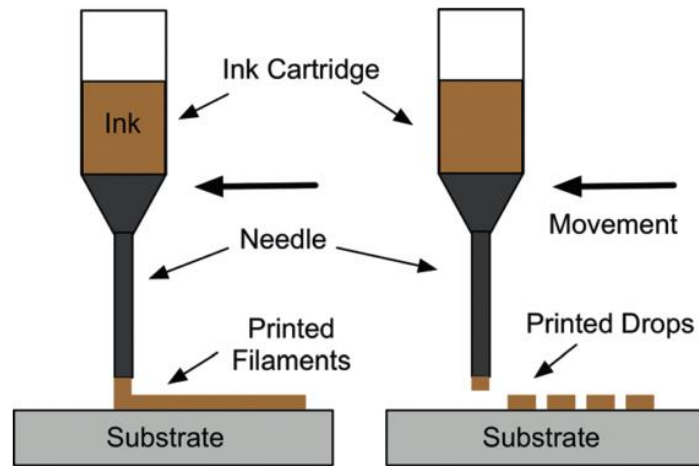
Figure 5. Schematic of the dispenser printing process.

2.2. Colloidal Suspensions/Inks

2.2.1. Interparticle Forces

Colloidal suspensions can be prepared in the dispersed, weakly flocculated, or strongly flocculated states[4], as shown schematically in Figure 6. In the dispersed state, discrete particles that exist in the suspension repel one another on close approach. In the weakly flocculated state, particles aggregate in a shallow secondary minimum, forming isolated clusters (or flocs) in suspension at volume fractions below the gel point or a particle network at higher volume fractions. In this case, an equilibrium separation distance exists between aggregated particles. In contrast, particles aggregate into a deep primary minimum in the strongly flocculated (or coagulated) state, forming either a touching particle network or individual clusters in suspension, depending on their concentration. Colloidal stability is governed by the total interparticle potential energy, *Vtotal*, which can be expressed as

$$V_{total} = V_{vdW} + V_{electrostatic} + V_{steric} + V_{structural} \qquad (1)$$

where V_{vdW} is the attractive potential energy due to long-range van der Waals interactions between particles, $V_{electrostatic}$ the repulsive potential energy resulting from electrostatic interactions between like-charged particle surfaces, V_{steric} the repulsive potential energy resulting from steric interactions between particle surfaces coated with adsorbed polymeric species, and $V_{structural}$ the potential energy resulting from the presence of nonadsorbed species in solution that may either increase or decrease suspension stability. This equation, which predicts the stability of colloidal particles suspended in polar liquids, is a cornerstone of modern colloid science.
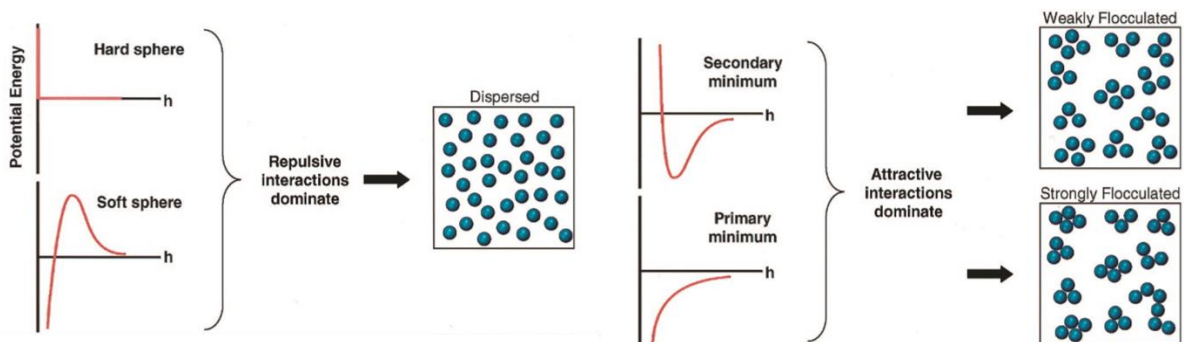
Figure 6. Schematic of the relationship between the total interparticle potential energy and the resulting suspension structure.

2.2.2. Suspension Rheology

Suspension, structure, and, hence, stability can be inferred from the observed behavior. The critical parameters of interest include the apparent viscosity (η), the yield stress under shear (τ_y) and compression (P_y), and the viscoelastic properties (i.e., the elastic (G') and loss (G") moduli) of the

system. Such parameters must be tailored for the specific forming method used during printing techniques (refer to Section 2-1).

Various types of flow behavior can be observed under steady shear depending on suspension composition and stability[4], as shown in Figure 7. Newtonian behavior is the simplest flow response, where viscosity is independent of shear rate (curve A). Pseudoplastic or shear-thinning behavior occurs when the viscosity decreases with shear rate (curve B). This response can be accompanied by a yield stress whose magnitude depends on the strength of the particle network (curve D and E). Finally, shear-thickening behavior occurs when the viscosity increases with shear rate (curve C).
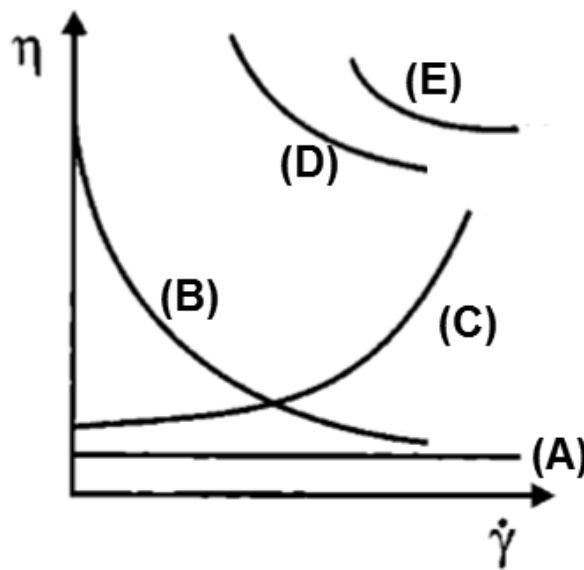
Figure 7. Types of rheological behavior of colloidal suspensions.

Concentrated colloidal suspensions commonly display viscoelastic behavior, which can be characterized by dynamic rheological measurements (or oscillatory techniques). During oscillation measurements, a frequency dependent shear stress or strain is applied to a suspension, and the shear moduli are obtained. Colloidal suspensions are usually characterized by oscillatory measurements in the linear viscoelastic regime (at small shear stresses or strains) to examine their behavior in the least perturbed state. The limit of the linear viscoelastic regime is defined as the shear stress (or strain) where the shear modulus deviates from its low shear plateau value. Structural information is obtained by conducting frequency (ω) sweeps at a given stress (or strain) in this regime[4], as shown in Figure 8. A liquid-like response is observed when G" > G'. A gel-like response is observed when G' and G" vary as ω^j, where $j = 0.3 \sim 0.7$, depending on the system. Finally, a solidlike response is observed when G' > G" over the entire frequency spectrum.
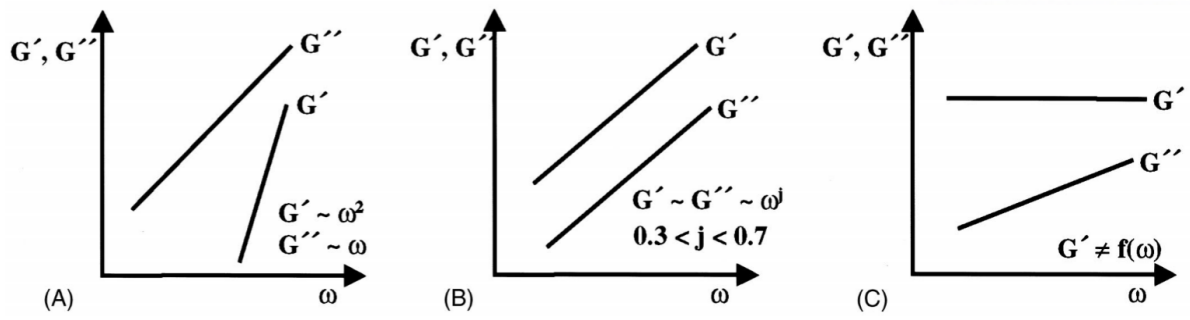
Figure 8. Schematic representation of oscillatory behavior as a function of frequency for (A) liquid, (B) gel, and (C) solid response.

2.3. Printed Battery Architectures

Design and configuration of cell components are important in developing high-performance printed batteries with aesthetic versatility. In commercial batteries, anodes and cathodes are vertically stacked (Figure 9a). This vertically stacked configuration is beneficial in reducing the distance between the anode and cathode, thereby lowering internal ohmic resistance of the cell. In addition to the vertically stacked configuration, in-plane model can be applied to batteries, wherein the anode and the cathode are positioned side-by-side (Figure 9b). The in-plane configuration is effective for widening the printing process window owing to the process simplicity and a minimal risk of short-circuit failure. The printed batteries require a broad variety of form factors and shape deformability. In this respect, the in-plane configuration could be a promising way to enrich the design and applicability of the printed batteries.
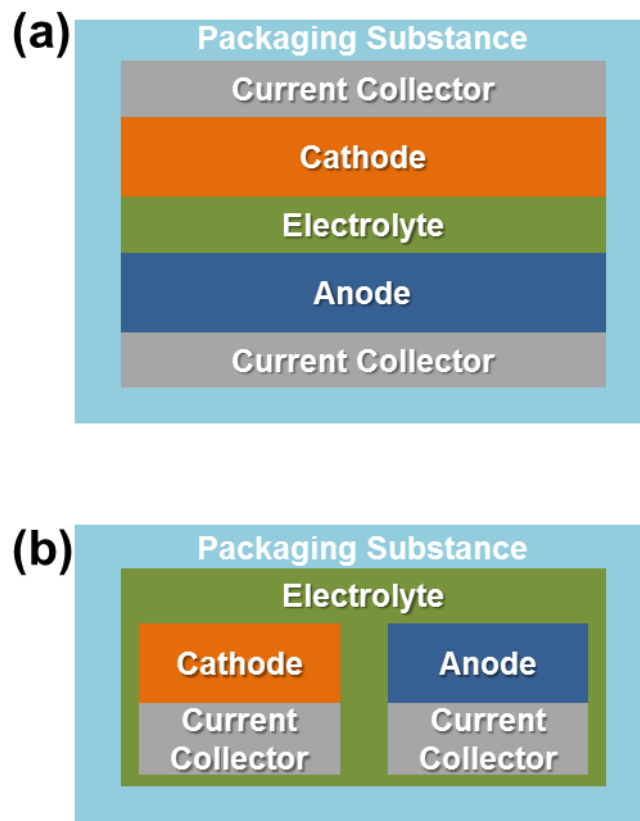
Figure 9. Schematic illustration of batteries with different component configuratoins: (a) vertically-stacked architecture; (b) in-plane architecture.

2.4. Electrochemical Systems

2.4.1. Lithium-Ion Batteries

Lithium-ion batteries (LIBs), as the main power source, dominate the portable device market due to their high energy density, high voltage window, long cyclability and eco-friendly operation.[5]

Rechargeable LIBs based on the intercalation concept were first suggested by Armand in 1972. A conventional LIB consists of a carbon anode and a lithium metal oxide cathode with a polymer separator, an organic liquid electrolyte of lithium salt with an organic solvent mixture and metal foil or mesh current collector (Figure 10). In the LIBs, the lithium ions are passes through the separator in electrolyte from the cathodes to the anodes during charging state while the electrons move from the cathodes to the anodes through the external circuit. The discharge reaction is a reverse reaction of the above reaction. The equations of chemical reactions during the charge/discharge are as follows. The $LiCoO_2$ as cathode and graphite as anode have been used in equation.

$$\text{Cathode: } LiCoO_2 \leftrightarrows Li_{1-x}CoO_2 + xLi^+ + xe^-$$

$$\text{Anode: } xLi^+ + xe^- + xC_6 \leftrightarrows xLiC_6$$

$$\text{Total reaction: } LiCoO_2 + xC_6 \leftrightarrows Li_{1-x}CoO_2 + xLiC_6$$
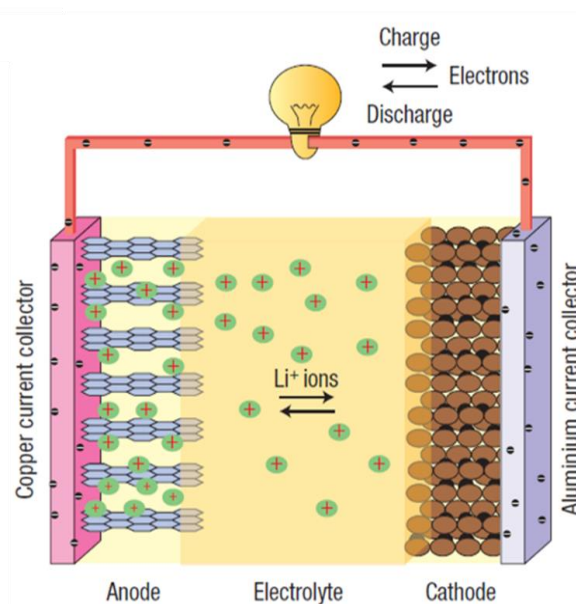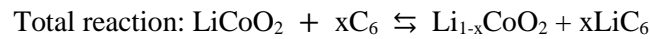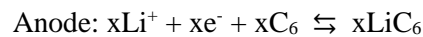
Figure 10. A scheme of conventional lithium-ion battery (anode: graphite, cathode: lithium cobalt oxide, and a liquid electrolyte containing lithium ions in a separator.)

23

2.4.2. Suspercapacitors

Supercapacitors (SCs) are a charge-storage device similar to batteries in design and manufacturing. As shown in Figure 11, SCs consist of two electrodes, an electrolyte, and a separator that electrically isolates the two electrodes[6]. The most important component in the SCs is the electrode material. In general, the SC's electrodes are fabricated from nanoscale materials that have high surface area and high porosity. It can be seen from Figure 11 that charges can be stored and separated at the interface between the conductive solid particles (such as carbon particles or metal particles) and the electrolyte. This interface can be treated as a capacitor with an electrical double-layer capacitance, which can be expressed as:

$$C = A\varepsilon/4\pi d$$

where A is the area of the electrode surface, which for a supercapacitor should be the active surface of the electrode porous layer; ε is the medium (electrolyte) dielectric constant, which will be equal to 1 for a vacuum and larger than 1 for all other materials, including gases; and d is the effective thickness of the electrical double layer.
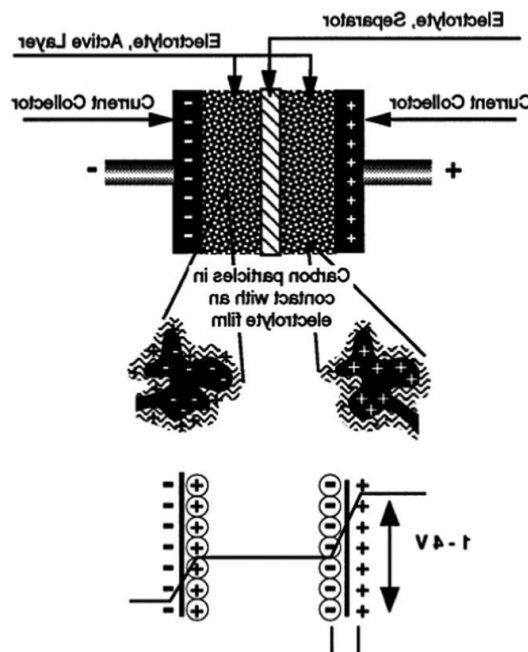
Figure 11. Schematic illustration of principles of a supercapacitor.

2.4.3. Zn-Air Batteries

During discharge, Zn-air batteries function as a power generator through the electrochemical coupling of the zinc metal to the air electrode in the presence of an alkaline electrolyte with an inexhaustible cathode reactant (oxygen) from the atmosphere[7]. The electrons liberated at the zinc travel through an external load to the air electrode, while zinc cations are produced at the zinc electrode. At the same time, atmospheric oxygen diffuses into the porous air electrode and is ready to be reduced to hydroxide ions via the oxygen reduction reaction (ORR) at a three-phase reaction site, which is the interface of oxygen (gas), electrolyte (liquid), and electrocatalysts (solid). The generated hydroxide ions then migrate from the reaction site to the zinc electrode, forming zincate ($Zn(OH)_4^{2-}$) ions, which then further decompose to insoluble zinc oxide (ZnO) at supersaturated $Zn(OH)_4^{2-}$ concentrations. During charging, the zinc–air battery is capable of storing electric energy through the oxygen-evolution reaction (OER), occurring at the electrode–electrolyte interface, whereas the zinc is deposited at the cathode surface. The overall reaction can be simply shown as Zn combining with O_2 to form ZnO. The overall reaction is:

$$\text{(Cathode reaction) } O_2 + 2H_2O + 4e^- \leftrightarrow 4OH^-, E = 0.40 \text{ V vs. SHE}$$

$$\text{(Anode reaction) } Zn + 2OH^- \leftrightarrow ZnO + H_2O + 2e^-, E = -1.26 \text{ V vs. SHE}$$

$$\text{(Overall reaction) } 2Zn + O_2 \leftrightarrow 2ZnO, E = 1.66 \text{ V vs. SHE}$$
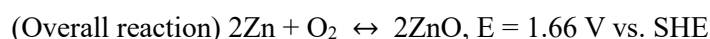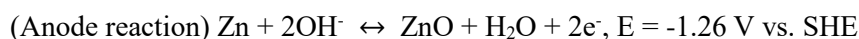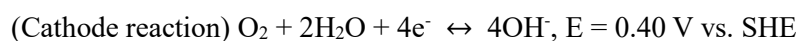
Thermodynamically, both reactions are spontaneous and produce a theoretical voltage of 1.66 V. However, the redox reactions of oxygen during the charging and discharging cycles are kinetically slow; thus, electrocatalysts are often used to accelerate the process. For the electrically rechargeable zinc–air battery, each main structural component faces its own challenges. For the air electrode, it is difficult to find a catalyst that facilitates both redox reactions, thereby limiting the power density of zinc–air batteries. Morevoer, carbon dioxide (CO_2) in the air can undergo a carbonation reaction with the alkaline electrolyte, thus changing the reaction environment inside the cell. The carbonate by-product can potentially block the pores of the GDL, which limits access to air. For the separator, it is challenging to find a material that is robust in a basic environment, yet also allows the flow of hydroxide ions exclusively while blocking the zinc ions. For the zinc metal electrode, it is difficult to control the non-uniform dissolution and deposition of zinc, which is the main cause of dendrite formation and shape change.

2.5.   References

(1)   A. M. Gaikwad, A. C. Arias, D. A. Steingart, *Energy Technol.* **2015**, *3*, 305.

(2)   M. Kuang, L. Wang, Y. Song, *Adv. Mater.* **2014**, 26, 6950.

(3)   C. C. Ho, J. W. Evans, P. K. Wright, J. Micromech. Microeng. **2010**, 20, 104009.

(4)   J. A. Lewis, *J. Am. Ceram. Soc*. **2000**, 83, 2341.

(5)   J. M. Tarascon, M. Armand, *Nature* **2001**, 414, 359.

(6)   G. Wang, L. Zhang, J. Zhang, *Chem. Soc. Rev*. **2012**, 41, 797.

(7)   J. Fu, Z. P. Cano, M. G. Park, A. Yu, M. Fowler, Z. Chen, *Adv. Mater*. **2017**, 29, 1604685.

CHAPTER III. Printed, Shape-Conformable, Solid-State Batteries with Vertically-Stacked Architecture

3.1. Printed, Solid-State Lithium-Ion Batteries: A New Route toward Shape-Conformable Power Sources

3.1.1. Introduction

Rapidly emerging flexible/wearable electronic devices with unusual shape diversity and mobile usability, including wrist-mounted cellular phones, roll-up displays, Google Glass, smart electronic clothing (so-called "e-textiles"), wearable robotic suits and implantable/patchable sensors, draw considerable attention as a kind of disruptive technology to drastically change our daily lives.[1-4] Stimulated by such promising prospect, a number of global electronics makers are fiercely competing to preoccupy this attractive market. To accelerate the advent of the smart electronics era, along with never-ceasing pursuit of high-performance flexible displays and memory chips, development of thin, lightweight and flexible rechargeable power sources should be indispensably required.[5-10]

Among various rechargeable energy storage systems, current state-of-the-art lithium-ion batteries, the most widespread portable power source, could be suggested as a promising solution to fulfill the stringent requirements for flexible electronics.[8-12] From the cell manufacturing point of view, conventional lithium-ion batteries with fixed shapes and sizes are generally fabricated by winding (or stacking) cell components (such as anodes, cathodes and microporous separator membranes) and then packaging them with (cylindrical-/rectangular-shaped) metallic canisters or pouch films, finally followed by injection of liquid electrolytes. In particular, the use of liquid electrolytes gives rise to serious concerns in cell assembly, because they require strict packaging materials to avoid leakage problems and also separator membranes to prevent electrical contact between electrodes.[8,10,13] For these reasons, the conventional cell assembly and materials have pushed the batteries to lack of variety in form factors, thus imposing formidable challenges on their integration into versatile-shaped electronic devices.

The abovementioned design limitation of traditional batteries has spurred us to pay much attention to flexible batteries with shape/design diversity. To date, many of the research works on flexible batteries have been primarily devoted to rational design/synthesis/structural engineering of electrode materials. Details on the previous studies have been comprehensively described in the review articles.[6-10] Some representative achievements include the nanostructured electrode materials based on low-dimensional carbon materials such as carbon nanotube and graphene, and also 3-dimensional (3D) non-metallic current collectors exploiting conductive/compliant papers and textiles.[14-18] Meanwhile, to replace combustible and fluidic liquid electrolytes, which are believed to be a major threat to cell safety and electrolyte leakage failures, solid-state (in particular, polymer-

mediated) electrolytes with balanced electrochemical properties and mechanical flexibility have been demonstrated.[13,19,20]

In addition to these materials-based approaches, a new concept of battery design and architecture, including cable (or fiber)-type and stretchable power systems, have also attracted great interests due to their shape novelty and superior flexibility.[12,18,21-23] Unfortunately, most of the previous works have still relied on traditional cell assembly processes (i.e., winding (or stacking) of electrode sheets and separator membranes → packaging → injection of liquid electrolyte). Meanwhile, in order to address this cell manufacturing-related issues, new fabrication processes such as multi-step spray painting and screen printing processes were recently reported.[24-27] However, they still required the injection step of liquid electrolyte and also a set of mask or screen mesh for spatial alignment of battery components.

Here, as a facile and efficient strategy to resolve the abovementioned deadlocks of conventional battery technologies and also to develop flexible power sources with exceptional shape conformability and aesthetic versatility, we demonstrate a new class of printable solid-state batteries (hereinafter, referred to as "PRISS" batteries). Printing is known to be a simple and reliable technique capable of imparting various surface functionality to a wide diversity of substrates. In particular, stencil printing is one of mass-printing methods, which can be realized by pressing rheologically-tuned inks through a preformed stencil with a squeegee.[28] Recently, besides traditional application fields of printing technology for commodity interests, printed electronics has emerged as an attractive industry due to its process benefits enabling facile fabrication of solution-processable thin-film transistors[28-30] and integrated circuits.[31] In addition, printing concept was exploited in the development of new power sources, although most of which were related to zinc primary batteries. Nylon mesh-embedded Zn electrodes,[32] KOH electrolyte-swelled polyethylene oxide/methyl cellulose gel polymer electrolytes[33] and ionic liquid-swelled polyvinylidene fluoride-hexafluoropropylene gel polymer electrolytes[34] were fabricated via various printing methods. Meanwhile, our group recently reported a bendable and imprintable solid-state composite electrolyte (SCE) as an alternative electrolyte for use in flexible batteries.[20,35]

To fabricate the PRISS batteries, their major components (i.e., SCE layer and SCE matrix-embedded electrodes) are consecutively printed on arbitrary objects of complex design/geometries through simple stencil printing process (followed by ultraviolet (UV) crosslinking). More notably, this printing process for PRISS batteries does not require traditional processing solvents such as acetone, water and N-methyl pyrrolidone (that are essentially used for preparation of conventional electrodes/self-standing polymer electrolyte films and also demand time-/energy-consuming drying processes), liquid-electrolyte injection and conventional microporous separator membranes, eventually leading to the fabrication of fully-integrated, multilayer-structured PRISS batteries with

shape conformability and design universality far beyond those accessible with conventional cell components and manufacturing processes. Furthermore, such process simplicity and scalability of PRISS batteries allow seamless integration into complex-shaped electronic devices, thus enabling the realization of power source-unitized electronics. We anticipate that PRISS batteries hold a great deal of promise as a versatile and scalable platform technology to overcome battery-triggered design issues facing flexible/wearable electronic gadgets.

3.1.2. Experimental

3.1.2.1. Architecture Design and Fabrication

To fabricate printable electrodes, the SCE matrix precursor, which was composed of UV-curable ETPTA monomer (incorporating 1.0 wt.% HMPP as a photoinitiator) and high boiling point electrolyte (1M $LiPF_6$ in EC/PC = 1/1 v/v) wherein the composition ratio of ETPTA/high boiling point electrolyte = 15/85 (w/w), was mixed with electrode active materials (here, LFP (Süd Chemie) and LTO (Süd Chemie) powders were chosen) and carbon black conductive additives. The weight-based composition ratios of electrode slurry mixtures were electrode active powders/carbon black/SCE matrix precursor = 38/4/58 (w/w/w) for LFP cathode and 27/7/66 (w/w/w) for LTO anode, respectively. The LTO anode slurry was printed on an Al current collector using stencil printing technique (copper foil-based stencils with various shapes/thickness were used) without using any processing solvents such as NMP or water and then exposed to UV irradiation for a short time less than 30 sec, yielding the printable LTO anode. The UV irradiation was performed using a Hg UV-lamp (Lichtzen), with an irradiation peak intensity of approximately 2000 mW cm^{-2} on the sample surface. Subsequently, on top of the LTO anode, the SCE paste (ETPTA/1M $LiPF_6$ in $EC/PC/Al_2O_3$ nanoparticles (average particle size ~ 300 nm) = 5/28/67 w/w/w) was introduced via the same stencil printing and UV curing process, leading to a solid-state SCE thin layer on the LTO anode. Then, the LFP cathode slurry was printed directly on the SCE layer/LTO anode unit and subjected to UV irradiation. After placing Al current collector on top of the printable LFP cathode/printable SCE layer/printable LTO anode (C/S/A) assembly, a full-integrated and multilayer-structured PRISS cell was finally obtained.

3.1.2.2. Structural/rheological/physical characterization

The UV curing reaction of the printable cell components such as cathode, anode and electrolyte was examined using a FT-IR spectrometer (FT-3000, Excalibur) with a spectral resolution of 4 cm-1. The morphologies (cross-sectional view) of the printable cell components were characterized by field emission scanning electron microscopy (FE-SEM, Hitachi) equipped with energy-dispersive spectrometer (EDS). The rheological properties of the printable cell components were measured with a rheometer (Haake MARS 3, Thermo Electron GmbH). The physical flexibility of the printable cell components upon mechanical deformation such as folding and winding (rod diameter = 5 mm) was also investigated.

3.1.2.3. Electrochemical Analysis and Shape Conformability

To elucidate basic electrochemical performance of PRISS batteries (including half cells), a

unit cell (2032-type coin) was prepared in an argon-filled glove box. The cell performance was measured using a cycle tester (PNE Solution) at various charge/discharge conditions. To explore potential applicability of PRISS batteries as a shape-conformable power source with aesthetic versatility, the PRISS cells were fabricated directly on paper (Hi-Q ACB, HANSOL PAPER Co., Korea)-made eyeglasses and a transparent glass cup using the abovementioned stencil printing and UV-curing process. Here, to visualize the unique architecture of PRISS cells, a transparent PDMS-coated PE film (thickness ~ 100 μm) was prepared and employed as a flexible packaging material. Also, the "PRISS" letters-shaped PRISS cell was fabricated through the stencil printing-based manufacturing process. To understand electronic/ionic transport phenomena of PRISS cells, with a particular focus on electrochemical behavior inside electrodes, the EIS (VSP classic, Bio-Logic) analysis was performed using symmetric cells with two different modes (non-blocking vs. blocking) over a frequency range of 10^{-1} to 10^6 Hz.

3.1.3. Results and discussion

3.1.3.1. Architecture Design
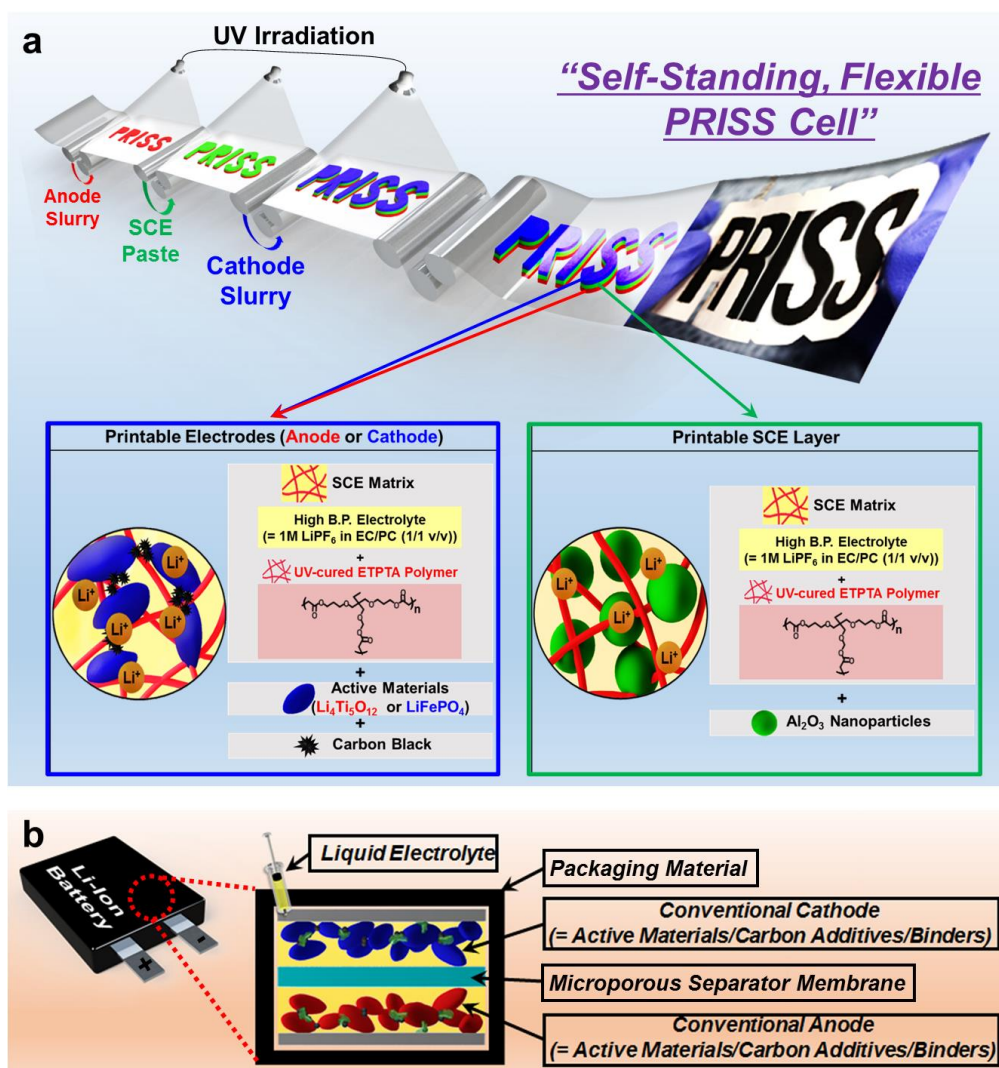
Figure 12. (a) A schematic representation depicting the stepwise fabrication procedure for PRISS cells, wherein chemical structure of their major components and a photograph of the self-standing, flexible "PRISS" letters-shaped PRISS cell were provided. The stencil-printable electrodes were composed of electrode active materials (here, LFP (for cathode) and LTO (for anode) powders were chosen as model electrode active materials), carbon black conductive additives and SCE matrix (= ETPTA polymer/high boiling point electrolyte). Between the stencil-printable electrodes, a stencil-printable SCE thin layer (= ETPTA polymer/high boiling point electrolyte/Al_2O_3 nanoparticles), acting as a separator membrane as well as solid-state electrolyte, was positioned. (b) A schematic illustration of a conventional battery consisting of anode, cathode, microporous separator membrane and liquid electrolyte inside packaging material with pre-determined shape and size.

The stepwise fabrication procedure (potentially being combined with roll-to-roll process in future works) for PRISS cells, along with chemical structure of their major components, was depicted in a schematic representation (Figure 12a). The SCE matrix precursor, which was composed of UV-curable ethoxylated trimethylolpropane triacrylate (ETPTA) monomer[20,35] (incorporating 1.0 wt.% 2-

hydroxy-2-methyl-1-phenyl-1-propanone (HMPP) as a photoinitiator) and high boiling point electrolyte (1M $LiPF_6$ in ethylene carbonate (EC, b.p. = 261 °C)/propylene carbonate (PC, b.p. = 242 °C) = 1/1 v/v) wherein the composition ratio of ETPTA/high boiling point electrolyte = 15/85 (w/w), was mixed with electrode active materials (here, $LiFePO_4$ (LFP, cathode) and $Li_4Ti_5O_{12}$ (LTO, anode) powders were chosen as model electrode active materials to explore the proof of concept for PRISS cells) and carbon black conductive additives. The EC/PC-based electrolyte shows good thermal stability due to its high boiling point/low vapor pressure.[20,35] The weight-based composition ratios of electrode slurry mixtures (= electrode active powders/carbon black/SCE matrix precursor) were respectively 38/4/58 (w/w/w) for LFP cathode and 27/7/66 (w/w/w) for LTO anode.

The LTO anode slurry was printed on an aluminum (Al) current collector using stencil printing technique (here, copper foil-based stencils with various shapes/thickness were used) and then exposed to UV irradiation for a short time less than 30 sec, leading to the SCE matrix-embedded solid state LTO anode. Subsequently, on top of the LTO anode, the SCE paste (ETPTA/high boiling point electrolyte/Al_2O_3 nanoparticles (average particle size ~ 300 nm) = 5/28/67 w/w/w) was introduced via the same stencil printing and UV curing process, yielding a printable SCE thin layer (acting as a separator membrane as well as solid state electrolyte) on the LTO anode. Then, the LFP cathode slurry was stencil printed directly on the SCE layer/LTO anode unit and subjected to UV irradiation. After placing Al current collector on top of the printable LFP cathode/printable SCE layer/printable LTO anode (C/S/A) assembly, a full-integrated and multilayer-structured PRISS cell was finally obtained. More details on the stencil printing-based cell fabrication procedure were described in the experimental section. A photograph of the self-standing, flexible "PRISS" letters-shaped PRISS cell is also presented in Figure 12a.

The PRISS cell, as compared to a conventional cell (Figure 12b) that consists of anode, cathode, microporous separator membrane and liquid electrolyte inside a packaging material with pre-determined shape and size, offers the following composition/processing benefits: i) being free from conventional microporous separator membranes and polymeric binders such as polyvinylidene fluoride (PVdF) or carboxymethylcellulose (CMC)/styrene-butadiene rubber (SBR) in the electrodes, thereby enabling the removal of time-/cost-consuming drying of processing solvents (i.e., N-methyl-2-pyrrolidone (NMP), water and so on); ii) no extra step for liquid-electrolyte injection.

3.1.3.2. Designing UV-Curable, Viscoelastic Electrodes/Electrolyte Suspensions

A key technology to enable the realization of PRISS cells is the fine-tuning of rheological properties of electrode slurries and SCE pastes, in addition to the material uniqueness of basic elements. The printable LFP cathode slurry (LFP/carbon black/SCE matrix precursor = 38/4/58

(w/w/w) without NMP solvent) presents significantly higher viscosity (~ 2.3 x 10^5 Poise) and also non-Newtonian fluid (specifically, shear-thinning) behavior (Figure 13a,b). The viscoelastic analysis of the printable LFP cathode slurry shows that G' is higher than G" at low shear stress region and the opposite trend is observed at high shear stress region. Similar rheological behavior was also observed at the LTO anode slurry (LTO/carbon black additive/SCE matrix precursor = 27/7/66 (w/w/w) without NMP solvent) (Figure 13c,d). The abovementioned rheology results of the electrode slurries verify a typical thixotropic fluid behavior.[36,37]
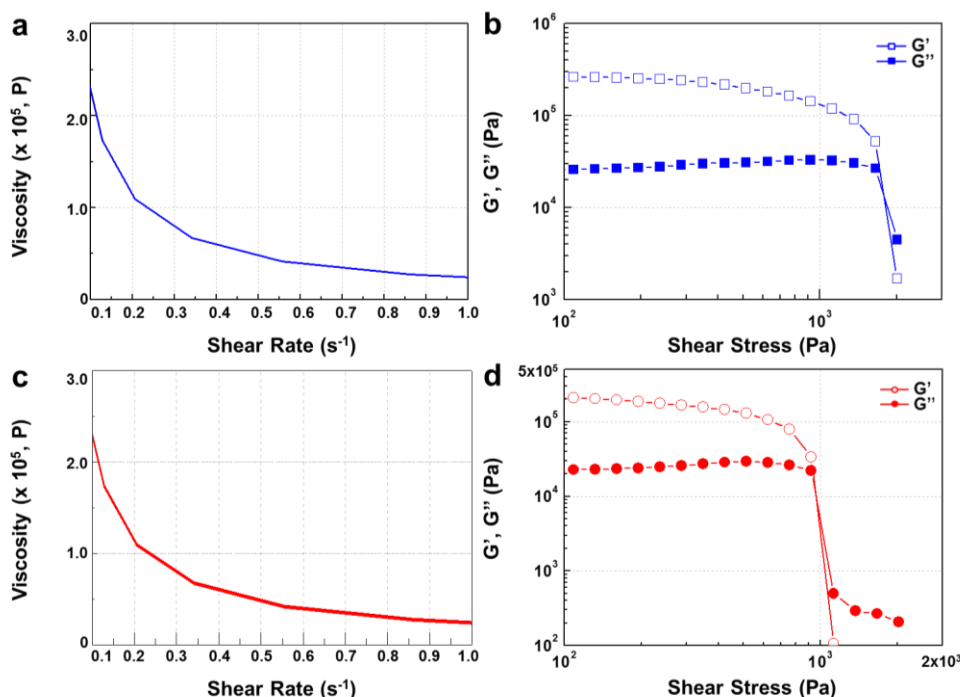
Figure 13. Rheological properties of LFP cathode suspension (LFP/carbon black additive/SCE matrix precursor = 38/4/58 (w/w/w): (a) viscosity; (b) storage modulus (G') and loss modulus (G"). Rheological properties of LTO anode suspension (LTO/carbon black additive/SCE matrix precursor = 27/7/66 (w/w/w): (c) viscosity; (d) G' and G".

Effect of the solid (= LFP powders + carbon black additives) content in the printable LFP cathode slurries on their rheological properties was investigated. In comparison to the optimized solid content ((LFP + carbon black) = 42 wt.%), the lower solid content (= 20 wt.%, the LFP/carbon black composition ratio was identical to that of the optimized solid content) in the electrode slurry reduced the viscosity and also weakened the thixotropic fluid characteristic (Figure 14a,b). Meanwhile, the higher solid content (= 50 wt.%) failed to secure good dispersion state in the cathode slurry, giving rise to serious agglomeration of particles (Figure 14c). These results underscore the importance of rheology control in fabricating the printable electrodes.
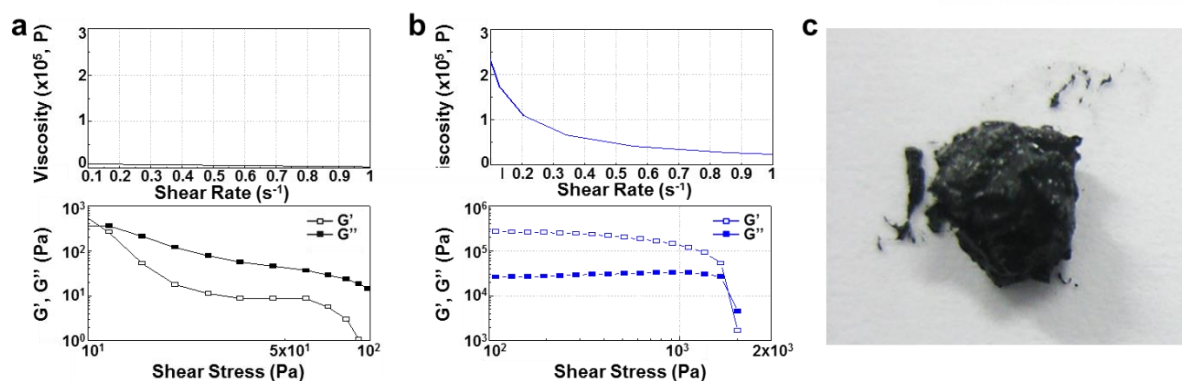
Figure 14. Rheological properties (viscosity and viscoelasticity): (a) solid content (= 20 wt%); (b) solid content (= 42 wt%). (c) At higher solid content (= 50 wt%), a photograph showing the glass transition in the cathode suspension.

With the optimized composition ratios of electrodes (LFP/carbon black/SCE matrix precursor = 38/4/58, LTO/carbon black/SCE matrix precursor = 27/7/66 w/w/w), the printable electrodes containing the solid state electrolytes were directly fabricated via the stencil printing followed by UV curing process. The cross-sectional scanning electron microscopy (SEM) and energy dispersive spectroscopy (EDS) images (Figure 15) show that the electrode active materials and carbon black additives are densely packed and also well dispersed in the through-thickness direction. Notably, the highly-percolated nanoscale interstitial voids formed between the electrode active materials and carbon black additives, corresponding to the space originally occupied by the EC/PC-based liquid electrolyte that was selectively removed using dimethyl carbonate (DMC, as an etching solvent) prior to the SEM analysis, indicate the construction of ion-conductive pathways[20,35] in the printable electrodes. In addition, the good dispersion state of LFP particles and carbon black additives was observed, revealing the formation of electronic networks in the printable electrodes. These electronic networks, in combination with the ionic channels mentioned above, are expected to play important roles in enabling normal Faradaic reactions in the printable electrodes.
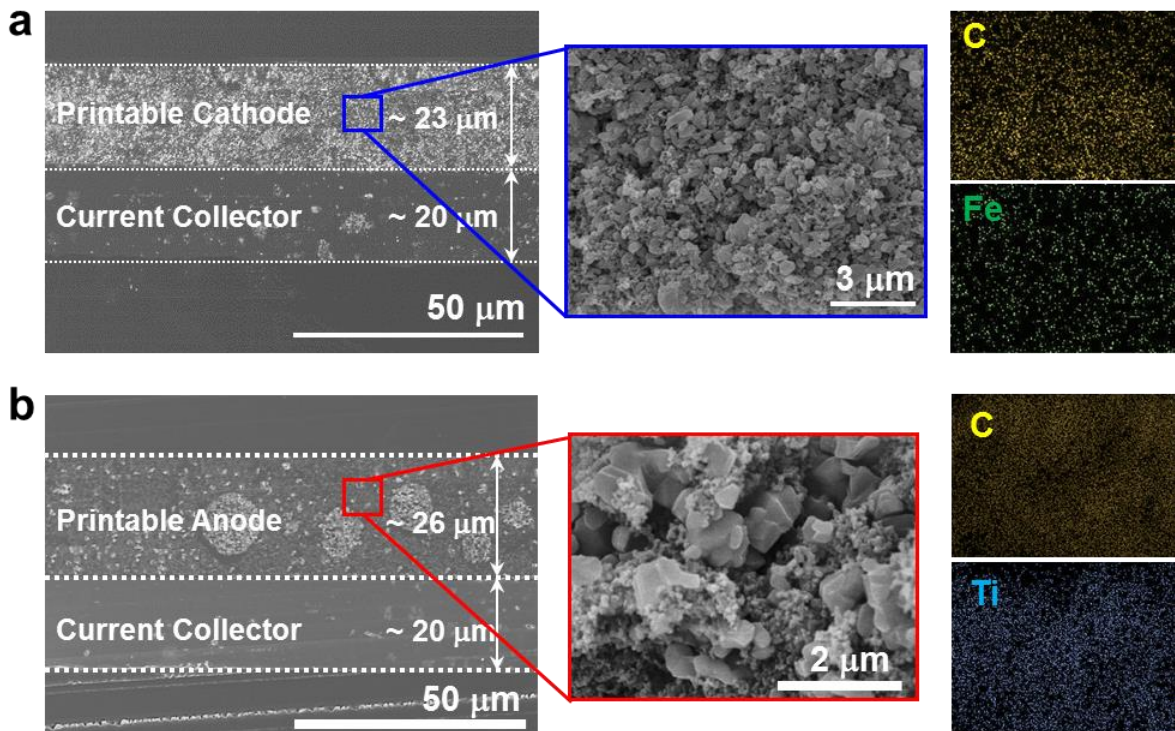
Figure 15. Morphological characterization (cross-sectional view) of (a) printable LFP cathode and (b) printable LTO anode: SEM images; EDS images.

The FT-IR analysis (Figure 16) shows that the characteristic peaks corresponding to acrylic C=C bonds (1610 - 1625 cm^{-1})[13,19,35] of ETPTA monomer disappeared after exposure to UV irradiation, demonstrating that the ETPTA monomer was photo-polymerized in the printable electrode slurry. In addition, gel content (i.e., insoluble polymer fraction after solvent (DMC → acetone) extraction) of the printable electrodes was observed to be higher than 99 %, confirming the successful UV curing reaction of ETPTA monomer.
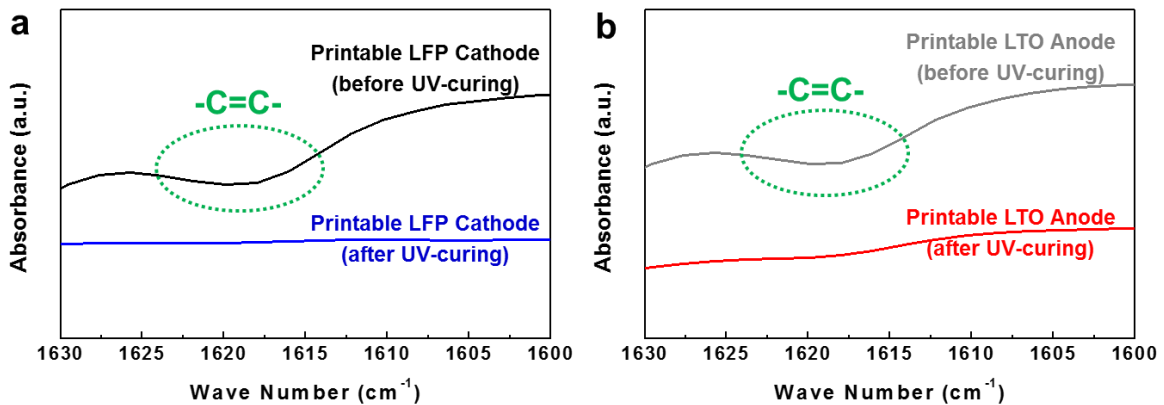
Figure 16. Change in the FT-IR spectra of acrylic C=C double bonds of ETPTA before/after UV irradiation: (a) printable LFP cathode; (b) printable LTO anode.

Figure 17a shows that the printable electrodes are not mechanically disrupted upon physical deformation such as folding and winding (rod diameter = 5 mm). The aforementioned thixotropic fluid behavior of printable electrode slurries allows the fabrication of SCE matrix-embedded electrodes having various form factors. Figure 17b shows that the LFP cathode slurry with the optimized composition (represented by a word of "UNIST") can be directly printed on an Al current collector, prior to UV curing. By comparison, the LFP cathode slurry with lower solid content (= 20%) failed to maintain the letter form when it was tilted toward vertical position.
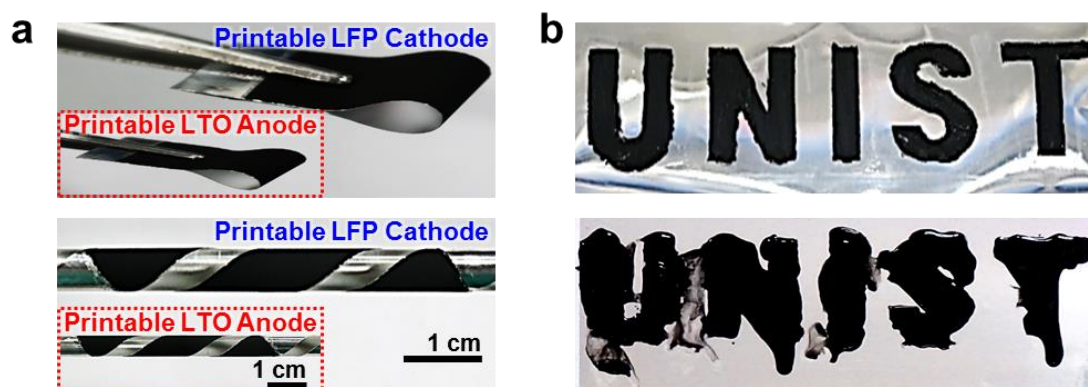
Figure 17. (a) Photographs showing mechanical flexibility of printable electrodes upon physical deformation such as folding and winding (rod diameter = 5 mm). (b) Photographs of the LFP cathode slurry with solid content = 42% (upper image) and LFP cathode slurry with solid content = 20% (lower image). The LFP cathode slurry with lower solid content failed to maintain the letter form when it was tilted toward vertical position.

In the PRISS cells, another important component is the printable SCE layer (= UV-cured ETPTA polymer/1M $LiPF_6$ in $EC/PC/Al_2O_3$ nanoparticles).[20,35] Here, the Al_2O_3 nanoparticles act as a multifunctional filler to control thixotropic fluid behavior of SCE pastes and also impart the resulting SCE layers with dimensional stability/mechanical robustness. Major characteristics of the printable SCE layers, including rheological properties (in terms of viscosity and viscoelasticity), mechanical flexibility and ionic conductivity were investigated and summarized in Figure 18.
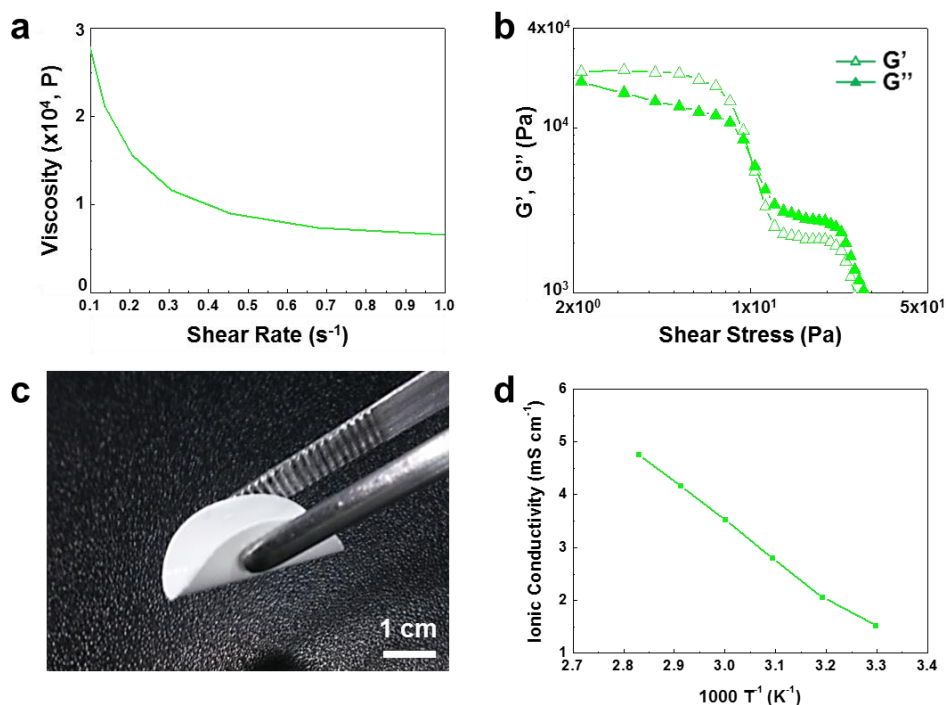
Figure 18. Major characteristics of printable SCE layers: (a) viscosity; (b) G' and G''; (c) mechanical flexibility; (d) temperature-dependent ionic conductivity.

3.1.3.3. Fabrication of Printed Batteries

Based on the understanding of structure and physicochemical properties of printable electrodes and printable SCE layers, electrochemical performance of PRISS cells was investigated in terms of their charge/discharge behavior. Figure 19a shows charge/discharge profiles of a LFP half cell (= printable LFP cathode/(1M LiPF$_6$ in EC/PC)-soaked polyethylene (PE) separator/lithium metal anode) as a function of cycle number. The cell was cycled at a fixed charge/discharge current density of 0.1 C (= 0.05 mA cm^{-2})/0.1 C under a voltage range of 2.5 - 3.8 V. No abnormal charge/discharge behavior was observed with cycling, demonstrating the electrochemical validity of the printable LFP cathode. The half-cell performance of a printable LTO anode was also examined (Figure 19b). Similar to the results of the printable LFP cathode, the printable LTO anode showed stable charge/discharge cycling behavior.
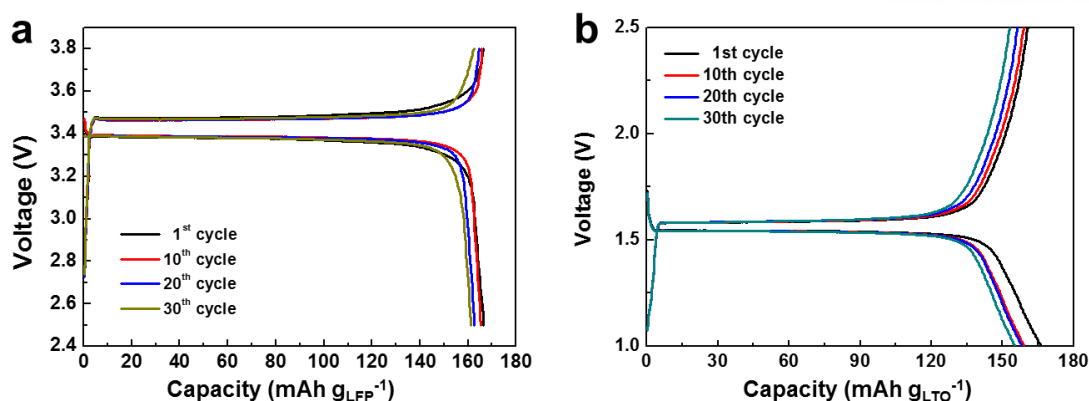
Figure 19. Galvanostatic charge/discharge profiles as a fuction of cycle number, where the gravimetric charge/discharge capacity was estimated based on the mass of active materials: (a) a LFP half cell (= printable LFP cathode/(1M LiPF$_6$ in EC/PC)-soaked PE separator/lithium metal anode); (b) a LTO half cell (= printable LTO anode/(1M LiPF$_6$ in EC/PC)-soaked PE separator/lithium metal anode).

After elucidating the half-cell performance of each printable electrode, a PRISS full cell (composed of the printable LTO anode, printable SCE layer and printable LFP cathode) was fabricated and its electrochemical performance was analyzed. A cross-sectional SEM image (Figure 20a) shows that a PRISS full cell (= printable LFP cathode (~ 34 μm, excluding Al current collector)/printable SCE layer (~ 60 μm)/printable LTO anode (~ 25 μm)) was successfully constructed, wherein the EC/PC-based liquid electrolyte was removed prior to the SEM analysis. Neither structural instability nor delamination between the electrodes and SCE layer was observed in the PRISS cell.
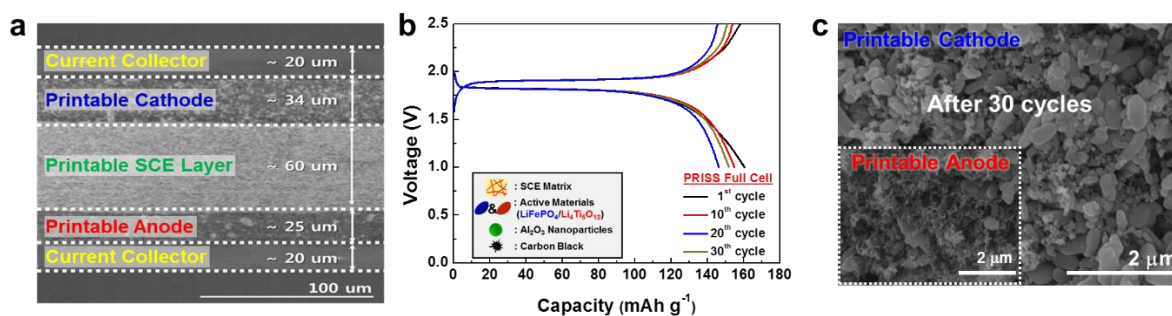
Figure 20. (a) A SEM image (cross-sectional view) of a PRISS full cell (= printable LFP cathode (LFP/carbon black/SCE matrix = 38/4/58 w/w/w)/printable SCE layer (ETPTA/1M LiPF$_6$ in EC/PC/Al$_2$O$_3$ nanoparticles = 5/28/67 w/w/w)/printable LTO anode (LTO/carbon black/SCE matrix = 27/7/66 w/w/w)), wherein the EC/PC-based liquid electrolyte was removed prior to the SEM analysis. (b) Galvanostatic charge/discharge profiles of a PRISS full cell as a function of cycle number. The cell was cycled between 1.0 and 2.5 V at a constant charge/discharge current density (= 0.05 C/0.05 C), where gravimetric charge/discharge capacity was estimated based on the mass of LFP active materials. (c) SEM images (cross-sectional view) of the printable electrodes after the cycling test (30 cycles).

39

The electrochemical performance of the PRISS full cell was examined at room temperature (Figure 20b), where the cell was cycled between 1.0 and 2.5 V at a constant charge/discharge current density (= 0.05 C/0.05 C). The PRISS full cell presents normal charge/discharge profiles and also stable capacity retention (~ 90 %) up to 30 cycles, even without injection of extra liquid electrolyte and conventional microporous separator membranes. The abovementioned electrochemical behavior of the PRISS full cell can be explained by the favorable ion/electron pathways constructed in the printable electrodes (Figure 15) and also the facile ion conduction through the printable SCE layer (Figure 18). The structural stability of the PRISS full cell after the cycling test (30 cycles) was investigated. The full-integrated multilayer structure was well preserved and neither morphological disruption nor local structural defects were found at the printable electrodes (Figure 20c).

3.1.3.4. Shape Conformability/Flexibility

Currently available batteries with traditional designs and shapes (in most cases, cylindrical, prismatic and pouch types) have critical limitations in developing power source-unitized electronics. To facilitate the advent of flexible/wearable electronics era, the power systems need to be shape-conformable and also seamlessly integrated with electronic devices. In this respect, PRISS cells could be suggested as a promising candidate to power next-generation flexible/wearable electronic devices.

To explore the applicability of PRISS cells, we prepared paper-made eyeglasses as a kind of Google Glass-mimic ones and then fabricated the PRISS cell directly on top of the paper-made eyeglasses. The components and composition ratio of the PRISS cell were the same as those provided in Figure 20. Onto one side (Al foil was pre-attached as a current collector) of the paper-made eyeglasses, the LTO anode slurry (comprising LTO/carbon black/SCE matrix precursor) was printed and exposed to UV irradiation. Subsequently, the SCE layer was introduced onto the printable LTO anode. Finally, the LFP cathode was printed on top of the printable SCE layer/printable LTO anode assembly. During the whole printing-based fabrication steps (Figure 21), any dripping-induced shape failure or dimensional disruption was not observed, demonstrating process superiority of the PRISS cell as a new class of wearable power source. Here, to visualize the unusual architecture of the PRISS cell, a transparent PDMS-coated PE film (thickness ~ 100 μm) was used as a flexible

packaging material. Figure 21 shows that the PRISS cell was directly fabricated on the paper-made eyeglasses and also operated a light emitting diode (LED) lamp connected to the power source-unitized, paper-made eyeglasses.
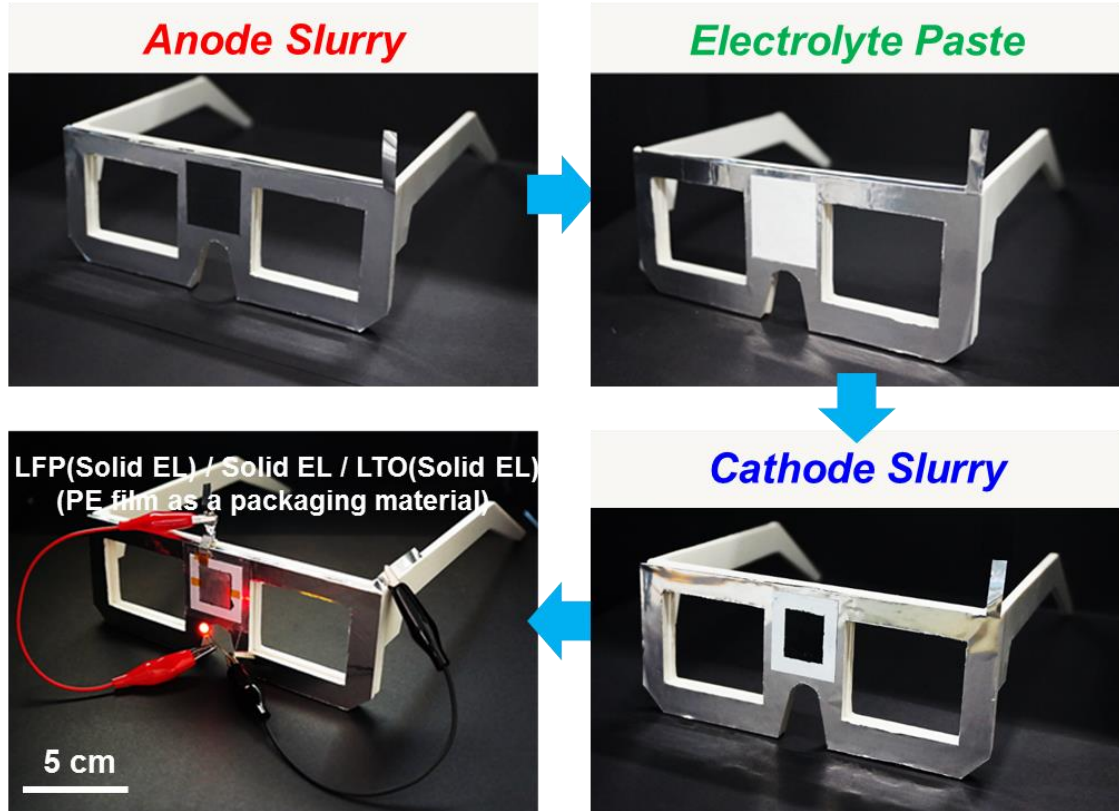
Figure 21. A photograph showing direct fabrication of a PRISS cell on paper-made eyeglasses. The PRISS cell-unitized wearable eyeglasses operated a LED lamp.

To further highlight the versatile applicability and also shape-conformable feature of PRISS cells, a transparent glass cup was chosen as another example representing complex-shaped objects. Even on a curvilinear surface of the glass cup, a heart-shaped PRISS cell was fabricated using the aforementioned simple stencil printing and UV curing process. Figure 22 exhibits that the PRISS cell, under being mounted on the round-shaped glass cup, delivers normal charge/discharge behavior.
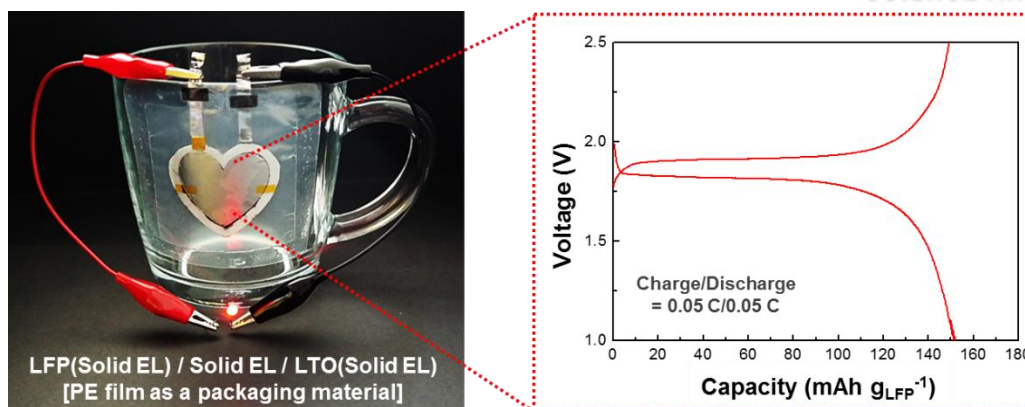
Figure 22. A photograph showing direct fabrication of a heart-shaped PRISS cell on a transparent glass cup with curvilinear surface. The PRISS cell, under being mounted on the round-shaped glass cup, delivered normal charge/discharge behavior (at charge/discharge current density of 0.05 C/0.05 C under voltage range of 1.0 - 2.5 V, gravimetric charge/discharge capacity was estimated based on the mass of LFP active materials).

Notably, this unique printability of PRISS cells allows us to make letters-shaped power sources. Figure 23 shows that the "PRISS" letters-shaped PRISS cell were successfully developed through the stencil printing and UV curing process. The letters-shaped PRISS cell presented normal charge/discharge profiles. Furthermore, to elucidate mechanical flexibility of the letters-shaped PRISS cell, the cells were completely wound along the rods having different diameters (= 5, 10, 15 mm), which ensured that the entire part of the cells was subjected to the same bending deformation. The charge/discharge behavior of the cells was examined under the fully wound state, not a planar configuration. The letters-shaped PRISS cell maintained its dimensional stability even after being mechanically bended and also showed no appreciable deterioration in the charge/discharge profiles.

The abovementioned proof-of-concept results underscore the exceptional shape conformability/design universality/printability of PRISS batteries far beyond those accessible with conventional battery technologies. Future works will be devoted to improving electrochemical performance (including energy density, rate capability and long-term cycling performance) of PRISS cells, with a focus on optimization of their composition/architecture and incorporation of new electrochemically-active materials[43-46] such as high-voltage/high-capacity electrode materials and high-conductive functional electrolytes, and also nanoengineered electrically-conductive additives.
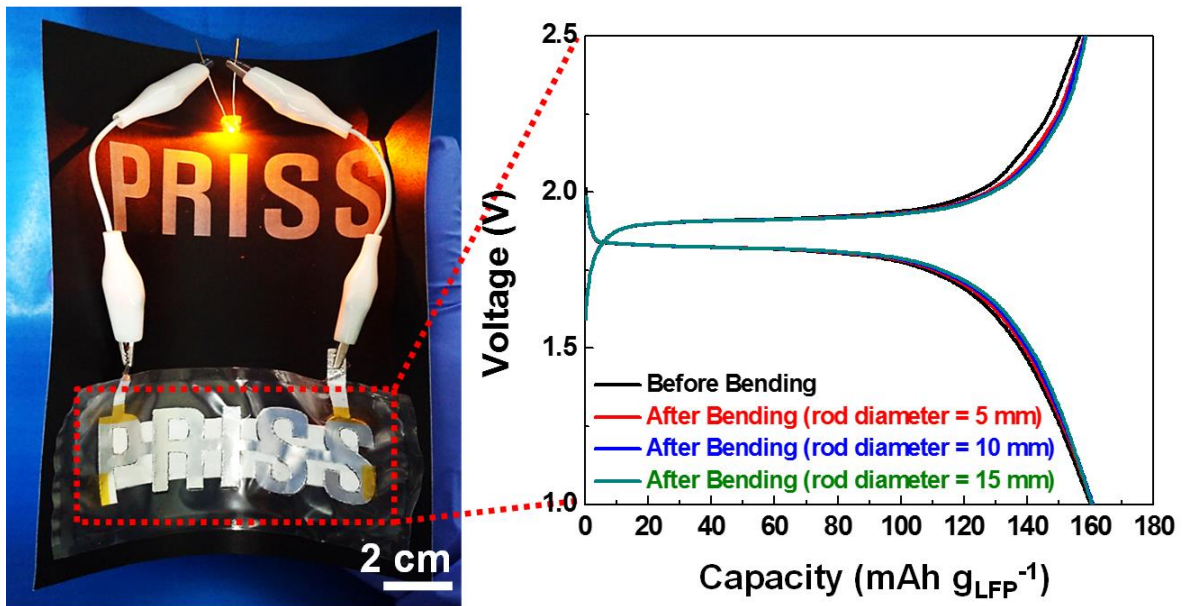
Figure 23. A photograph of "PRISS" letters-shaped PRISS cell (left side) and its charge/discharge profiles at charge/discharge current density of 0.05 C/0.05 C under voltage range of 1.0 - 2.5 V (right side, gravimetric charge/discharge capacity was estimated based on the mass of LFP active materials), which were measured under being completely wound along the rods having different diameters (= 5, 10, 15 mm), not a planar configuration.

3.1.4. Conclusion

In summary, we have presented the PRISS batteries as a versatile and scalable platform technology to open a new concept of cell architecture and fabrication route toward shape-conformable power sources with aesthetic versatility, which could overcome power source-related design/performance limitations in flexible/wearable electronic devices. The PRISS batteries were successfully fabricated through the simple stencil printing process followed by UV curing. The rheology control (toward thixotropic fluid behavior) of electrode slurries and SCE pastes, in combination with the well-tailored core elements including the UV-cured ETPTA polymer and high boiling point electrolyte, played key roles in realizing the exceptional printability. Such process and material uniqueness simplified the cell assembly process (specifically, being free from solvent drying/liquid-electrolyte injection/microporous separator membranes), thereupon enabling the fully-integrated multilayer-structured PRISS cells with various form factors far beyond those achievable by conventional battery technologies. More notably, the shape-conformable PRISS cells were seamlessly integrated with versatile-shaped objects such as paper-made eyeglasses and glass cups. In addition, the letters-shaped power sources were fabricated using the PRISS battery technology. We anticipate that the PRISS cells could be combined with fine-precision inkjet or three-dimensional printing techniques, which will offer unprecedented opportunities for development of multidimensional/multiscale complex-structured power sources. Future studies will be also focused on improving electrochemical performance of PRISS cells by introducing advanced electrochemically-active materials and optimizing their composition/architecture, along with continuing efforts toward making other cell components (for example, current collectors and packaging materials) printable, which will eventually enable direct fabrication of all-printable batteries with affordable and reliable electrochemical properties that are universally applicable to any arbitrary objects.

3.1.5. References

(1) Lu, X.; Xia, Y. *Nat. Nanotechnol.* **2006**, *1*, 163-164.

(2) Gate, B. D. *Science* **2009**, *323*, 1566-1567.

(3) Rogers, J. A.; Someya, T.; Huang, Y. *Science* **2010**, *327*, 1603-1607.

(4) Cima, M. J. *Nat. Biotechnol.* **2014**, *32*, 642-643.

(5) Bae, J.; Song, M. K.; Park, Y. J.; Kim, J. M.; Liu, M.; Wang, Z. L. *Angew. Chem. Int. Ed.* **2011**, *50*, 1683-1687.

(6) Lee, S.-Y.; Choi, K.-H.; Choi, W.-S.; Kwon, Y.-H.; Jung, H.-R.; Shin, H.-C.; Kim, J.-Y. *Energy Environ. Sci.* **2013**, *6*, 2414-2423.

(7) Gwon, H.; Hong, J.; Kim, H.; Seo, D.-H.; Jeon, S.; Kang, K. *Energy Environ. Sci.* **2014**, *7*, 538-551.

(8) Zhou, G.; Li, F.; Cheng, H.-M. *Energy Environ. Sci.* **2014**, *7*, 1307-1338.

(9) Li, L.; Wu, Z.; Yuan, S.; Zhang, X.-B. *Energy Environ. Sci.* **2014**, *7*, 2101-2122.

(10) Wang, X.; Lu, X.; Liu, B.; Chen, D.; Tong, Y.; Sehn, G. *Adv. Mater.* **2014**, *26*, 4763-4782.

(11) Lee, Y.-H.; Kim, J.-S.; Noh, J.; Lee, I.; Kim, H. J.; Choi, S.; Seo, J.; Jeon, S.; Kim, T.-S.; Lee, J.-Y.; Choi, J. W. *Nano Lett.* **2013**, *13*, 5753-5761.

(12) Ren, J.; Zhang, Y.; Bai, W.; Chen, X.; Zhang, Z.; Fang, X.; Weng, W.; Wang, Y.; Peng, H. *Angew. Chem. Int. Ed.* **2014**, *53*, 7864-7869.

(13) Choi, K.-H; Cho, S.-J.; Kim, S.-H.; Kwon, Y. H.; Kim, J. Y.; Lee, S.-Y. *Adv. Funct. Mater.* **2014**, *24*, 44-52.

(14) Hu, L.; Pasta, M.; Mantia, F. L.; Cui, L.; Jeong, S.; Deshazer, H. D.; Choi, J. W.; Han, S. M.; Cui, Y. *Nano Lett.* **2010**, *10*, 708-714.

(15) Hu, L.; Wu, H.; La Mantia, F.; Yang, Y.; Cui, Y. *ACS Nano* **2010**, *4*, 5843-5848.

(16) Kaempgen, M.; Chan, C. K.; Ma, J.; Cui, Y.; Gruner, G. *Nano Lett.* **2009**, *9*, 1872-1876.

(17) Jost, K.; Perez, C. R.; McDonough, J. K.; Presser, V.; Heon, M.; Dion, G.; Gogotsi, Y. *Energy Environ. Sci.* **2011**, *4*, 5060-5067.

(18) Weng, W.; Sun, Q.; Zhang, Y.; Lin, H.; Ren, J.; Lu, X.; Wang, M.; Peng, H. *Nano Lett.* **2014**, *14*, 3432-3438.

(19) Ha, H.-J.; Kil, E.-H.; Kwon, Y. H.; Kim, J. Y.; Lee, C. K.; Lee, S.-Y. *Energy Environ. Sci.* **2012**, *5*, 6491-6499.

(20) Kim, S.-H.; Choi, K.-H.; Cho, S.-J.; Kil, E.-H.; Lee, S.-Y. *J. Mater. Chem. A* **2013**, *1*, 4949-4955.

(21) Kwon, Y. H.; Woo, S.-W.; Jung, H.-R.; Yu, H.-K.; Kim, K.; Oh, B. H.; Ahn, S.; Lee, S.-Y.; Song, S.-W.; Cho, J.; Shin, H.-C.; Kim, J. Y. *Adv. Mater.* **2012**, *24*, 5192-5197.

(22) Kou, L.; Huang, T.; Zheng, B.; Han, Y.; Zhao, X.; Gopalsamy, K.; Sun. H.; Gao, C. *Nat. Commun.* **2014**, *5*, 3754-3763.

(23) Xu, S.; Zhang, Y.; Cho, J.; Lee, J.; Huang, X.; Jia, L.; Fan, J. A.; Su, Y.; Su, J.; Zhang, H.; Cheng, H.; Lu, B.; Yu, C.; Chuang, C.; Kim, T.-I.; Song, T.; Shigeta, K.; Kang, S.; Dagdeviren, C.; Petrov, I.; Braun, P. V.; Huang, Y.; Paik, U.; Rogers, J. A. *Nat. Commun.* **2013**, *4*, 1543-1550.

(24) Singh, N.; Galande, C.; Miranda, A.; Mathkar, A.; Gao, W.; Reddy, A. L. M.; Vlad, A.; Ajayan, P. M. *Sci. Rep.* **2012**, *2*, 481-485.

(25) Xu, Y.; Schwab, M. G.; Strudwick, A. J.; Hennig, I.; Feng, X.; Wu, Z.; Mullan, K. *Adv. Energy Mater.* **2013**, *3*, 1035-1040.

(26) Wang, X.; Liu, B.; Xiang, Q.; Wang, Q.; Hou, X.; Chen, D.; Shen, G. *ChemSusChem* **2014**, *7*, 308-313.

(27) Sun, K.; Wei, T.-S.; Ahn, B. Y.; Seo, J. Y.; Dillon, S. J.; Lewis, J. A. *Adv. Mater.* **2013**, *25*, 4539-4543.

(28) Hyun, W. J.; Secor, E. B.; Hersam, M. C.; Frisbie, C. D.; Francis, L. F. *Adv. Mater.* **2015**, *27*, 109-115.

(29) Hong, K.; Kim, S. H.; Lee, K. H.; Frisbie, C. D. *Adv. Mater.* **2013**, *25*, 3413-3418.

(30) Fukuda, K.; Takeda, Y.; Yoshimura, Y.; Shiwaku, R.; Tran, L. T.; Sekine, T.; Mizukami, M.; Kumaki, D.; Tokito, S. *Nat. Commun.* **2014**, *5*, 4147-4154..

(31) Baeg, K.-J.; Caironi, M.; Noh, Y.-Y. *Adv. Mater.* **2013**, *25*, 4210-4244.

(32) Gaikwad, A. M.; Whiting, G. L.; Steingart, D. A.; Arias, A. C. *Adv. Mater.* **2011**, *23*, 3251-3255.

(33) Braam, K. T.; Volkman, S. K.; Subramanian, V. *J. Power Sources* **2012**, *199*, 367-372.

(34) Ho, C. C.; Evans, J. W.; Wright, P. K. *J. Micromech. Microeng.* **2010**, *20*, 104009-104017.

(35) Kil, E.-H.; Choi, K.-H.; Ha, H.-J.; Xu, S.; Rogers, J. A.; Kim, M. R.; Lee, Y.-G.; Kim, K. M.; Cho, K. Y.; Lee, S.-Y. *Adv. Mater.* **2013**, *25*, 1395-1400.

(36) Pignon, F.; Magnin, A.; Piau, J.-M. *J. Rheol.* **1998**, *42*, 1349-1373.

(37) Wallevik, J. E. *Cem. Concr. Res.* **2009**, *39*, 14-29.

(38) Ogihara, N.; Kawauchi, S.; Okuda, C.; Itou, Y.; Takeuchi, Y.; Ukyo, Y. *J. Electrochem. Soc.* **2012**, *159*, A1034-A1039.

(39) Illig, J.; Ender, M.; Chrobak, T.; Schmidt, J. P.; Klotz, D.; Ivers-Tiffee, E. *J. Electrochem. Soc.* **2012**, *159*, A952-A960.

(40) Gaberscek, M.; Moskon, J.; Erjavec, B.; Dominko, R.; Jamnik, *J. Electrochem. Solid-State Lett.* **2008**, *11*, A170.

(41) Kim, G. Y.; Petibon, R.; Dahn, J. R. *J. Electrochem. Soc.* **2014**, *161*, A506-A512.

(42) Siroma, Z.; Hagiwara, J.; Yasuda, K.; Inaba, M.; Tasaka, A. *J. Electroanal. Chem.* **2010**, *648*, 92-97.

(43) Xu, K. *Chem. Rev.* **2004**, *104*, 4303-4417.

(44) Armand, M.; Tarascon, J. M. *Nature* **2008**, *451*, 652-657.

(45) Hassoun, J.; Lee, K. S.; Sun, Y. K.; Scrosati, B. *J. Am. Chem. Soc.* **2011**, *133*, 3139-3143.

(46) Etacheri, V.; Marom, R.; Elazari, R.; Salitra, G.; Aurbach, D. *Energy Environ. Sci.* **2011**, *4*, 3243-3262.

3.2. Monolithically Integrated Photo-Rechargeable Portable Power Sources Based on Miniaturized Si Solar Cells and Printed Solid-State Lithium-Ion Batteries

3.2.1. Introduction

The forthcoming ubiquitous and smart energy era, which will involve the widespread popularity of electric vehicles, grid-scale stationary energy storage systems, and flexible electronics in our daily lives, has relentlessly pursued the need for high-performance energy generation systems, such as photovoltaic (PV) cells, fuel cells, and other renewable energy sources) systems, and energy storage systems, including lithium-ion batteries (LIBs), supercapacitors, and other rechargeable batteries[1-3]. Enormous progress has been made in both the development of energy generation and energy storage systems; however, the individual use of each system as a power source is not sufficient for fulfilling the ever-increasing demand for high energy/power density and ubiquitous mobility[4-6].

Combining energy generation and energy storage systems has been proposed as an ultimate solution to address the formidable challenges mentioned above[4,7,8]. For example, PV-battery systems first convert solar energy to electrical energy using the PV cells and then store the generated electrical energy in the batteries. Therefore, PV-battery systems can continuously operate electronic devices under light illumination whenever and wherever they are needed, which demonstrates their potential application as infinite energy sources that resolve both the energy density problems of batteries and the energy storage concerns for solar cells[4,5]. Notably, the application of PV-battery systems in electric vehicles has been recommended as a promising approach to overcome issues with the driving range of the vehicles and limitations with the charging stations[4].

Numerous research efforts have been devoted to developing high-performance PV-battery systems. One approach involves the simple interconnection of two independent PV and battery systems through external electrical wires[4,5,8-11]. However, the inevitable use of additional electrical wires/accessories resulted in an increase of the ohmic resistance and the complexity of the system design/dimensions. Another approach focused on fabricating single-body-structured, photo-rechargeable electric energy storage systems, in which one electrode of the energy conversion device acts simultaneously as an electrode for the storage of electrochemical energy[7,12-27]. From the perspective of system integration, most of the previously reported works have utilized dye-sensitized solar cells (DSSCs)[7,14-23] or organic solar cells[24,25]. However, the low power conversion efficiency (PCE) and non-optimized modulation of these PV cells have remained significant obstacles to achieving reliable photo-

charging performance. Meanwhile, only a few studies[7,20,21] have focused on the adoption of LIBs as a counterpart of PVs in comparison to PV-supercapacitor systems. Most notably, all of the PV-battery systems reported to date have used liquid electrolytes in batteries and DSSCs, thus giving rise to the deterioration of the long-term electrochemical performance, particularly for high-temperature operation, and resulting in safety failures.

Here, we demonstrate a new class of monolithically integrated, portable PV-battery systems (denoted by "SiPV-LIB") based on miniaturized crystalline Si photovoltaics (c-Si PVs) and printed solid-state bipolar LIBs as a facile and scalable system architecture strategy to address the aforementioned long-standing challenges of photo-rechargeable power sources. To enable the seamless architectural/electrical connection of the two different energy systems, an aluminium (Al) metal electrode of the c-Si PV module is simultaneously used as a current collector of the LIBs. The c-Si PV module is fabricated by interconnecting 25 units of Si mini-cells, and it shows a high output voltage of 14.1 V and a PCE of 15.8%. The solid-state LIB with a bipolar cell configuration is directly fabricated on the Al metal electrode of the c-Si PV module via an ultraviolet (UV) curing-assisted printing process. We recently reported on printed solid-state LIBs with versatile designs and their potential application as a new shape-conformable power source for flexible electronics and the Internet of Things (IOT)[28-30].

The single-unit SiPV-LIB device, in association with the well-designed physicochemical properties of its components, i.e., c-Si PV and solid-state bipolar LIBs, enables the realization of an unprecedented electrochemical performance that is far beyond that achievable by conventional PVs or LIBs alone; this includes the following: i) rapid photo-charging in less than 2 min with a high photo-electric conversion/storage efficiency of 7.61%; ii) photo-charging under illumination with an extremely low intensity (~8 mW cm^{-2}); iii) photo-charging/galvanostatic discharging at a high-temperature of 60°C; iv) continuous discharging at a current density of 28 C under sunlight illumination; and v) photo-generated electric energy that is capable of charging portable electronics, such as smartphones and MP3 players, under sunlight illumination.

3.2.2. Experimental

3.2.2.1. Design and Fabrication of Printed Solid-State Bipolar LIB

To prepare electrode pastes, an electrolyte precursor mixture composed of UV-curable ETPTA monomer (containing 1.0 wt.% 2-hydroxy-2-methyl-1-phenyl-1-propanone (HMPP) as a photoinitiator) and a high boiling point electrolyte (1M $LiPF_6$ in EC/PC with a ratio of 1/1 v/v), where the composition ratio of ETPTA/high boiling point electrolyte was 15/85 (w/w), was mixed with electrode active materials: $LiCoO_2$ (LCO, Umicore) for the cathode material, $Li_4Ti_5O_{12}$ (LTO, Süd Chemie) for the anode material and carbon black conductive additives. The electrode pastes were composed of the electrode mixture (electrode active materials/carbon black with a ratio of 8/2 (w/w))/SCE matrix precursor with a ratio of 6/4 (w/w). The LTO anode paste was printed on top of the Al metal electrode of the c-Si PV module using a stencil printing technique without any processing solvents, such as NMP or water, and then exposed to UV irradiation for a short time of less than 30 sec. UV irradiation was performed on the sample surface using a Hg UV-lamp (Lichtzen) with an irradiation peak intensity of approximately 2,000 mW cm^{-2}. Subsequently, the SCE paste (ETPTA/1M $LiPF_6$ in EC/PC/Al_2O_3 nanoparticles (average particle size ~300 nm) with a ratio of 7.5/42.5/50 (w/w/w)) was introduced on top of the LTO anode via the same stencil printing and UV curing process, which resulted in the formation of a solid-state SCE thin layer on the LTO anode. Then, the LCO cathode slurry was printed directly on the SCE layer/LTO anode unit and exposed to UV irradiation. After placing an Al current collector on top of the printed LCO cathode/printed SCE layer/printed LTO anode (C/S/A) assembly, a solid-state LIB unit cell was obtained. Another LIB unit cell with the same materials and composition ratio was introduced on top of the as-fabricated LIB unit cell using the same printing process, resulting in the fabrication of a bipolar stacked LIB cell (i.e., the two LIB unit cells were connected in series) on the c-Si PV module. Finally, the bipolar LIB cell was encapsulated with a ~27 µm-thick UV-cured hydrophobic polymer (PRO-001, Novacentrix) that served as the packaging material.

3.2.2.2. Photo-Electrochemical Chracterization of the SiPV-LIB Device

The c-Si PV module of the SiPV-LIB device was illuminated using a full-sun intensity solar simulator (Class AAA, Oriel Sol3A, Newport). Simultaneously, the in situ measurement of photo-charged voltages of the LIB was conducted using a potentiostat/galvanostat (VSP classic, Bio-Logic). After the LIB was fully photo-charged, it was galvanostatically discharged over a wide range of current densities. In particular, the discharge current density was varied from 28 (14 mA cm^{-2}) to 60 C under sunlight illumination to investigate the high-rate

discharge capability of the SiPV-LIB device. The thermal stability of the SiPV-LIB device was characterized by measuring the photo-charge/discharge profiles after storage for 1 hour at 25, 60, 90, and 120°C. The low-intensity light was illuminated by an AM 1.5G solar simulator with various grey filters. To fabricate a monolithically integrated smartcard, the SiPV-LIB device was inserted into a pre-cut credit card. Then, electric circuits were drawn on the back of the credit card using a commercial Ag pen to connect the SiPV-LIB device with a LED lamp. The SiPV-LIB device was electrically connected with a smartphone or MP3 player and its potential application as a supplementary portable power source was explored under sunlight illumination.

3.2.3. Results and Discussion

3.2.3.1. Monolithically Integrated SiPV-LIB Device and Electrochemical Performance of Bipolar LIB

The architectural uniqueness of the SiPV-LIB device was investigated, with a particular focus on the monolithic integration of the c-Si PV module and LIB cell (Figure 24a,b). The current/voltage tunable c-Si PV module (3 x 3 x 0.10 (cm/cm/cm)) was seamlessly connected with the printed solid-state bipolar LIB (3 x 3 x 0.03 (cm/cm/cm)) through an Al layer that acted as an electrical bridge, which eventually resulted in the formation of a monolithic tandem cell configuration. The redox reaction-based operating principle of the SiPV-LIB device is conceptually depicted in Figure 24b. Under light illumination, photocarriers such as electrons and holes are generated by the c-Si PV module. The photo-generated electrons collected by highly doped n-Si regions (n^+-Si, cathode) of the c-Si PV module move via the Al layer, which exhibits a bifunctional role as both a metal electrode (negative terminal) of the c-Si PV module and a current collector (negative terminal) of the LIB, to the LIB anode while the photo-generated holes accumulate at the opposite electrode (highly doped p-Si regions, anode) of the c-Si PV module, thus enabling the PV-induced charging of the LIB system. Specifically, electrons ejected from the c-Si PV module react with lithium ions at the LIB anode ($Li_4Ti_5O_{12} + xLi^+ + xe^- \rightarrow Li_{(4+x)}Ti_5O_{12}$). Simultaneously, free electrons are released from the positive terminal of the LIB cathode ($LiCoO_2 \rightarrow Li_{1-x}CoO_2 + xLi^+ + xe^-$) and then flow toward the positive terminal of the anode in the c-Si PV module through the external circuit, which results in recombination with the accumulated holes. This operating mechanism demonstrates the light-induced generation of photocarriers in the c-Si PV module, the separation of electrons and holes at the cathode/anode of the c-Si PV module, and electron storage in the LIBs of the c-Si PV-LIB device.
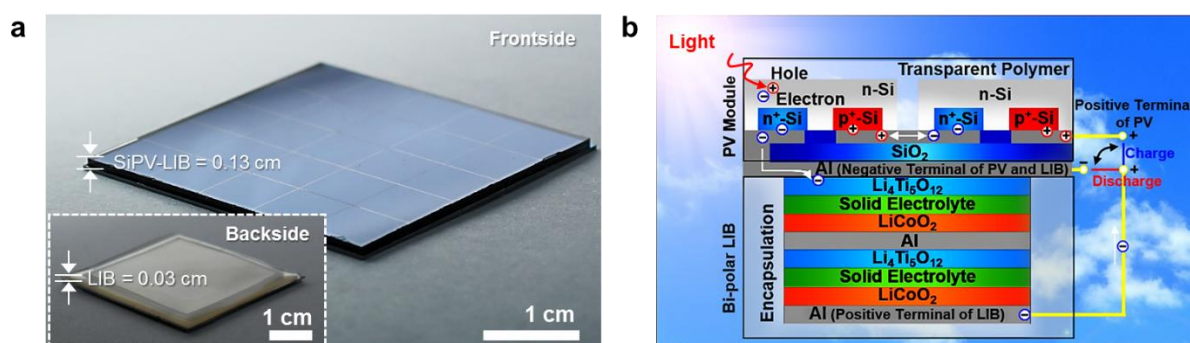

Figure 24. (a) Digital photograph (front) of SiPV-LIB device featuring a monolithic tandem cell configuration. Inset shows the back of the SiPV-LIB device. (b) Schematic representation of the internal structure and operating principle of the SiPV-LIB device under sunlight illumination.

Details on the fabrication procedure of the SiPV-LIB device are described below. The compact c-Si PV module was fabricated by interconnecting 25 units of c-Si mini-cells in series (the area of each cell was 0.36 cm^2) to generate high voltage and power, which are designed to be electrochemically compatible with the LIB. The fabrication and characteristics of the c-Si PV module will be further discussed in the following section. The solid-state LIB with a bipolar cell configuration was directly fabricated on the Al metal electrode of the as-prepared c-Si PV module through the UV curing-assisted printing method[30] (Figure 25a). The pastes of major LIB components (such as the anode, solid-state electrolyte, and cathode) were prepared for the printing process, and specific attention was paid to their rheological properties. The chemical structure and composition ratio of the component pastes and their preparation procedure are described in the experimental section. The anode paste (an active material mixture/electrolyte precursor mixture with a ratio of 60/40 (w/w)) was printed on top of the Al current collector and then exposed to UV irradiation for solidification. The anode paste consisted of an active material mixture of $Li_4Ti_5O_{12}$ (LTO)/carbon black with a ratio of 80/20 (w/w) and an electrolyte precursor mixture of ethoxylated trimethylolpropane triacrylate (ETPTA) monomer/1M $LiPF_6$ in ethylene carbonate (EC)/propylene carbonate (PC) with a ratio of 1/1 (v/v), i.e., 15/85 (w/w). Subsequently, the solid-state electrolyte paste (an Al_2O_3 nanoparticles/electrolyte precursor mixture with a ratio of 50/50 (w/w), where the electrolyte precursor mixture is the same as the aforementioned precursor mixture) and cathode paste (an active material mixture/electrolyte precursor mixture with a ratio of 60/40 (w/w), where the active material mixture is $LiCoO_2$ (LCO)/carbon black with a ratio of 80/20 (w/w) and the electrolyte precursor mixture is the same as the aforementioned precursor mixture) were subjected to printing and UV curing, which resulted in the printed solid-state LIB unit cell with a total thickness of ~ 110 µm (cathode + solid-state electrolyte + anode = 25 + 55 + 30 (µm)). The mass loadings of the cathode and anode were 3.8 mg cm^{-2} and 3.6 mg cm^{-2}, respectively. Meanwhile, another LIB unit cell with the same materials and composition ratio was introduced on top of the as-fabricated LIB unit cell using the same printing procedure; this resulted in the fabrication of a bipolar stacked LIB cell (i.e., the two LIB unit cells were connected in series) on the c-Si PV module. Finally, the bipolar LIB cell was encapsulated with a UV-cured hydrophobic polymer (PRO-001, Novacentrix)[33] that was used as a packaging material (thickness ~27 µm).
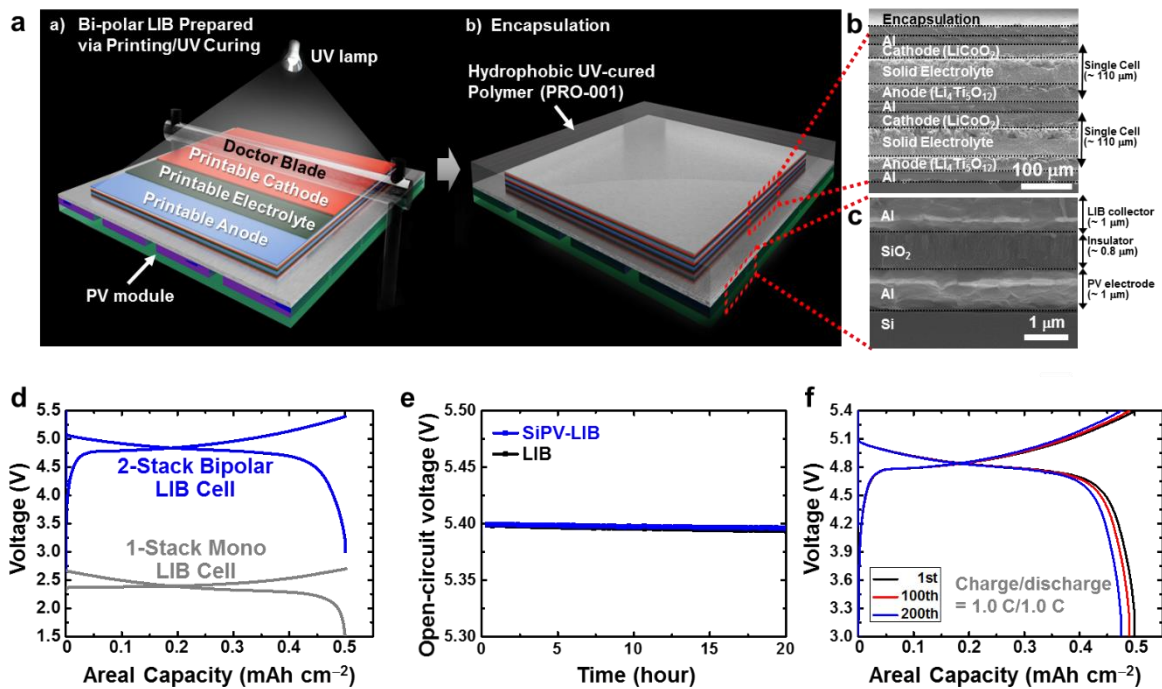
Figure 25. (a) Schematic illustration of the printing-based stepwise fabrication of the solid-state bipolar LIB cell directly on a c-Si PV module. (b, c) Cross-sectional SEM images of 2-stack bipolar LIB cell (b) and seamlessly unitized interface between bipolar LIB cell and c-Si PV module (c). (d) Galvanostatic charge/discharge profiles of 1-stack (grey lines) and 2-stack (blue lines) LIB cells. (e) OCV profiles of the SiPV-LIB device and bare bipolar LIB cell as a function of elapsed time. (f) Galvanostatic charge/discharge profiles of bipolar LIB cell in SiPV-LIB device as a function of the cycle number at a constant charge/discharge current density of 1.0 C/1.0 C.

The cross-sectional scanning electron microscopy (SEM) image in Figure 25b indicates that neither structural instability nor delamination was observed between the LIB cell components, which confirms the successful construction of the 2-stack bipolar LIB cell. Figure 25c shows the seamless unitization of the bipolar LIB cell with the c-Si PV module in the SiPV-LIB device. The electrochemical performance of the LIBs in the SiPV-LIB devices was independently investigated using a potentiostat/galvanostat without light illumination. The bipolar LIB cell exhibited a normal charge/discharge behaviour, which appeared to be similar to that of the mono LIB cell (Figure 25d). Intriguingly, the voltage plateaus of the bipolar LIB cell were observed at 4.7 V, which is two times higher than that of the mono LIB cell (a voltage plateau of 2.35 V determined by the voltage difference between the $Li_4Ti_5O_{12}$ anode and $LiCoO_2$ cathode[3,34-36]). To address a concern on self-discharge of the SiPV-LIB device, the open-circuit voltage (OCV) of the fully charged (i.e., 5.4 V) SiPV-LIB device was measured as a function of the elapsed time (Figure 25e). No appreciable difference in the OCV drop was found between the LIB cell of the SiPV-LIB device and bare bipolar LIB cell. The electrochemical performance of the bipolar LIB cell in the SiPV-LIB device was examined at

room temperature (Figure 25f), where the bipolar LIB cell was cycled between 3.0 and 5.4 V at a constant charge/discharge current density of 1.0/1.0 C. The bipolar LIB cell exhibits normal charge/discharge profiles and stable capacity retention (~95%) after 200 cycles. These results demonstrate that the printed solid-state bipolar LIB cell was unitized with the c-Si PV module without impairing its electrochemical performance.

3.2.3.2. Assembly and Photo-Electrochemical Characteristics of the Compact c-Si PV Module

The mini c-Si solar cell with a size of 0.36 cm^2 exhibited an average PCE of 15.7%, and an open-circuit voltage, short-circuit current density, and fill factor of 562 mV, 36.7 mA cm^{-2}, and 76.5%, respectively. To enable direct photo-charging of the bipolar LIB cell, the solar cells were interconnected in series to generate higher voltage than the bipolar LIBs (> 5 V). Prior to the interconnection, the as-fabricated solar cells were electrically isolated to prevent short-circuit failures because all of the cells were fabricated in a single Si wafer and they share the same Si layer. The master Si wafer was mechanically cut to detach the as-fabricated cells. However, the assembly of compact PV modules requires complex and customized processes in which the mini-cells are elaborately transferred onto the handling substrate by a motion-controlled stamp[37-39]. Here, we prepared the compact c-Si PV modules using UV-curable transparent films and tapes without utilizing additional transfer techniques (Figure 26a). To ensure electrical isolation, the as-fabricated wafer was attached to the UV-curable tape (DUV 190, DS Semicon)[40] and then mechanically cut by a dicing process. After cutting the wafer, the as-cut cells were embedded into the UV-curable transparent polymer (NOA 71, Norland Products, Inc.)[41], and then, the tape was detached from the polymer-embedded cells. As shown in Figure 26b, compact c-Si PV modules (3 × 3 × 0.10 (cm/cm/cm)) were achieved by interconnecting 25 cells with microscale gaps (widths of ~300 μm) between the cells. The cells were interconnected with each other simply by the thermal deposition of an Al film through a shadow mask (Figure 26c) because the microscale gaps formed during the dicing process were filled by the transparent UV-curable film to flatten the module surface. Figure 26d shows the voltage and maximum power output of the compact c-Si PV modules as a function of the number of mini-cells. The voltage and power output linearly increased with the number of mini-cells. The arrays of mini-cells can also be connected in parallel to create systems with high current. These results demonstrate that the compact c-Si PV module technique described above enabled the facile and versatile control of voltage and current, which is thus anticipated to widen its potential application areas.
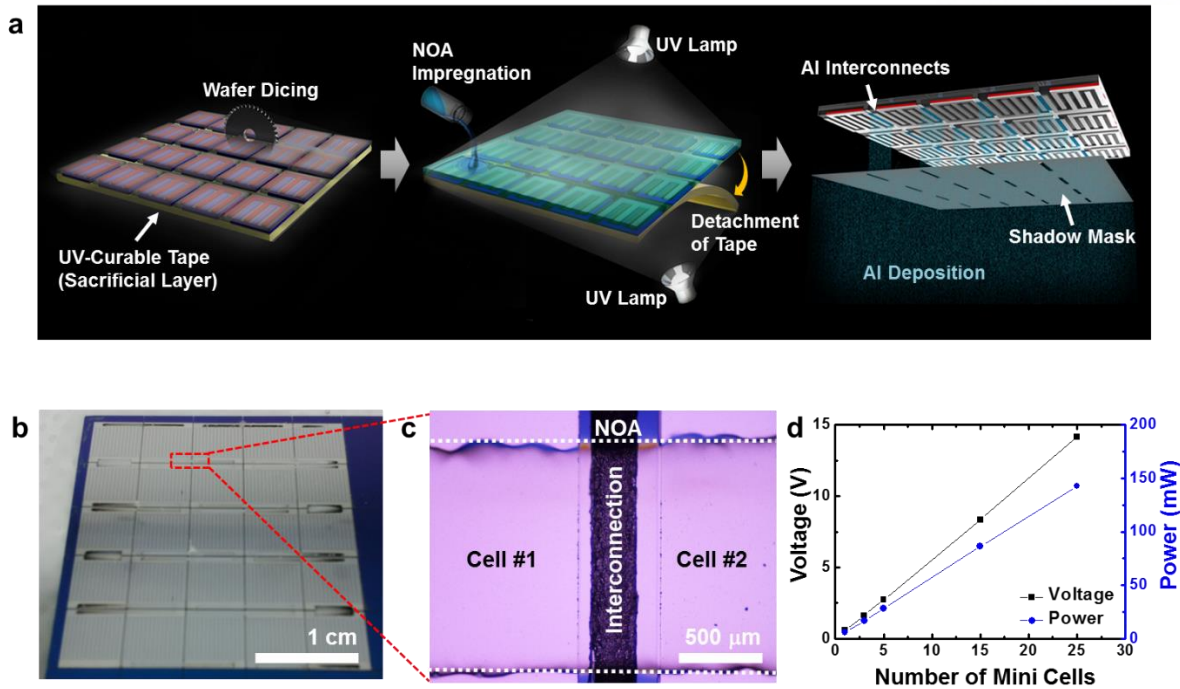
Figure 26. Assembly of high-voltage compact c-Si PV module. (a) Schematic illustration of transfer-free c-Si PV module assembly using UV-curable polymer and adhesive tapes. (b) Digital photograph (backside) of the compact c-Si PV module showing the interconnection of 25 solar cells in series. (c) Optical microscopy image (red square region in Fig. 2b) showing the interconnected solar cells formed by the thermally deposited Al film. (d) Voltage (black line) and power (blue line) of compact c-Si PV module as a function of the number of mini-cells.

3.2.3.3. Photo-Charging/Galvanostatic Discharging Behaviour of SiPV-LIB Devices

An equivalent circuit for the SiPV-LIB device upon photo-charging/discharging is schematically illustrated in Figure 27a. To create the equivalent circuit of the SiPV-LIB device, single diode model[42] and Rint model[43] were used for the SiPV and LIB, respectively. The photo-charging/galvanostatic discharging behaviour of the SiPV-LIB device was systematically investigated based on the understanding of this equivalent circuit. Figure 27b shows that the LIB cell of the SiPV-LIB device was rapidly photo-charged from 3.0 to 5.4 V for only 45 sec under a light intensity of 100 mW cm^{-2} (1 Sun), and then, without undergoing constant voltage (CV) mode, the fully charged LIB cell was galvanostatically discharged to 3 V at a discharge current rate of 1.0 C (= 0.5 mA cm^{-2}) for approximately 16 min. This photo-charging/galvanostatic discharging behaviour was steadily maintained for over 100 cycles (the capacity retention after 100 cycles > ~98%, Figure 27c). Notably, no appreciable loss in the photo-electric conversion/storage efficiency (PSE) was observed after the cycling test, which demonstrates the sustainable cycling performance of the SiPV-LIB device.
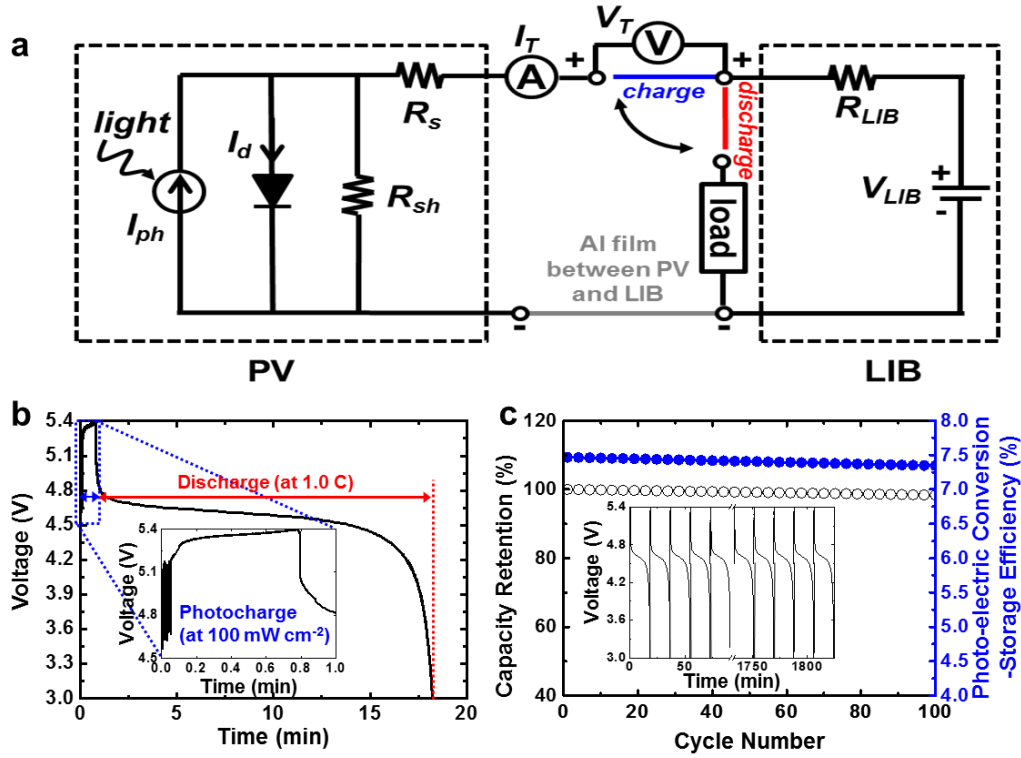
Figure 27. (a) Equivalent circuit of the SiPV-LIB device upon photo-charging/galvanostatic discharging. (b) Photo-charge/galvanostatic discharge profiles of the SiPV-LIB device, where the SiPV-LIB device was photo-charged from 3.0 to 5.4 V for 45 sec under a light intensity of 100 mW cm^{-2} (1 Sun) and was galvanostatically discharged to 3 V at a discharge current rate of 1.0 C (= 0.5 mA cm^{-2}). (c) Photo-charge/galvanostatic discharge cycling performance (expressed by the capacity retention (black line with hollow circle) and photo-electric conversion/storage efficiency (blue line with filled circles)) of SiPV-LIB device under a light intensity of 100 mW cm^{-2} (1 Sun) and a discharge current rate of 1.0 C (= 0.5 mA cm^{-2}). Inset shows photo-charge/galvanostatic discharge profiles with repeated cycling.

The photo-charged capacity was examined as a function of photo-charging time (at a light intensity of 100 mW cm^{-2}) and it exhibited a linear dependence on the light illumination time (Figure 28a). Additionally, the SiPV-LIB device was fully charged under sunlight illumination after only 2 min. The photo-charging behaviour of the SiPV-LIB device was further discussed by considering the following equation[44]:

$$I_T = I_{ph} - I_{dark}$$

$$= I_{ph} - I_0 \left[\exp\left(\frac{q\left(V_T + I_T\left(R_s + R_{LIB}\right) + V_{LIB}\right)}{k_B T} \right) - 1 \right] - \frac{\left(V_T + I_T\left(R_s + R_{LIB}\right) + V_{LIB}\right)}{R_{sh}} \qquad (1)$$

where I_T, I_{ph}, I_{dark}, I_0, V_T, V_{LIB}, R_s, R_{sh}, R_{LIB}, k_B, and T represent the total current of the PV-battery device, the PV photocurrent, the current of the PV-battery device in a dark environment, the reverse saturation current, the total voltage of the PV-battery device, the

internal voltage of the LIB, the PV series resistance, the PV shunt resistance, the internal resistance of the LIB, Boltzmann's constant, and temperature, respectively. In general, during the photo-charging of batteries, the negative current (I_{dark}) in Equation (1) tends to increase due to the increased voltage of the charged battery while the positive current (I_{ph}) generated from the c-Si PV module is maintained at the same level[9]. As a result, I_T is reduced when the voltage of the photo-charged battery is increased. In contrast, for the SiPV-LIB device, the LIB can be steadily and rapidly photo-charged due to the SiPV module that is designed to consistently generate a higher voltage (V_T) than the operating voltage (V_{LIB}) of the LIB.

An important factor for describing the photo-induced energy conversion and storage capability of the SiPV-LIB device is the photo-electric conversion/storage efficiency (PSE), which can be quantitatively estimated by the equation shown below:

$$PSE = \frac{E_{LIB}}{E_{in}} = \frac{\int_0^{t_{discharge}} VI\,dt}{P_{in}t_{charge}A} \qquad (2)$$

where I is the constant galvanostatic discharge current density of 0.5 mA cm^{-2}, $t_{discharge}$ is the discharge time, E_{LIB} is the energy stored in the LIB, E_{in} is the incident solar energy, P_{in} is the incident light power density, t_{charge} is the illumination time during photo-charging, and A is the area of the PV module. As shown in Figure 28a, the PSE of the SiPV-LIB device increased rapidly from 5% to 7.23% in a duration that was less than the photo-charging time of 30 sec, and then, it reached a saturation value of 7.61% after 60 sec. More notably, this PSE value (7.61%) of the SiPV-LIB device was higher than those of previously reported PV-battery systems with similar single-unit architecture (Figure 28b), which underscores its superior performance as a new photo-rechargeable power source.
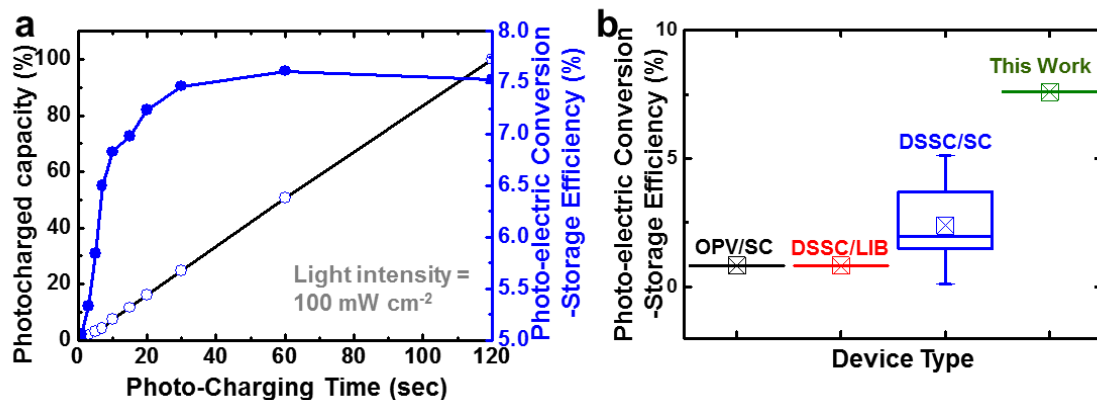

Figure 28. (a) Photo-charge capacity (black line with hollow circles) and photo-electric conversion/storage efficiency (blue solid line with filled circles) of the SiPV-LIB device as a function of photo-charging time. (b) Comparison of photo-electric conversion/storage efficiencies between this work (the SiPV-LIB device) and previously reported PV-battery

systems with similar single-unit architectures (organic solar cell (OPV)-supercapacitor[24], DSSC-LIB[20], and DSSC-supercapacitor[14-16,18,19,27,52]).

To highlight and visualize the rapid photo-charging capability and the unique nature of the design described above, the SiPV-LIB device was combined with a smartcard and its electrochemical performance was examined (Figure 29a). The SiPV-LIB device was monolithically embedded into the smartcard, and its low thickness of 0.13 cm ensured that there was no significant impact on the overall dimension and shape of the smartcard. The LIB of the SiPV-LIB device was photo-charged under a light intensity of 100 mW cm^{-2}. Notably, the SiPV-LIB device was capable of lighting up a LED lamp mounted in the smartcard only after photo-charging was performed for 20 sec. This result demonstrates the potential for applying the SiPV-LIB device as an aesthetically unitized power source for use in future IOTs and wearable electronics.

The discharge rate capability of the SiPV-LIB device, after photo-charging was performed for 120 sec under a light intensity of 100 mW cm^{-2}, was examined over a wide range of discharge current densities between 0.5 and 5.0 C (Figure 29b). Similar to discharge behaviours of traditional LIB cells[4], the discharge capacities of the SiPV-LIB device decreased as the discharge current density increased from 0.5 to 5.0 C. Intriguingly, a satisfactory level of the discharge capacity was observed even at a fast discharge rate of 5.0 C, which indicates that the SiPV-LIB device can be readily applied in a variety of fields including electric vehicles that require high operating currents.

The photo-induced energy conversion capability of the SiPV-LIB device was investigated to explore its versatile use under a wide range of light intensity conditions, including in an indoor environment. Even at an extremely low light intensity of 8 mW cm^{-2}, which corresponds to the intensity in a dimly-light living room[45], the output voltage of the SiPV-LIB device was observed to be over 12.0 V, which is much higher than the voltage ($\leq$5.4 V) of the LIB. To attain quantitative information on the photo-electrochemical performance of the SiPV-LIB device, the photo-charge/galvanostatic discharge behaviour of the SiPV-LIB device at a fixed discharge current rate of 1.0 C was investigated as a function of the light intensity (at 8, 40, and 100 mW cm^{-2}). Figure 29c shows that the SiPV-LIB device was successfully photo-charged even under a low light intensity of 8 mW cm^{-2} and then galvanostatically discharged for 60 min, although the lower light intensity, which yielded a lower photo-current of the SiPV module, required a longer photo-charging time. As the light intensity decreased, a slight reduction in PSE was observed due to the decreased PCE of the SiPV module under lower light intensity. Meanwhile, a lower light intensity led to a decrease

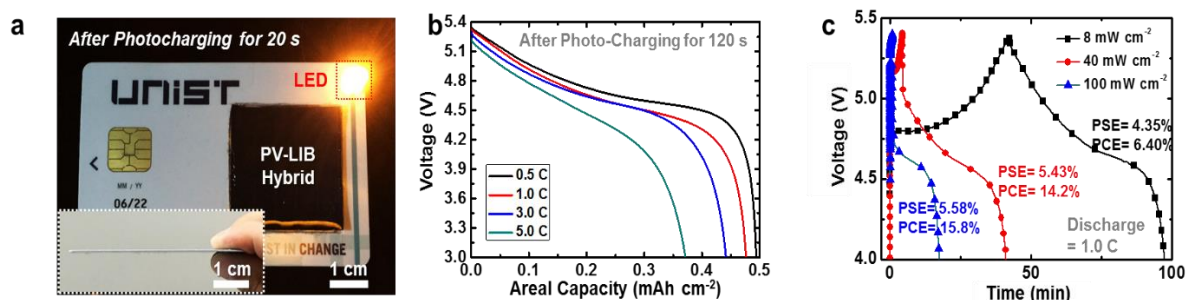in the PCE of the c-Si PV module, thus resulting in a slight reduction in the PSE of the SiPV-LIB device.

Figure 29. (a) Digital photograph showing the operation of the SiPV-LIB-embedded smartcard. Inset shows the overall thickness of the resulting smartcard. (b) Galvanostatic discharge rate capability of the SiPV-LIB device (after photo-charging for 120 sec under a light intensity of 100 mW cm^{-2}) over a wide range of discharge current densities from 0.5 to 5.0 C. (c) Photo-charging/galvanostatic discharging profiles of SiPV-LIB devices at a fixed discharge current rate of 1.0 C as a function of light intensity (8, 40, and 100 mW cm^{-2}).

One formidable challenge that faces photo-rechargeable electric energy storage systems is their thermal instability because long-term exposure to sunlight tends to trigger heat-induced structural disruption and performance degradation of the systems. This problem becomes more pronounced in batteries or DSSCs that use liquid-state electrolytes that are vulnerable to elevated temperature conditions. After the SiPV-LIB device was placed in a hot oven for 1 h with the temperature varied from 60 to 120°C, its dimensional change was monitored. Neither swelling nor shrinkage was observed for the Si-PV LIB device over the entire range of temperatures examined in this study (Figure 30a). The thermal stability of the SiPV-LIB device was further evaluated as a function of the number of photo-charge/discharge cycles under a light intensity of 100 mW cm^{-2} and a discharge current rate of 1.0 C at various operating temperatures. The SiPV-LIB device showed good capacity retention (> 95%) after 100 cycles at 60°C as well as 25 and 40°C (Figure 30b). This excellent thermal tolerance, which is attributed to the adoption of the crystalline Si PV module and the solid-state LIB, is a salient advantageous feature of the SiPV-LIB device compared to previously reported photo-rechargeable electric energy storage systems that use liquid electrolytes[17,20].
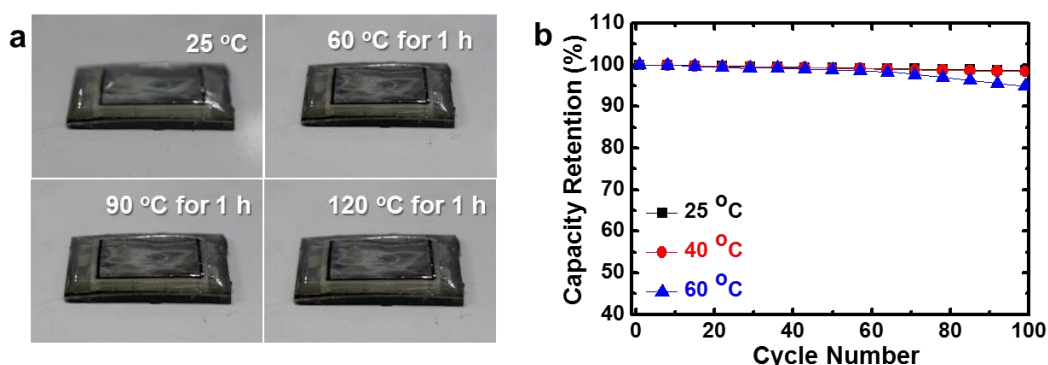
Figure 30. (a) Digital photographs showing the dimensional change of the SiPV-LIB device (with a focus on the LIB part) after it is placed in a hot oven for 1 h with the temperature varied from 60 to 120°C. (b) Capacity retention of SiPV-LIB device with cycling as a function of temperature under a light intensity of 100 mW cm^{-2} and a discharge current rate of 1.0 C.

3.2.3.4. Discharge Performance under Sunlight Illumination of the SiPV-LIB Device

The discharge performance of the SiPV-LIB device was investigated in detail under sunlight illumination at an intensity of 100 mW cm^{-2}. Figure 31a shows the discharge profiles of the SiPV-LIB device as a function of discharge current density (28, 30, 48, and 60 C). Amazingly, no appreciable loss in the discharge voltage of the SiPV-LIB device was observed in the measured time at the high discharge current density of 28 C (Figure 31a). In addition, the SiPV-LIB device showed a detectable discharge capacity even under the extremely fast discharge current density of 60 C. However, the SiPV-LIB device placed in a dark environment showed poor discharge behaviour at rapid discharge current rates (the inset of Figure 31a), which is commonly observed for conventional LIBs.

Considering that electric vehicle batteries require high discharge current densities to deliver the high power needed for operating various driving modes[46,47], the aforementioned discharge performance of the SiPV-LIB device is highly appealing because the results shown in Figure 31a indicate that, if new large-sized photo-rechargeable power sources with sufficient energy density could be fabricated using the concept of the SiPV-LIB device proposed herein, they may continuously operate electric vehicles with a current load below 28 C under sunlight illumination.

Such an unusual discharge behaviour of the SiPV-LIB device is ascribed to the remarkable reduction in the internal resistance ($R_{internal}$) of the LIB under sunlight illumination compared to that in the dark environment (Figure 31b); here, $R_{internal}$[48] was determined using Ohm's law by measuring the difference in the initial voltage between the voltage at open-circuit and the voltage at a given current density. Driven by electrons generated by the c-Si PV

module, a significant difference in the electron concentration may be developed between the c-Si PV module and the LIB cell, thereby boosting the transport of electrons from the c-Si PV module (with a high electron concentration) to the LIB (with a low electron concentration). As a result, electron migration towards the LIB could be facilitated, which results in the decrease of $R_{internal}$. This result for the SiPV-LIB device appears similar to the transport phenomena of plasmon-induced hot electrons in metal/Si Schottky junction where a high concentration of electrons can overcome the energy barrier to produce current for optoelectronics[49-51]. Further studies are required to better understand this unusual discharge behaviour of the SiPV-LIB device under sunlight illumination.
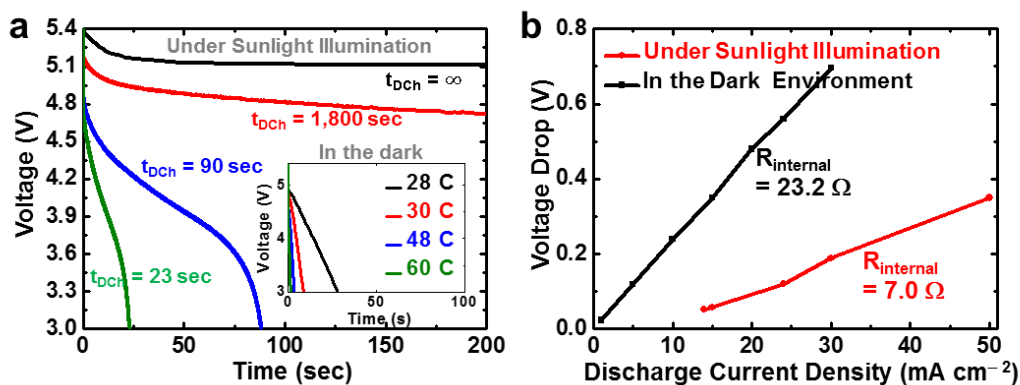

Figure 31. (a) Galvanostatic discharge profiles of the SiPV-LIB device as a function of discharge current density (28, 30, 48, and 60 C). Inset shows the discharge profiles of the SiPV-LIB device in the dark environment. (b) Internal resistances ($R_{internal}$) of LIB cells in SiPV-LIB devices under sunlight illumination (red line) and in the dark environment (black line).

This exceptional galvanostatic discharge performance of the SiPV-LIB device is expected to make remarkable advances in the Ragone plot, which depicts the relationship between energy and power densities. The volumetric/gravimetric energy and power densities of the SiPV-LIB device were determined by considering the weight/volume of the major components while the contribution of the packaging substances was excluded. Intriguingly, under sunlight illumination, the SiPV-LIB device showed significant improvements in the volumetric/gravimetric energy and power densities without altering the electrochemically active materials (Figure 32), which lay far beyond the results achievable with the LIBs alone (i.e., obtained in the dark environment.). The target value of energy/power density required for long-range electric vehicles (operating for at least 300 miles), which was announced by the US Department of Energy[46], was also marked on the Ragone plot. Due to the noteworthy galvanostatic discharging under sunlight illumination, the SiPV-LIB device satisfied the challenging energy/power density requirements for electric vehicles. Most notably, limitless energy density was achieved at power densities below 1,000 W L^{-1}, which demonstrates the

potential utilization of the SiPV-LIB device as a solar-driven infinite power source for electric vehicles.
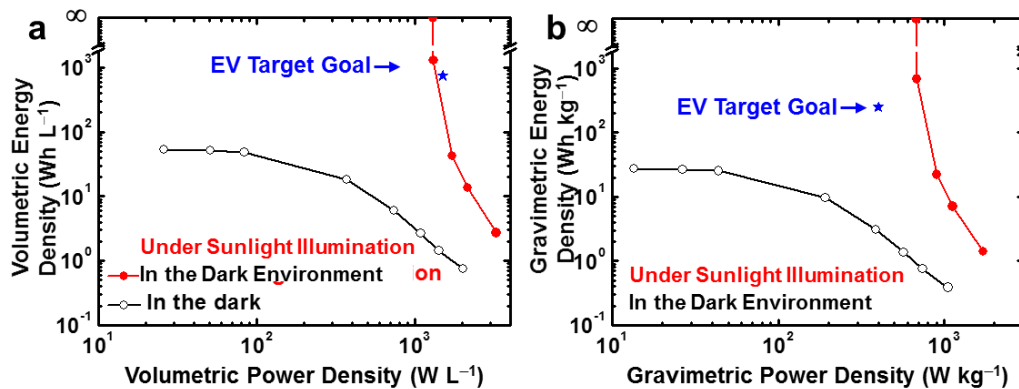
Figure 32. Volumetric (a) and Gravimetric (b) ragone plots of SiPV-LIB devices under sunlight illumination (red line) and in the dark environment (black line). The EV target goal announced by the US Department of Energy[46] is marked by the star symbol.

The SiPV-LIB device was connected to various portable electronics to explore its practical use. A smartphone (Figure 33a) and a MP3 player (Figure 33b) were successfully charged by the SiPV-LIB device under sunlight illumination. This demonstrates that the SiPV-LIB device can be used as a portable supplementary battery (one that requires no charging). In addition, we anticipate that integration of the SiPV-LIB device into electronic appliances can contribute to the realization of charge-less mobile electronics that operate under sunlight illumination.

Figure 33. Digital photograph showing a smartphone (a) and MP3 player (b) that are being charged by the SiPV-LIB device under sunlight illumination.

3.2.4. Conclusion

In summary, we demonstrated the monolithically integrated SiPV-LIB device as a new class of photo-rechargeable portable power sources with exceptional photo-electrochemical perfo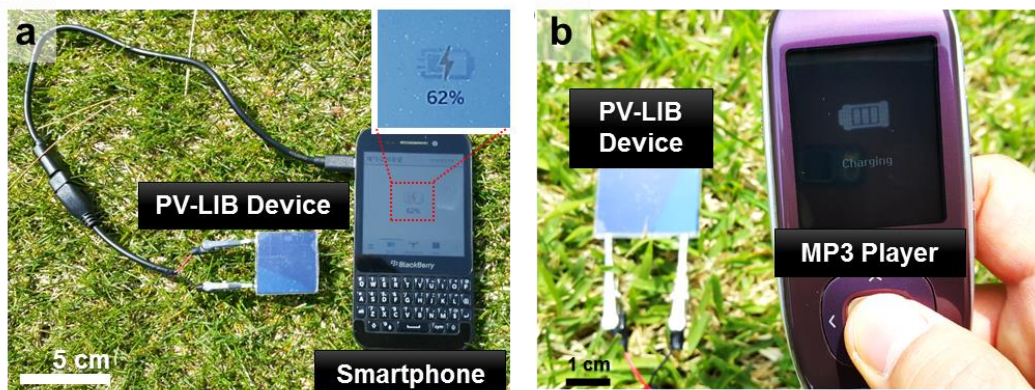rmance and design compactness. The solid-state bipolar LIB cell was directly fabricated on the Al electrode of the c-Si PV module (25 units of 0.36 cm^2 Si cells, output voltage = 14.1 V and PCE = 15.8%) through an in-series printing process, which resulted in the development of a structurally unitized/electrically connected SiPV-LIB device with dimensions of $3 \times 3 \times 0.13$ (cm/cm/cm). Driven by the unique device architecture and well-tailored physicochemical properties of the c-Si PV module and the LIB cell, the SiPV-LIB device exhibited unprecedented improvements in photo-charging (rapid charging in less than 2 min with a photo-electric conversion/storage efficiency of 7.61%), discharge rate capability (continuous discharging at a rapid rate of 28 C), and photo-charge/galvanostatic discharge cycling performance (capacity retention > ~98% after 100 cycles). In addition, the SiPV-LIB device showed decent photo-rechargeable electric energy storage behaviour even at a high temperature of 60°C and an extremely low light intensity of 8 mW cm^{-2}. More importantly, limitless energy at power densities below 1,000 W L^{-1} was produced by the SiPV-LIB device under sunlight illumination, which highlights its potential application as a solar-driven infinite energy conversion/storage system for use in electric vehicles and portable electronics. The SiPV-LIB device presented herein shows great potential as a photo-rechargeable mobile power source that will play a pivotal role in the future era of ubiquitous electronics.

3.2.5. References

(1) N. J. Jeon, J. H. Noh, W. S. Yang, Y. C. Kim, S. Ryu, J. Seo and S. I. Seok, *Nature*, 2015, **517**, 476-480.

(2) A. Polman, M. Knight, E. C. Garnett, B. Ehrler and W. C. Sinke, *Science*, 2016, **352**, aad4424.

(3) S. Xu, Y. Zhang, J. Cho, J. Lee, X. Huang, L. Jia, J. A. Fan, Y. Su, J. Su, H. Zhang, H. Cheng, B. Lu, C. Yu, C. Chuang, T. I. Kim, T. Song, K. Shigeta, S. Kang, C. Dagdeviren, I. Petrov, P. V. Braun, Y. Huang, U. Paik and J. A. Rogers, *Nat. Commun.*, 2013, **4**, 1543.

(4) J. Xu, Y. Chen and L. Dai, *Nat. Commun.*, 2015, **6**, 8103.

(5) D. Schmidt, M. D. Hager and U. S. Schubert, *Adv. Energy Mater.*, 2016, **6**, 1500369.

(6) J. H. Lee, J. Kim, T. Y. Kim, M. S. Al Hossain, S. W. Kim and J. H. Kim, *J. Mater. Chem. A*, 2016, **4**, 7983-7999.

(7) M. Yu, X. Ren, L. Ma and Y. Wu, *Nat. Commun.*, 2014, **5**, 5111.

(8) Z. Gao, C. Bumgardner, N. Song, Y. Zhang, J. Li and X. Li, *Nat. Commun.*, 2016, **7**, 11586.

(9) T. L. Gibson and N. A. Kelly, *J. Power Sources*, 2010, **195**, 3928-3932.

(10) K. Wedege, J. Azevedo, A. Khataee, A. Bentien and A. Mendes, *Angew. Chem. Int. Ed.*, 2016, **55**, 7142-7147.

(11) A. E. Ostfeld, A. M. Gaikwad, Y. Khan and A. C. Arias, *Sci. Rep.*, 2016, **6**, 26122.

(12) A. K. Pandey, P. C. Deakin, R. D. Jansen-Van Vuuren, P. L. Burn and I. D. W. Samuel, *Adv. Mater.*, 2010, **22**, 3954-3958.

(13) J. Xu, H. Wu, L. Lu, S.-F. Leung, D. Chen, X. Chen, Z. Fan, G. Shen and D. Li, *Adv. Func. Mater.*, 2014, **24**, 1840-1846.

(14) X. Zhang, X. Huang, C. Li and H. Jiang, *Adv. Mater.*, 2013, **25**, 4093−4096.

(15) T. Chen, L. Qiu, Z. Yang, Z. Cai, J. Ren, H. P. Li, H. Lin, X. M. Sun and H. S. Peng, *Angew. Chem. Int. Ed.*, 2012, **51**, 11977-11980.

(16) X. Chen, H. Sun, Z. Yang, G. Guan, Z. Zhang, L. Qiu and H. Peng, *J. Mater. Chem. A*, 2014, **2**, 1897-1902.

(17) M. A. Mahmoudzadeh, A. R. Usgaocar, J. Giorgio, D. L. Officer, G. G. Wallace and J. D. W. Madden, *J. Mater. Chem. A*, 2016, **4**, 3446-3452.

(18) Z. Yang, L. Li, Y. Luo, R. He, L. Qiu, H. Lin and H. Peng, *J. Mater. Chem. A*, 2013, **1**, 954-958.

(19) Y. Fu, H. Wu, S. Ye, X. Cai, X. Yu, S. Hou, H. Kafafy and D. Zou, *Energy Environ. Sci.*, 2013, **6**, 805-812.

(20) W. Guo, X. Xue, S. Wang, C. Lin and Z. L. Wang, *Nano Lett.*, 2012, **12**, 2520-2523.

(21) N. Li, Y. Wang, D. Tang and H. Zhou, *Angew. Chem. Int. Ed.*, 2015, **54**, 9271-9274.

(22) A. P. Cohn, W. R. Erwin, K. Share, L. Oakes, A. S. Westover, R. E. Carter, R. Bardhan and C. L. Pint, *Nano Lett.*, 2015, **15**, 2727-2731.

(23) C. Shi, H. Dong, R. Zhu, H. Li, Y. Sun, D. Xu, Q. Zhao and D. Yu, *Nano Energy*, 2015, **13**, 670-678.

(24) G. Wee, T. Salim, Y. M. Lam, S. G. Mhaisalkar and M. Srinivasan, *Energy Environ. Sci.*, 2011, **4**, 413-416.

(25) Z. Zhang, X. Chen, P. Chen, G. Guan, L. Qiu, H. Lin, Z. Yang, W. Bai, Y. Luo and H. Peng, *Adv. Mater.*, 2014, **26**, 466−470.

(26) H. Li, Q. Zhao, W. Wang, H. Dong, D. Xu, G. Zou, H. Duan and D. Yu, *Nano Lett.*, 2013, **13**, 1271-1277.

(27) H.-W. Chen, C.-Y. Hsu, J.-G. Chen, K.-M. Lee, C.-C. Wang, K.-C. Huang and K.-C. Ho, *J. Power Sources*, 2010, **195**, 6225-6231.

(28) E.-H. Kil, K.-H. Choi, H.-J. Ha, S. Xu, J. A. Rogers, M. R. Kim, Y.-G. Lee, K. M. Kim, K. Y. Cho and S.-Y. Lee, *Adv. Mater.*, 2013, **25**, 1395−1400.

(29) S.-H. Kim, K.-H. Choi, S. J. Cho, E.-H. Kil and S.-Y. Lee, *J. Mater. Chem. A*, 2013, **1**, 4949−4955.

(30) S.-H. Kim, K.-H. Choi, S.-J. Cho, S. Choi, S. Park and S.-Y. Lee, *Nano Lett.*, 2015, **15**, 5168−5177.

(31) H.-D. Um, I. Hwang, N. Kim, Y. J. Yu, M. Wober, K.-H. Kim and K. Seo, *Adv. Mater. Interfaces*, 2015, **2**, 1500347.

(32) K.-H. Choi, J. Yoo, C. K. Lee and S.-Y. Lee, *Energy Environ. Sci.*, 2016.

(33) Y. L. Kong, I. A. Tamargo, H. Kim, B. N. Johnson, M. K. Gupta, T. W. Koh, H. A. Chin, D. A. Steingart, B. P. Rand and M. C. McAlpine, *Nano Lett.*, 2014, **14**, 7017−7023.

(34) K. Yoshima, H. Munakata and K. Kanamura, *J. Power Sources*, 2012, **208**, 404-408.

(35) N. Schweikert, R. Heinzmann, A. Eichhofer, H. Hahn and S. Indris, *Solid State Ionics*, 2012, **226**, 15−23.

(36) E. Ferg, R. J. Gummow, A. Dekock and M. M. Thackeray, *J. Electrochem. Soc.*, 1994, **141**, L147−L150.

(37) A. J. Baca, K. J. Yu, J. Xiao, S. Wang, J. Yoon, J. H. Ryu, D. Stevenson, R. G. Nuzzo, A. A. Rockett, Y. Huang and J. A. Rogers, *Energy Environ. Sci.*, 2010, **3**, 208-211.

(38) Y. Yao, E. Brueckner, L. Li and R. Nuzzo, *Energy Environ. Sci.*, 2013, **6**, 3071-3079.

(39) J. Yoon, A. J. Baca, S. I. Park, P. Elvikis, J. B. Geddes, L. F. Li, R. H. Kim, J. L. Xiao, S. D. Wang, T. H. Kim, M. J. Motala, B. Y. Ahn, E. B. Duoss, J. A. Lewis, R. G. Nuzzo, P. M. Ferreira, Y. G. Huang, A. Rockett and J. A. Rogers, *Nat. Mater.*, 2008, **7**, 907-915.

(40) K. Ebe, H. Seno and K. Horigome, *J. Appl. Polym. Sci.*, 2003, **90**, 436−441.

(41) S. Nam, M. Song, D. H. Kim, B. Cho, H. M. Lee, J. D. Kwon, S. G. Park, K. S. Nam, Y. Jeong, S. H. Kwon, Y. C. Park, S. H. Jin, J. W. Kang, S. Jo and C. S. Kim, *Sci. Rep.*, 2014, **4**, 4788.

(42) J. Nelson, *The Physics of Solar Cells*, Imperial College Press, London, UK, 2003.

(43) V. H. Johnson, *J. Power Sources*, 2002, **110**, 321−329.

(44) A. Ortiz-Conde, F. J. García Sánchez and J. Muci, *Solid-State Electron.*, 2000, **44**, 1861−1864.

(45) D. L. Butler and P. M. Biner, *Environ. Behav.*, 1987, **19**, 695−721.

(46) R. Garcia-Valle and J. A. P. Lopes, *Electric Vehicle Integration into Modern Power Networks*, Springer, NY, USA, 2013.

(47) K. S. Kang, Y. S. Meng, J. Breger, C. P. Grey and G. Ceder, *Science*, 2006, **311**, 977−980.

(48) Y. Li, Z. Huang, K. Huang, D. Carnahan and Y. Xing, *Energy Environ. Sci.*, 2013, **6**, 3339−3345.

(49) A. Akbari and P. Berini, *Appl. Phys. Lett.*, 2009, **95**, 021104.

(50) I. Goykhman, B. Desiatov, J. Khurgin, J. Shappir and U. Levy, *Nano Lett.*, 2011, **11**, 2219-2224.

(51) D. W. Peters, *Proc. IEEE*, 1967, **55**, 704−705.

(52) K. Jost, G. Dion and Y. Gogotsi, *J. Mater. Chem. A*, 2014, **2**, 10776-10787.

CHAPTER IV. Direct-Writable, Solid-State Flexible Batteries with *in-plane* Architecture

4.1. All-Inkjet-Printed, Solid-State Flexible Supercapacitors on Paper

4.1.1. Introduction

The rapidly emerging flexible/wearable electronics and Internet of Things (IoT), which are anticipated to bring unforeseen ubiquitous innovations in our daily lives, essentially require the relentless pursuit of advanced power sources with various form factors and aesthetic diversity[1-3].

Conventional rechargeable energy storage systems, including commercial state-of-the-art lithium-ion batteries and supercapacitors, have employed sheet-type electrodes, separator membranes, and liquid electrolytes as the core components and also shown (cylindrical-/rectangular-shaped) stereotypical forms fabricated through a winding or stacking process. Such traditional cell components and assembly have pushed the power sources to lack a variety of form factors and flexibility. A variety of flexible power sources, which can be bendable, foldable, and stretchable, has been investigated[4-7]; such studies have mainly focused on nanostructured electrode materials, paper (or textile)-mediated nonmetallic current collectors, and functional electrolytes. Despite such enormous research efforts, slurry-casted electrodes, liquid-state electrolytes, and (winding/stacking-based) cell assemblies are still adopted in many systems, thus imposing challenges on the diversification of the design of the power sources[8-12]. New cell manufacturing processes based on multistep spraying and screen (or stencil or blade) printing have been suggested as a drastic approach to address the aforementioned issues[13-20]. Some meaningful progress in the development of novel cell designs and architectures have been reported; however, the majority of these works required the use of pre-designed masks, supplementary spatial alignments, and liquid electrolytes as an ionic medium.

Here, we demonstrate a new class of solid-state flexible power sources that are fabricated directly on conventional A4 paper using a typical desktop inkjet printer. Activated carbon (AC)-based electric double-layer supercapacitors (SCs)[21-23] are chosen as a model power source to demonstrate the feasibility and practical validity of the proposed concept. Ionic liquid (1-butyl-3-methylimidazolium tetrafluoroborate, [BMIM][BF$_4$]) /ultraviolet (UV)-cured ethoxylated trimethylolpropane triacrylate (ETPTA)-based gel polymer electrolytes are incorporated to produce the solid-state SCs. Inkjet printing has been widely used as a facile and effective tool to write letters or draw patterns/figures on various substrates, including paper and films, due to the simplicity/versatility of its process and the high resolution of the resulting images[24,25]. The applications of inkjet printing are currently expanding from traditional office uses to high-fidelity electronics, displays, and sensors[26-29]. However, only a few works involved inkjet-printed energy storage systems, including three-dimensional (3D) Zn-AgO microbatteries[30], LiCoO$_2$/Li$_4$Ti$_5$O$_{12}$ lithium-ion batteries[31], 3D interdigitated LiFePO$_4$/Li$_4$Ti$_5$O$_{12}$

lithium-ion microbatteries[32], and thin-film supercapacitors[33-37]. In those battery systems, only the electrodes were inkjet-printed, and liquid electrolytes (introduced via dipping or injection) were still employed in predetermined cell geometries.

The salient features of the inkjet-printed SCs proposed herein are their monolithic integration with paper substrates and the high-resolution print images comparable to those produced with conventional black/color inks. In other words, the inkjet-printed SCs look like typical inkjet-printed letters or figures commonly found in office documents. As key-enabling technologies to achieve this goal, cellulose nanofibril (CNF)-mediated nanoporous mats and interwelded Ag nanowire (NW) networks are introduced through a conventional inkjet printing process to serve as a primer layer on top of A4 paper and to improve the electrical conductivity of the resulting electrodes, respectively. As a consequence, a variety of inkjet-printed, solid-state SCs featuring computer-designed artistic patterns/letters are successfully fabricated on A4 paper and are aesthetically unitized with other inkjet-printed digital images and smart glass cups.

4.1.2. Experimental

4.1.2.1. CNF Suspension for Inkjet-Printed CNF Nanomat as a Primer Layer on A4 Paper

The CNF suspension was produced from the repeated high-pressure homogenization of wood cellulose powders (particle size ~ 45 μm, KC Flock, Nippon Paper Chemicals) in water. The details on the preparation procedure of the CNF suspension were provided in our previous publications[38,39]. The as-prepared CNF suspension was diluted with water to vary the CNF concentration in the range of 0.1-1.0 mg mL^{-1}.

4.1.2.2. SWNT/AC and Ag NW Inks for Inkjet-Printed Electrodes

The AC powders (particle size ~ 50 nm, Vulcan, Fuel Cell Store) were mixed with the SWNTs (Tubal^{TM}, OCSIAL) in water, to which 1.0 wt% sodium dodecylbenzene sulfonate (SDBS) was added as a dispersing agent. The SWNT/AC mixtures in water were subjected to centrifugation (at 10,000 rpm for 1 h) to remove large-sized particles and agglomerates, resulting in SWNT/AC inks with a suitable viscosity (~ 20 cP at a shear rate of 1 s^{-1}) for the inkjet printing process. The Ag NW (DT-AGNW-N30-1DI, Ditto Technology Co.) suspension (solid content = 0.25 wt%) was prepared in water/IPA (= 1/1 (v/v)) and then subjected to a sonication-driven scission process[40] to avoid clogging concern induced by long Ag NWs with a high aspect ratio.

4.1.2.3. Electrolyte Inks for Inkjet-Printed Solid-State Electrolytes

The ionic liquid ([BMIM][BF$_4$]) was mixed with ETPTA[13,14] (incorporating 1.0 wt % HMPP as a photoinitiator) in a solvent (ethanol or water). The [BMIM][BF$_4$]/ETPTA (= 85/15 (w/w)) mixture was exposed to UV irradiation (Hg UV-lamp, irradiation peak intensity = 2,000 mW cm^{-2}, Lichtzen), resulting in a crosslinked solid-state gel polymer electrolyte.

4.1.2.4. Fabrication of CNF-Paper

The CNF-paper was fabricated directly onto A4 paper using a commercial desktop inkjet printer (HP Deskjet 1010). The inkjet printing of the CNF suspension (concentration = 0.3 mg mL^{-1}) on top of the A4 paper resulted in the inkjet-printed (wet-state) CNF layer. To improve the porous structure of the CNF layer, a solvent mixture of ethanol/acetone (= 1/1 (v/v)) was subsequently applied onto the (wet-state) CNF layer via inkjet printing, eventually yielding a CNF nanomat with a highly developed nanoporous structure.

4.1.2.5. Fabrication of Inkjet-Printed SCs

To fabricate the SC electrodes, the SWNT/AC inks were inkjet-printed on the CNF-paper substrate, followed by inkjet printing of the Ag NW inks. The inkjet-printed SC electrodes were subjected to UV irradiation to allow for the photonic sintering of the Ag NWs, leading to the formation of highly interwelded Ag NW networks. On top of the electrodes, the [BMIM][BF$_4$]/ETPTA mixture was inkjet-printed and then consecutively subjected to a UV-curing reaction to produce the solid-state electrolytes. Finally, the inkjet-printed electrode/electrolyte assembly was sealed with a polypropylene-based adhesive film (thickness ~ 100 μm, Formtec) as a packaging substance.

4.1.2.6. Structural/Rheological/Physical/Electrochemical Characterization of Inkjet-Printed, Solid-State Flexible SCs

The dispersion state of the CNF suspension was examined via transmission electron microscopy (TEM-2010, JEOL) analysis. The ink viscosities of the printed SC components were measured using a rheometer (Haake MARS 3, Thermo Electron GmbH). The surface and cross-sectional morphologies of the printed SC components were investigated by field emission scanning electron microscopy (S-4800, Hitachi) equipped with energy dispersive X-ray spectroscopy (EDS). To further elucidate the structural uniqueness of the CNF-paper, its surface morphology was characterized by 3D laser scanning microscopy (VK-X100, KEYENCE). The water contact angle of the CNF-paper was measured using a drop shape analyzer (DSA100, KRUSS). The electrical resistances of the printed electrodes were measured using a 4-point probe (CMT-SR1000N, Advanced Instrument Technology). The mechanical flexibility of the inkjet-printed electrodes was quantitatively measured using a universal tensile tester (DA-01, Petrol LAB). The thermal stability of the inkjet-printed solid-state electrolytes was examined using thermogravimetric analysis (TGA) measurement (SDT Q600, TA Instruments) at a heating rate of 10 °C min^{-1} under nitrogen atmosphere. The ionic conductivity of the inkjet-printed solid-state electrolytes was characterized by the AC impedance over the frequency range from 10^{-3} to 10^6 Hz. The cell performance of the inkjet-printed SCs was measured using a potentiostat/galvanostat (VSP classic, Bio-Logic) at various charge/discharge conditions.

4.1.3. Results and Discussion

4.1.3.1. CNF Nanomat-Based Primer Layer on A4 Paper for High-Resolution Inkjet Printing

The inkjet-printed, solid-state flexible SCs were fabricated directly on A4 paper using a commercial desktop inkjet printer (HP Deskjet 1010). A schematic illustration depicting the architectural uniqueness of the inkjet-printed SCs is presented in Figure 34a. The cell components were consecutively inkjet-printed on top of the A4 paper in a layered configuration. In printed electronics, the substrate structure and properties along with the ink chemistry/formulation are known to play crucial roles in achieving high-precision print images[41-45]. For example, inkjet printing on so-called "wetting substrates" (upper left side of Figure 34b), such as conventional A4 paper or textiles tends to cause random spreading of the ink droplets due to the uncontrollable capillary force generated from the nonuniformly distributed/several hundred micrometer-sized pores of the substrates[41,45]. Meanwhile, using "non-wetting substrates" (lower left side of Figure 34b), such as non-porous polyethylene terephthalate (PET) films, often leads to a ring-like deposition (i.e., coffee-ring formation) of ink particles[41] as well as poor adhesion[46] of the printed products with the substrates. Thus, these substrate-triggered printing failures demand stringent requirements for ink chemistry and formulation. However, such ink optimization requires tremendous research efforts and often limits a wide selection of ink components, thus posing a formidable obstacle to application extension. In this study, we introduced CNF nanomats (right side of Figure 34b) as a type of primer layer on top of A4 paper through the inkjet printing process to overcome the aforementioned substrate issues. The CNF primer layers were designed to exhibit a well-developed nanoporous structure and uniform surface roughness. As a consequence, the CNF primer layer can provide the combined advantageous attributes of "wetting" and "non-wetting" substrates, eventually broadening the chemistry/formulation horizons of electrode/electrolyte inks and also realizing high-resolution print images on conventional paper without suffering from the droplet spreading or coffee-ring formation.
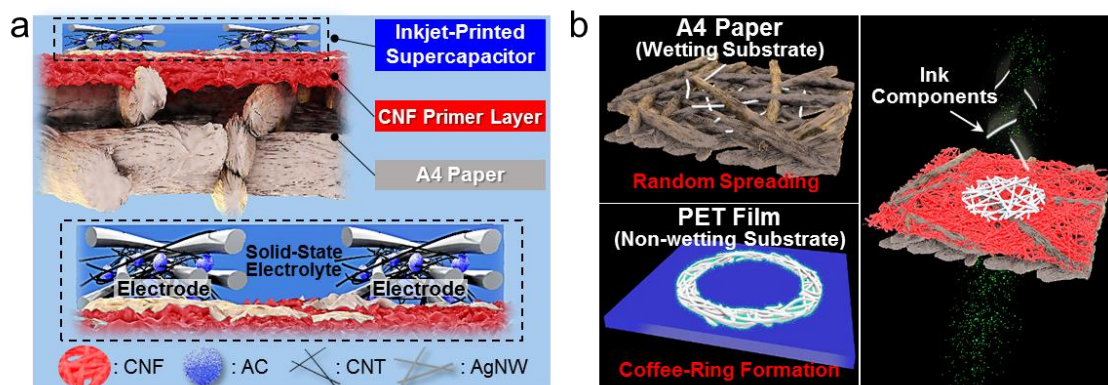
Figure 34. (a) Schematic illustration depicting the architectural uniqueness of the inkjet-printed SCs, wherein the cell components were consecutively inkjet-printed in a layered configuration. (b) Effect of substrates on the resolution of the inkjet printing process: wetting substrate (left upper side, random spreading of ink droplets), non-wetting substrate (left lower side, coffee-ring formation), and CNF nanomat on A4 paper (right side, high-resolution print pattern).

When fabricating the CNF primer layer via inkjet printing, the dispersion state and rheological properties of the CNF suspension should be carefully tuned. The CNFs, which are characterized with nanoscale diameter and length of up to a few micrometers, were produced from the repeated high-pressure homogenization of wood cellulose powders[38,39]. After being subjected to ultrasonication, the CNFs were uniformly dispersed in water (inset images of Fig. 1c). The apparent viscosity (η, measured at a shear rate of 1 s^{-1}) of the CNF suspension was measured as a function of the CNF concentration (Figure 35). The apparent viscosity of the CNF suspension tends to increase with CNF content. At a CNF concentration of 0.3 mg mL^{-1}, the viscosity of the suspension was ~ 18 cP. A further increase in the CNF content to 0.7 mg mL^{-1} led to an abrupt increase in viscosity by an order of magnitude. The desired viscosity values for ink jetting are known be in the range of 5 - 25 cP (marked by dotted lines in Figure 35)[24]. Of the various CNF suspension solutions examined herein, the CNF concentration of 0.3 mg mL^{-1} fulfilled the aforementioned viscosity requirement, thereby allowing for a reliable flow through microsized (= 20 μm) nozzles of inkjet heads without the problems of leaking, skipping, and clogging. Moreover, the CNF suspension ink was stably stored under ambient conditions for longer than one month.
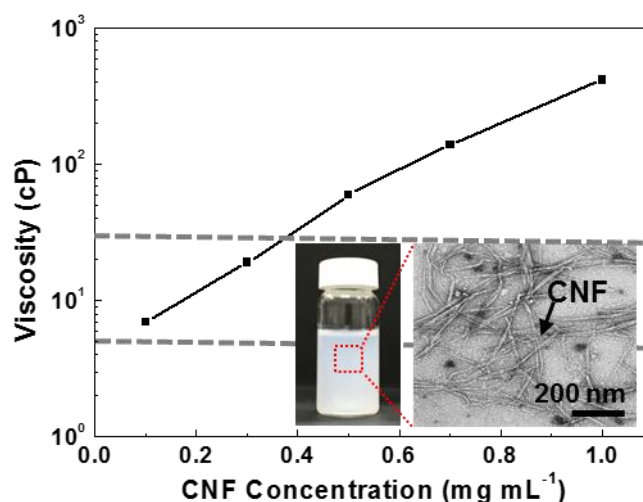
Figure 35. Apparent viscosity (η, measured at a shear rate of 1 s^{-1}) of the CNF suspension solution as a function of CNF concentration, where the insets are a photograph and TEM image of the CNF suspension solution.

The CNF nanomat must have a well-defined porous structure to effectively act as a primer layer on A4 paper in terms of facilitating the drying of inkjet droplets and also the physical anchoring of the ink components. However, the CNFs themselves tend to be densely packed by hydrogen bonding-induced capillary action during water evaporation[47,48] (inset of Fig. 1d). We propose a new concept of solvent exchange reaction based on multiple inkjet printing as an attempt to resolve this problem (Figure 36). A solvent mixture of ethanol/acetone (= 1/1 (v/v)) was subsequently applied on top of the inkjet-printed (wet-state) CNF layer via inkjet printing. As a result, the solvent exchange reaction between the ethanol/acetone mixture and water[39,49] occurred in the wet CNF layer, yielding a CNF nanomat with a highly developed nanoporous structure. In particular, a number of nanometer-sized pores formed between closely packed CNFs were generated over the large area of the CNF primer layer (Figure 36). Moreover, the CNF primer layer contributed to the lower surface roughness (R_a ~ 0.4 μm, Figure 37a) compared to that of the A4 paper (R_a ~ 4.8 μm, Figure 37b), even appearing similar to that (R_a ~ 0.2 μm, Figure 37c) of a commercial PET film. The smooth/homogeneous surface of the CNF primer layer, in conjunction with its well-developed nanoporous structure, is expected to enable the realization of high-resolution print patterns far beyond those that can be achieved with conventional wetting (or non-wetting) substrates.
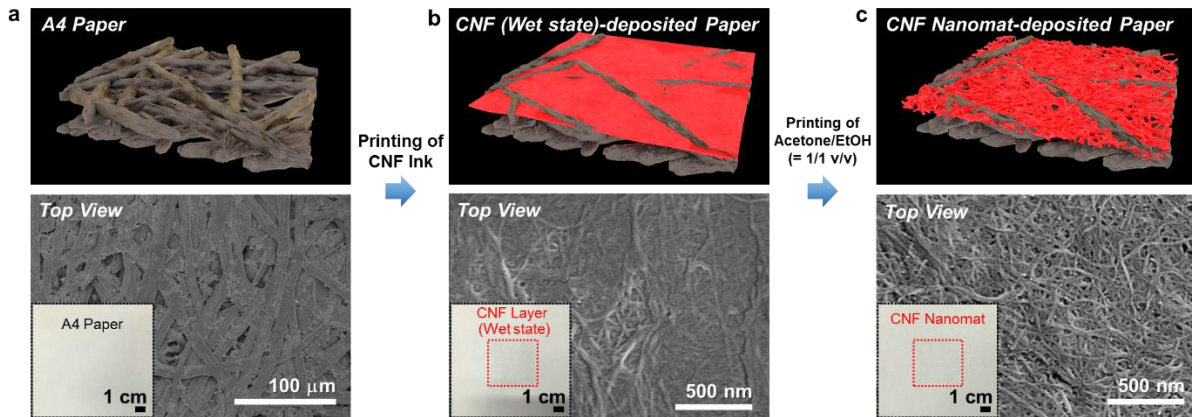
Figure 36. Schematics and SEM images of the stepwise fabrication procedure of the CNF nanomat-based primer layer: (a) A4 paper, (b) inkjet-printed (wet-state) CNF layer deposited on A4 paper, (c) inkjet-printed CNF nanomat deposited onto A4 paper. The highly developed nanoporous structure was generated after the solvent exchange between ethanol/acetone mixture and water.
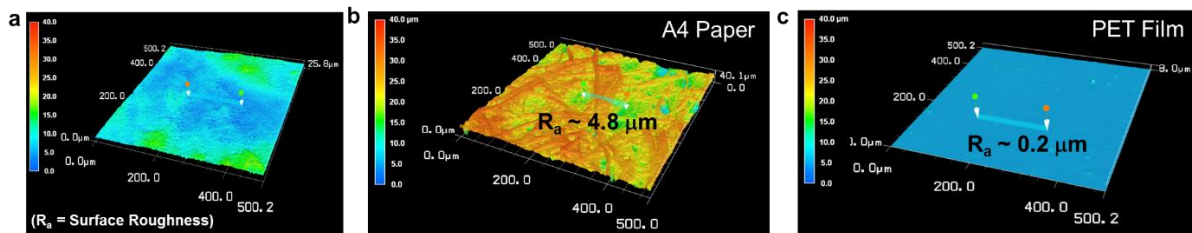

Figure 37. 3D laser scanning microscope images of: (a) CNF nanomat-based primer layer (R_a (surface roughness) ~ 0.4 μm); (b) A4 paper (wetting substrate, R_a (surface roughness) ~ 4.8 μm); (c) PET film (non-wetting substrate, R_a ~ 0.2 μm).

The advantageous functions of the CNF primer layer compared to the control substrates, such as A4 paper and PET film, were elucidated in detail. Figure 38a shows the variation in the water contact angles of the substrates with time. For the A4 paper, the contact angle declined to zero in a short period of time (~ 15 s), which could cause spreading-induced printing failure[41,45]. Meanwhile, for the PET film, the contact angle decreased slowly with time and reached zero after 1,200 s (i.e., extremely slow drying of water), resulting in the coffee-ring formation[41]. In contrast, the CNF nanomat exhibited a moderate decrease in the contact angle with time. To demonstrate the beneficial effects of the CNF primer layer, the electrode ((SWNT/AC) + Ag NW) inks, which will be further described in the following section, were inkjet-printed onto the different substrates. The CNF primer layer allowed the electrode components to be uniformly printed in a precisely defined pattern compared to the control substrates, which showed undesirable printing failures (Figure 38b). Moreover, the electrode components were deposited preferentially onto the surface of the CNF primer-treated A4 paper (referred to as CNF-paper below) substrate (Figure 38c), contributing to their

75

densification and interconnection. As a consequence, the CNF-paper substrate allowed for a substantial decrease in electric resistance (~ 8 ohm sq^{-1}, Figure 38d), which was several orders of magnitude lower than the values obtained with the A4 paper (~ 75 kohm sq^{-1}) and PET substrate (~ 2.2 kohm sq^{-1}).
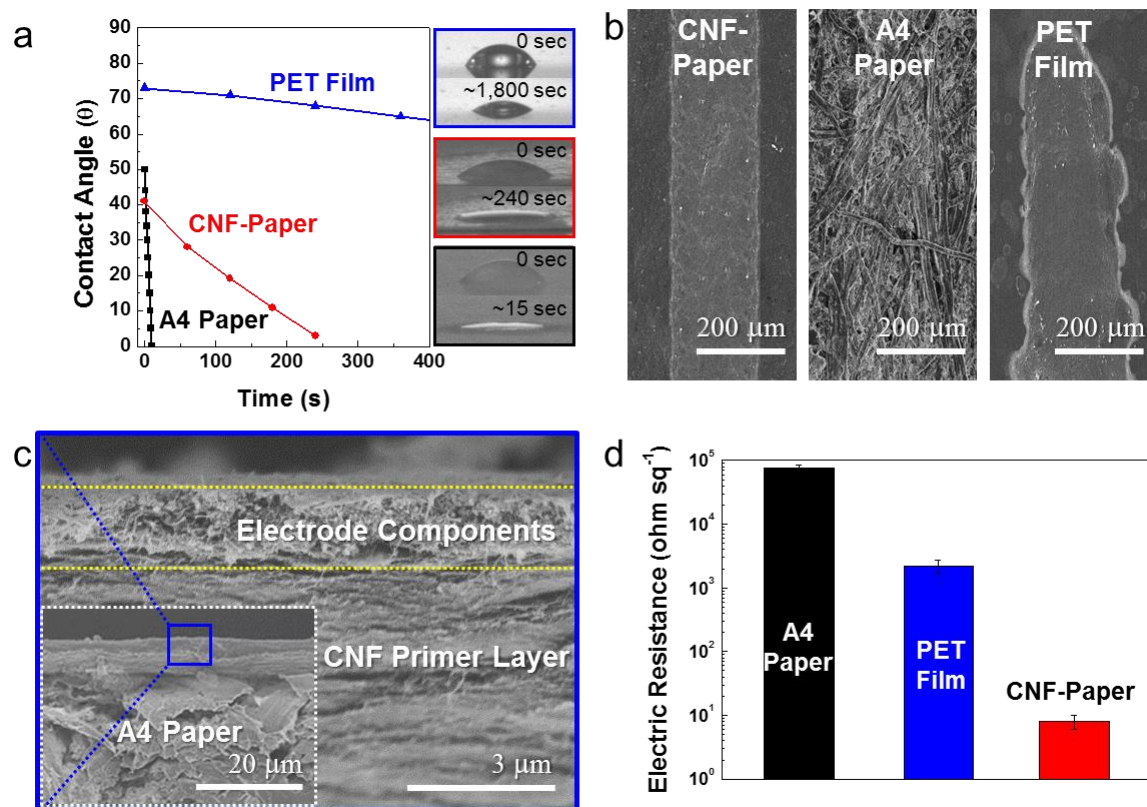

Figure 38. (a) Variation in the water contact angles of different substrates with time. (b) SEM images (surface view) of the inkjet-printed ((SWNT/AC) + Ag NWs) electrodes on different substrates. (c) SEM image (cross-sectional view) showing the preferential deposition of the ((SWNT/AC) + Ag NWs) electrode onto the CNF-paper surface. (d) Electric resistances of the inkjet-printed ((SWNT/AC) + Ag NWs) electrodes on different substrates.

4.1.3.2. Inkjet-Printed Electrodes

In addition to the CNF primer layer mentioned above, electrode and electrolyte inks, which should also be readily inkjet-printed without coagulation in ink cartridges[50], were prepared. The acquisition of electrochemical activity without conventional metallic current collector foils is an important requirement of inkjet-printed electrodes because the metallic foils are known to limit the design diversity of power sources[8-12,16-18]. The electrode inks presented herein were composed of an electrochemically active ink (SWNT/AC in water) and an electrically conductive ink (Ag NWs in water/isopropyl alcohol (IPA) = 1/1 (v/v)). The SWNT/AC inks were subjected to centrifugation (at 10,000 rpm for 1 h) to remove large-sized

particles and agglomerates, resulting in the significant decrease in viscosity (~ 20 cP at a shear rate of 1 s^{-1}) that is suitable for the inkjet printing process. Meanwhile, the Ag NWs were subjected to the sonication-driven scission process to avoid the issue of clogging induced by long Ag NWs with a high aspect ratio[40], thereupon shortening their length from ~ 20 μm to ~ 1 μm. The viscosity of the resultant Ag NW inks containing the short length was ~ 18 cP (at a shear rate of 1 s^{-1}). The SWNT/AC inks were inkjet-printed on top of the CNF-paper substrate, followed by the inkjet printing of the Ag NW inks. The fabrication procedure of the inkjet-printed SC electrodes, along with photographs of the SWNT/AC and Ag NW inks, is conceptually illustrated in Figure 39a. The well-designed electrode and conductive inks, in combination with the CNF primer layer, enabled the facile fabrication of inkjet-printed, letter ("UNIST")-shaped electrodes of different sizes (ranging from centimeter to micrometer scale) on A4 paper (Figure 39b), which appeared as typical inkjet-printed black letters found in office documents.
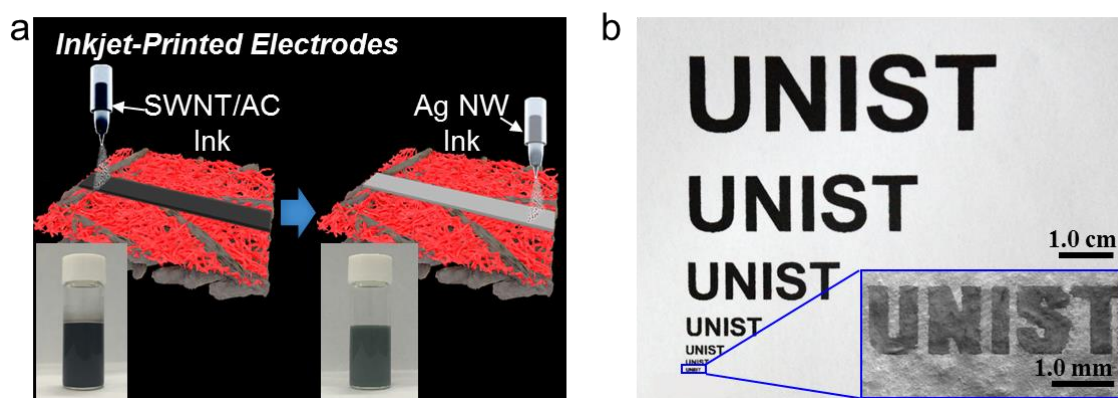

Figure 39. (a) Schematic illustration of the fabrication procedure of the inkjet-printed SC electrodes. The insets are the photographs of an electrochemically active ink (SWNT/AC in water) and an electrically conductive ink (Ag NWs in water/IPA = 1/1 (v/v)). (b) Photograph of the inkjet-printed, letter ("UNIST")-shaped electrodes of different sizes (ranging from centimeter to micrometer scale) on A4 paper.

To further improve the electrical conductivity of the inkjet-printed electrodes, we propose the use of CNT-assisted photonic sintering of Ag NWs, in which the SWNTs are exploited as UV light absorbers and heat-transfer pathways (Figure 40a). Photonic sintering[51], one of the indirect sintering methods, is known to exploit light as a sintering-triggering energy source and can thus complete the sintering reaction in a short period of time compared to traditional direct sintering approaches, such as thermal or mechanical ones. The SWNT networks in the inkjet-printed electrodes promoted the transfer of absorbed UV light energy to the adjacent Ag NWs, thus enhancing the sintering of Ag NWs. As a consequence, a number of Ag NWs were highly interwelded without structural disruption (Figure 40b), leading to the

formation of highly-percolated Ag NWs. This morphological change was verified by examining the change in electrode sheet resistance as a function of UV irradiation time (Figure 40c). The sheet resistance of the control electrode (incorporating ACs/Ag NWs without SWNTs) was slightly decreased and reached a nearly saturated value (~ 100 ohm sq^{-1}) after 150 s. By comparison, the electrode with SWNTs/ACs and Ag NWs showed a drastic decrease in the sheet resistance (~ 8 ohm sq^{-1}). The Raman spectra (with particular attention to the D and G bands[52], Figure 40d) exhibited a slight shifting of the characteristic peaks ascribed to the G band from 1582 to 1590 cm^{-1}, whereas no significant change in the peaks of the D band was observed. This result is consistent with the previously reported results on the CNT-mediated direct growth of Ag NWs[53], demonstrating the interwelding between the SWNTs and Ag NWs in the inkjet-printed SC electrodes. The CNT-assisted photonic sintering can likely be further extended to a variety of printed electronics as well as inkjet-printed power sources due to the simplicity and effectiveness of the process.
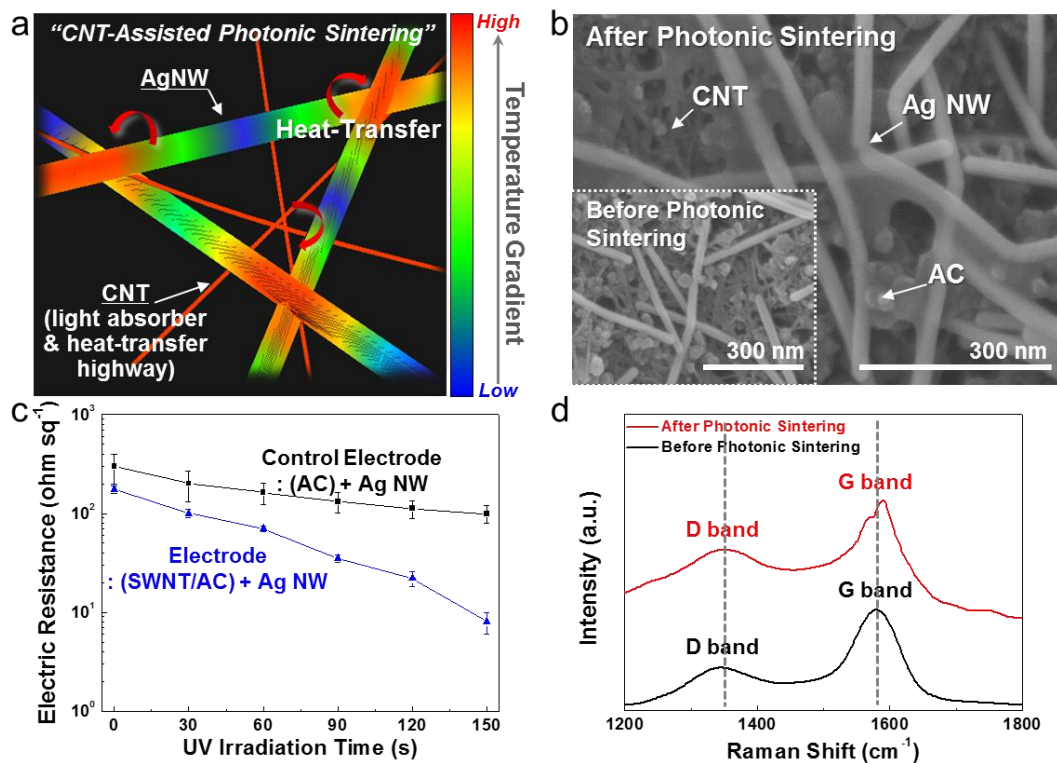

Figure 40. (a) Schematic illustration depicting the CNT-assisted photonic sintering (i.e., interwelding) of Ag NWs. (b) SEM image of the inkjet-printed electrodes before (see the inset) and after the SWNT-assisted photonic sintering. (c) Electric resistances of the inkjet-printed electrode and control electrode (= AC + Ag NW) as a function of UV irradiation time. (d) Raman spectra of the inkjet-printed electrodes before/after the SWNT-assisted photonic sintering.

The resultant inkjet-printed SC electrodes were successfully realized in terms of dimensional integrity and mechanical flexibility even without conventional polymeric binders, such as polyvinylidene fluoride (PVdF). Neither peel-off nor detachment of the electrode constituents was observed after the tape (using commercial Scotch tape) test and the mechanical rubbing test (Figure 41a). To quantitatively analyze the mechanical flexibility of the electrodes, the variation in the relative electrical resistance (= R (electrical resistance upon bending deformation) / R_0 (electrical resistance before bending deformation)) was measured with different bending radii (= 1.0, 3.0, 5.0 mm) as a function of bending cycles. The electrodes withstood the repeated bending deformation of over 1,000 cycles with a negligible increase in their electrical resistance even in the smallest bending radius of 1.0 mm (Figure 41b). Furthermore, the inkjet-printed electrodes were soaked in various solvents (here, water, ethanol, and acetone), and then, the change in their physical state was monitored over time (Figure 41c). No appreciable deterioration was observed in the appearance or electrical resistance.
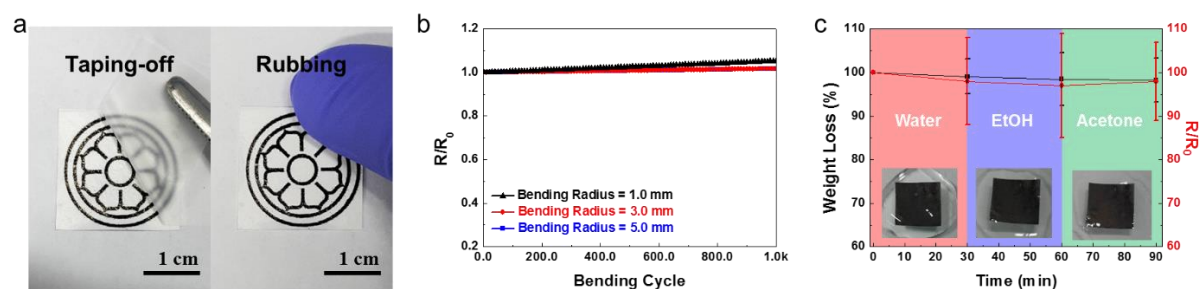

Figure 41. (a) Tape (using commercial Scotch tape) test and mechanical rubbing test of the inkjet-printed electrodes. (b) Variation in the relative electrical resistance (= R (electrical resistance upon bending deformation) / R_0 (electrical resistance before bending deformation)) of the inkjet-printed electrodes as a function of bending cycles with different bending radii (= 1.0, 3.0, and 5.0 mm). (c) Chemical stability of the inkjet-printed electrodes in various solvents (water, ethanol, and acetone).

4.1.3.3. Inkjet-Printed Solid-State Electrolytes

To fabricate inkjet-printed solid-state electrolytes, the ionic liquid ([BMIM][BF$_4$]) was mixed with the ETPTA monomer (incorporating 1.0 wt % 2-hydroxy-2-methyl-1-phenyl-1-propanone (HMPP) as a photoinitiator) in solvents, wherein the composition ratio of the [BMIM][BF$_4$]/ETPTA was 85/15 (w/w). The [BMIM][BF$_4$]/ETPTA mixture was inkjet-printed and then subjected to drying at 80 °C for 60 min in order to remove the residual solvents. Subsequently, the mixture was exposed to UV irradiation, resulting in the crosslinked solid-state gel polymer electrolyte. The UV-crosslinking reaction of the ETPTA monomer was verified by analyzing the changes in the characteristic FT-IR peaks assigned to the C=C double bonds of the ETPTA[13,14] (Figure 42a). Also, the electrochemical stability of the inkjet-printed [BMIM][BF$_4$]/ETPTA electrolyte (after the elimination of the residual water)

was examined using linear scanning voltammetry (LSV) technique. No appreciable electrochemical decomposition was observed between -3.0 to 2.0 V (vs. Pt/Pt⁺) (Figure 42b).
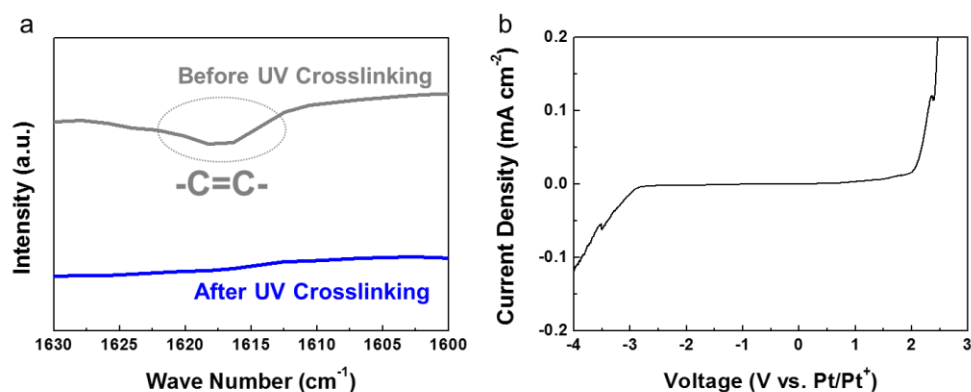

Figure 42. (a) FT-IR spectra showing the change of characteristic peaks assigned to C=C double bonds of ETPTA, before/after the UV crosslinking reaction. (b) Linear sweep voltammetry (LSV) profile of [BMIM][BF$_4$]/ETPTA mixture (after removal of the residual water).

The wetting behavior of the electrolyte inks (i.e., [BMIM][BF$_4$]/ETPTA mixture in solvents) was controlled to ensure inkjet printability, with a particular focus on the solvent effect. Two different solvents (here, water and ethanol) in surface tension were chosen, and both of the resultant electrolyte inks (concentration of [BMIM][BF$_4$]/ETPTA = 10 wt%) showed similar viscosities (~ 13 cP, Figure 43a). For ethanol solvent, the electrolyte ink yielded a blurred image on the CNF-paper substrate due to its low surface tension (= 22.39 mN m^{-1})[54] (upper side, Figure 43b). The randomly scattered red dots (representing the F elements of [BMIM][BF$_4$]) in the energy dispersive X-ray spectroscopy (EDS) images revealed the poorly developed ionic pathways. By comparison, water (surface tension = 72 mN m^{-1})[54] enabled the formation of inkjet-printed electrolytes with a relatively higher resolution, thus constructing the well-interconnected ionic pathways (lower side, Figure 43b). This morphological difference between the two solvents was confirmed by analyzing the Nyquist plots (Figure 43c). The ionic resistance (~ 2.5 ohm) of the water-based printed electrolyte was significantly lower than that (~ 22.0 ohm) of the ethanol-based counterpart. Moreover, the inkjet-printed electrolyte showed no appreciable weight loss with temperature (below 5 wt% up to ~ 320 °C) in the thermogravimetric analysis (TGA) profile due to the presence of the thermally stable ionic liquid (Figure 43d).
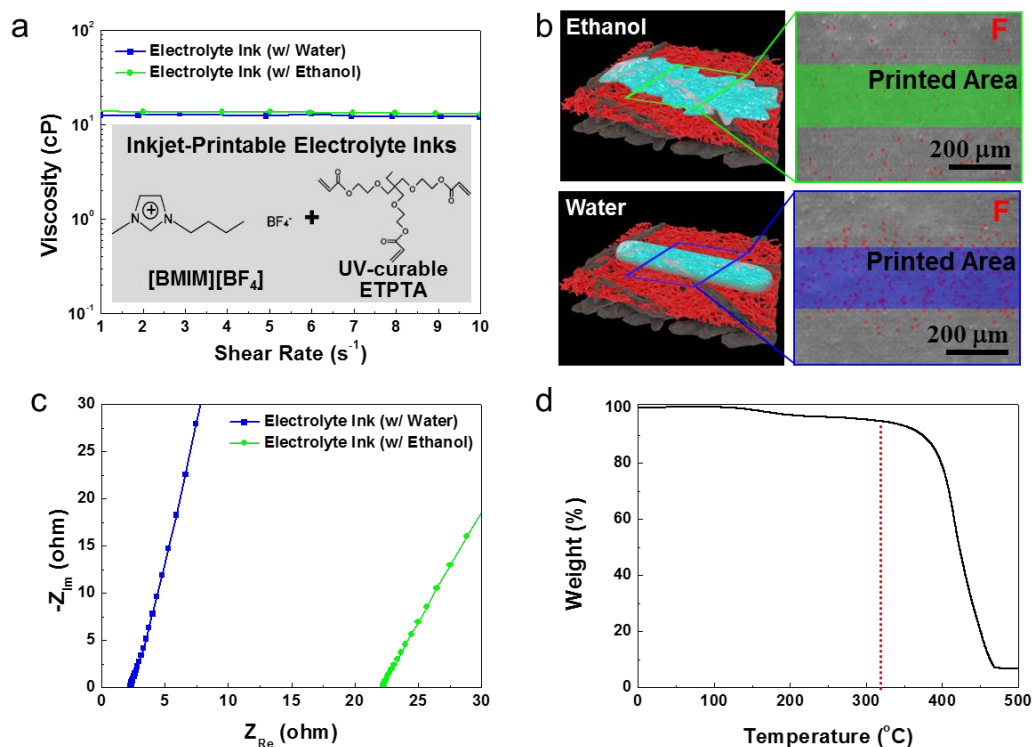
Figure 43. (a) Viscosity of the electrolyte ink ([BMIM][BF$_4$]/ETPTA = 85/15 (w/w) mixture in solvents, concentration = 10 wt%) as a function of shear rate. (b) Schematics and EDS images (red dots represent F elements of [BMIM][BF$_4$]) of the inkjet-printed solid-state electrolytes (ethanol (upper side) vs. water (lower side)). (c) Nyquist plots of the inkjet-printed solid-state electrolytes (ethanol vs. water). (d) TGA profile (dynamic mode, heating rate = 10 ^{o}C min^{-1} under nitrogen atmosphere) of the inkjet-printed ([BMIM][BF$_4$]/ETPTA) solid-state electrolyte.

4.1.3.4. Fabrication and Characterization of Inkjet-Printed SCs with Various Form Factors

Based on the understanding of the structural uniqueness and physicochemical properties of the inkjet-printed electrodes/electrolytes mentioned above, the inkjet-printed SCs featuring high-resolution computer-designed digital images were fabricated directly on A4 paper. The stepwise fabrication procedure, along with a photograph of the desktop inkjet printer used herein, is schematically illustrated in Figure 44a. Here, the electrodes were inkjet-printed "in parallel" instead of the traditional "in-series" configuration to avoid possible internal short-circuit failures between electrodes. The electrodes (SWNTs/ACs with the interwelded Ag NWs) showing comb-shaped patterns were fabricated on the CNF-paper substrate. The [BMIM][BF$_4$]/ETPTA mixture was inkjet-printed on top of the electrodes and then dried at 80 ^{o}C for 60 min in order to remove the residual water. Consecutively, the mixture was subjected to the UV-curing reaction, leading to the crosslinked solid-state gel

polymer electrolyte. Finally, the inkjet-printed electrode/electrolyte assembly was sealed with a polypropylene-based adhesive film.
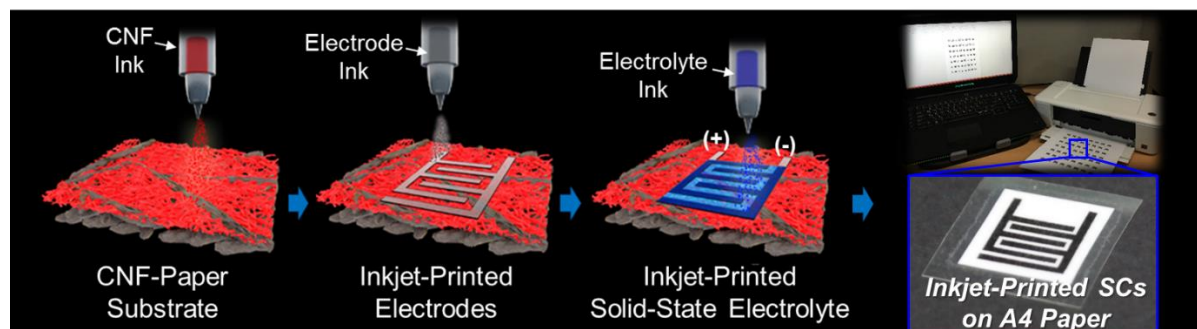

Figure 44. Schematic illustration of the stepwise fabrication procedure of the inkjet-printed SCs, and a photograph of the desktop inkjet printer used herein.

Figure 45a shows the photographs of two SCs with different dimensions, underscoring the fact that the dimensions (width and length) of inkjet-printed SCs can be tuned (ranging from centimeter (upper image) to micrometer scale (lower image)), similar to typical inkjet-printed images. In addition, their cyclic voltammetry (CV) profiles appeared nearly rectangular[21-23] in shape (Figure 45a). The cycling performance of the SC was examined at a constant charge/discharge current density of 0.2 mA cm^{-2} (Figure 45b). No significant decrease in the cell capacitance ($\sim$ 100 mF cm^{-2}) was observed for over 10,000 charge/discharge cycles. The inkjet-printed SCs were subjected to repeated bending deformation (bending radius = 2.5 mm, the deformed state of the SC is displayed in the inset of Figure 45c). Even after 1,000 bending cycles, the SCs still retained their structural integrity without impairing the cell capacitance (Figure 45c); this result is consistent with the previous results (Figure 41a,b) of the inkjet-printed electrodes.
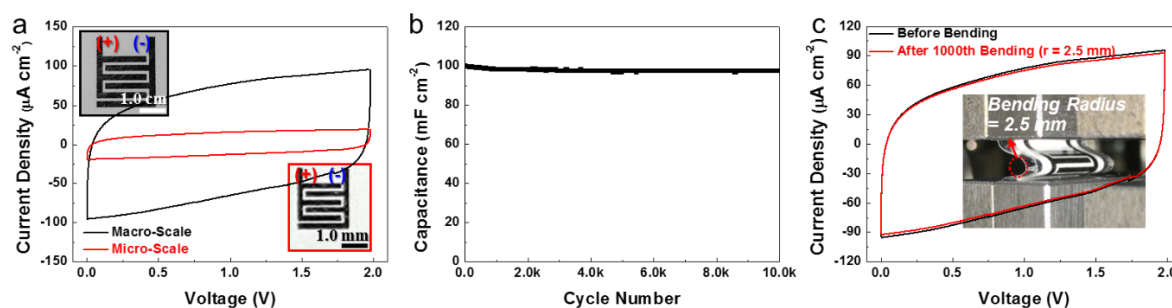

Figure 45. (a) CV profiles (scan rate = 1.0 mV s^{-1}) of the inkjet-printed SCs with different dimensions (insets are their photographs). (b) Cycling performance of the inkjet-printed SC at a constant charge/discharge current density of 0.2 mA cm^{-2}. (c) CV profiles (scan rate = 1.0 mV s^{-1}) of the inkjet-printed SC after the repeated bending deformation (bending radius = 2.5 mm and 1,000 cycles). The inset shows the deformed state of the SC.

One of the most appealing advantages of the inkjet-printed SCs is the provision of aesthetic versatility. The inkjet-printed SCs can be readily connected in series or parallel without the use of metallic interconnects (Figure 46). For example, compared to the mono cell (~ 2 V and ~ 100 mF), the 5 cells connected in series showed a 5-fold increase in voltage (~ 10 V) and the 5 cells connected in parallel presented a 5-fold increase in cell capacitance (~ 500 mF). This result demonstrates that the inkjet printing technology proposed herein allows the voltage and current of the resultant power sources to be easily controlled by simply designing the print patterns.
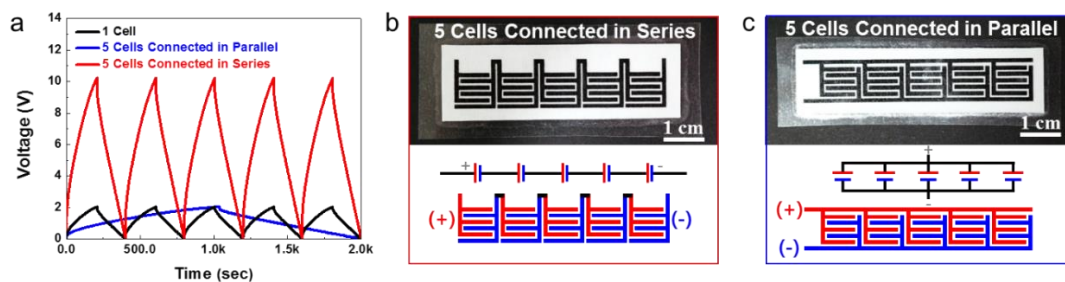

Figure 46. (a) Galvanostatic charge/discharge profiles (current density = 0.2 mA cm^{-2}) of the inkjet-printed SCs connected in series or parallel without the use of metallic interconnects. Schematics and photographs of the inkjet-printed SCs: (b) 5 cells connected in series and (c) 5 cells connected in parallel.

In addition to the facile control of the series/parallel connection of the cells, SCs with various form factors were fabricated through the inkjet printing process. The letter-shaped SC (marked by a red box) was inkjet-printed and then seamlessly connected with the inkjet-printed electrical circuit, eventually powering a LED lamp (Figure 48). In addition, the traditional Korean "Taegeuk" symbol-like SC (marked by a red circle) was inkjet-printed and aesthetically unitized with the inkjet-printed electric circuit, other print patterns, and a LED lamp (Figure 49). Both the letter- and symbol-shaped SCs delivered normal charge/discharge behavior (Supplementary Fig. S14b, S15b). Notably, upon being placed on a hot plate (set at 150 °C) for 0.5 h, the inkjet-printed SC still powered the LED lamp without any volumetric swelling (Figure 49) due to the high thermal stability of the solid-state electrolyte (Figure 43d).
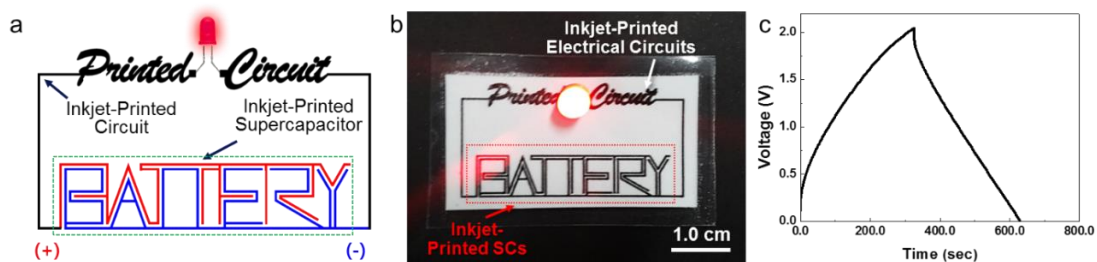

Figure 47. (a) Schematic and (b) photograph of the inkjet-printed, letter ("BATTERY")-shaped SC that was seamlessly connected with the inkjet-printed electrical circuit. (b) Charge/discharge profiles of the inkjet-printed, letter ("BATTERY")-shaped SC.
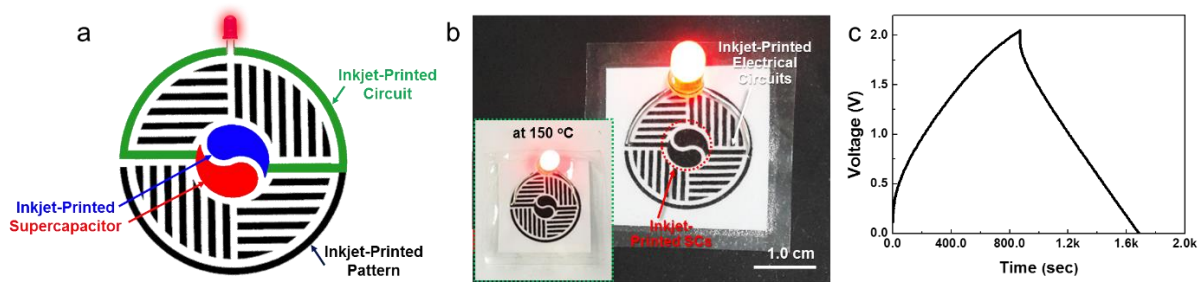
Figure 48. (a) Schematic and (b) photograph of the inkjet-printed, traditional Korean "Taegeuk" symbol-like SC (marked by a red circle) that was seamlessly connected with the inkjet-printed electrical circuits and a LED lamp. The inset is a photograph of the SC after being placed on a hot plate (set at 150 °C) for 0.5 h. (c) Charge/discharge profiles of the inkjet-printed, "Taegeuk" symbol-like SC.

4.1.3.5. Aesthetic Versatillity and IoT Applications of Inkjet-Printed SCs

To further explore the practical potential of the inkjet-printed SCs with a particular focus on IoT applications, we fabricated SCs-unitized digital print images/smart glass cups. A map of Korea was inkjet-printed onto A4 paper (Figure 49a). Subsequently, the SCs (marked by red boxes) were inkjet-printed on top of the dark spots, appearing as one part of the map image (i.e., the presence of the SCs was difficult to detect). The SCs were then seamlessly connected via the inkjet-printed electric circuits to LED lamps (marked by blue boxes) (Figure 49b), eventually powering the LED lamps with normal charge/discharge profiles (Figure 49c).
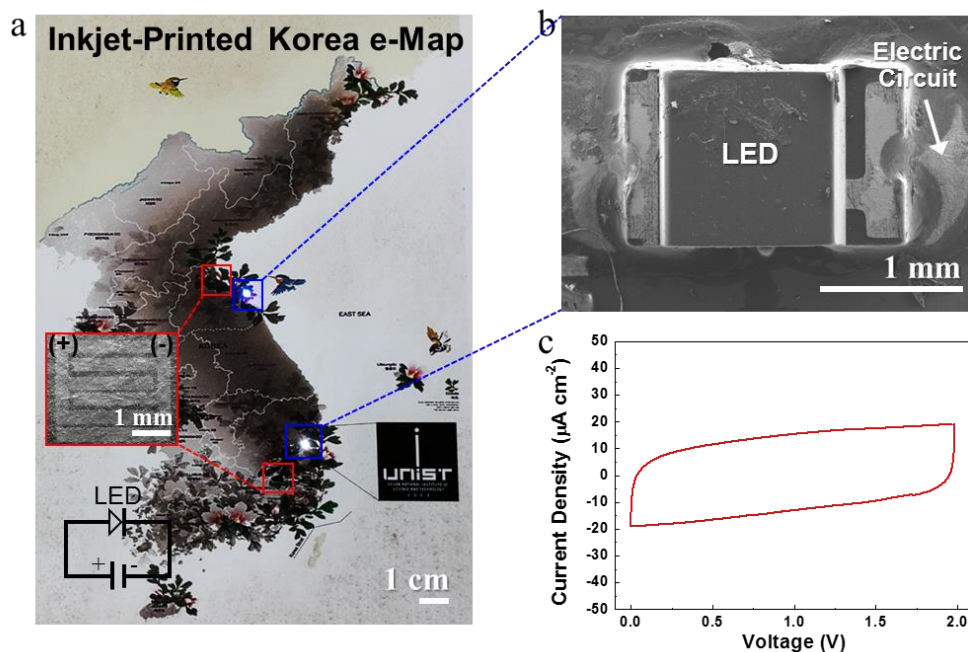

Figure 49. (a) Photograph of the inkjet-printed Korea map, wherein the inkjet-printed SCs (marked by red boxes) were seamlessly connected to LED lamps (marked by blue boxes) via the inkjet-printed electric circuits. (b) SEM image of the LED lamp connected to the inkjet-

printed electric circuits. (c) CV profile (scan rate = 1.0 mV s^{-1}) of the inkjet-printed SC in the map.

To highlight the unique functions of the inkjet-printed SCs as a monolithically-integrated power source for the IoT, we fabricated smart glass cups that can intelligently respond to temperature stimulus. The letter (here, "OR")-shaped SCs were inkjet-printed onto A4 paper and then seamlessly connected to a temperature sensor assembled with an Arduino board and also blue/red LED lamps via the letter ("HOT" and "COLD")-shaped electric circuits (Figure 50a). The inkjet-printed SCs consisted of 4 cells connected in series and exhibited normal charge/discharge behavior (Figure 50b). The Arduino board was coded to power a red LED lamp when the sensor detects a temperature above 60 °C and a blue LED lamp when the sensor detects a temperature below 20 °C. The A4 paper containing the inkjet-printed SCs and the above-mentioned electric components was aesthetically cut and then attached to the glass cup. Finally, the letter-shaped, inkjet-printed SCs ("OR") and electric circuits ("HOT" and "COLD") appeared as a type of decorative image on the smart glass cup. When cold water (~ 10 °C) was poured into the smart cup, the blue LED lamp connected with the "COLD"-shaped electric circuits emitted light (Figure 50c). Alternatively, the red LED lamp connected with the "HOT"-shaped electric circuits started to operate (Figure 50d) upon filling the smart cup with hot water (~ 80 °C). These results underline the exceptional applicability of the inkjet-printed SCs as an object-tailored power source that lies far beyond those that can be achieved with conventional battery technologies.
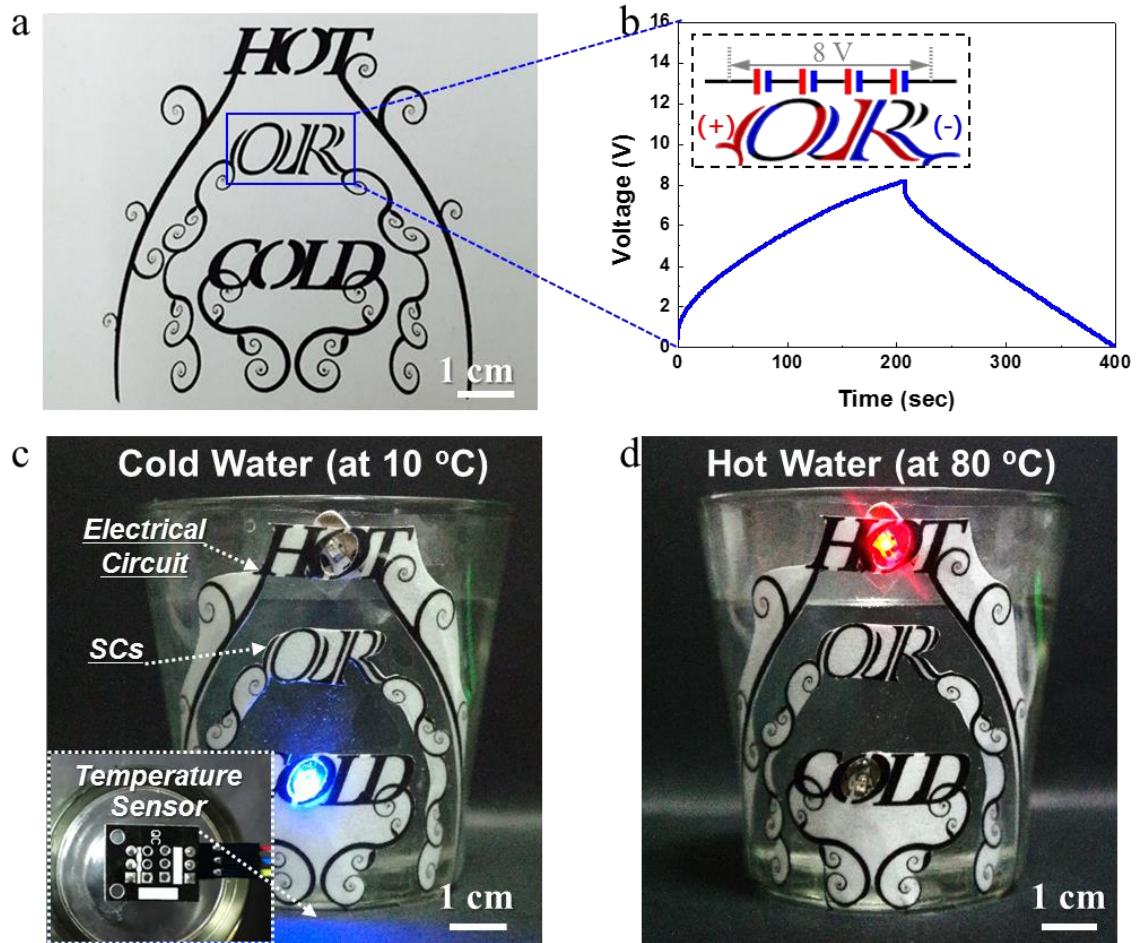
Figure 50. (a) Photograph of the inkjet-printed, letter ("OR")-shaped SCs that were seamlessly connected to the letter ("HOT" and "COLD")-shaped electric circuits onto A4 paper. (b) Galvanostatic charge/discharge profile (current density = 1.0 mA cm^{-2}) of the inkjet-printed, letter ("OR")-shaped SCs that were composed of 4 cells connected in series. (c) Photograph depicting the operation of the blue LED lamp in the smart cup (for cold water (~ 10 °C)), wherein the inset is a photograph of a temperature sensor assembled with an Arduino board. (d) Photograph depicting the operation of the red LED lamp in the smart cup (for hot water (~ 80 °C)).

4.1.4. Conclusion

In summary, we demonstrated the solid-state flexible SCs with unprecedented form factors that were fabricated onto conventional A4 paper using a commercial desktop inkjet printer. The new SCs appeared as typical inkjet-printed letters or patterns commonly found in office documents. To attain high-resolution print images on A4 paper, a CNF-mediated nanomat was inkjet-printed as a primer layer. The introduction of Ag NWs onto the SWNT/AC electrodes, in combination with the SWNT-assisted photonic interwelding of Ag NW networks, led to a substantial improvement in the electrical conductivity of the resultant inkjet-printed electrodes. The ([BMIM][BF$_4$]/ETPTA) solid-state electrolyte was applied to the inkjet-printed electrodes via inkjet printing, after which the UV-crosslinking process was performed. The inkjet-printed SCs exhibited reliable electrochemical performance over 2,000 cycles as well as good mechanical flexibility. The inkjet-printed SCs were easily connected in series or parallel without the aid of metallic interconnects, thereby enabling the user-customized control of the cell voltage and capacitance. More notably, the inkjet-printed SCs featuring the computer-designed artistic patterns and letters were aesthetically unitized with other inkjet-printed art images (e.g., a map of Korea) and smart glass cups, underscoring their exceptionally versatile aesthetics and potential applicability as a new class of object-tailored power sources. Future works will be devoted to extending the application fields of the inkjet-printed power sources to other energy storage systems such as lithium-/sodium-ion and metal-air batteries. Due to the simplicity/scalability of their process and design universality, the inkjet-printed SCs presented herein hold substantial promise as a new class of monolithically-integrated flexible power sources in urgent need for the forthcoming IoT and flexible/wearable electronics.

4.1.5. References

(1) S. Bauer, *Nat. Mater.*, 2013, **12**, 871-872.

(2) Y. Gogotsi, *Nature*, 2014, **509**, 568-570.

(3) S. Xu, Y. Zhang, J. Cho, J. Lee, X. Huang, L. Jia, J. A. Fan, Y. Su, J. Su, H. Zhang, H. Cheng, B. Lu, C. Yu, C. Chuang, T. I. Kim, T. Song, K. Shigeta, S. Kang, C. Dagdeviren, I. Petrov, P. V. Braun, Y. Huang, U. Paik and J. A. Rogers, *Nat. Commun.*, 2013, **4**, 1543.

(4) Y. Z. Zhang, Y. Wang, T. Cheng, W. Y. Lai, H. Pang and W. Huang, *Chem. Soc. Rev.*, 2015, **44**, 5181-5199.

(5) G. Zhou, F. Li and H.-M. Cheng, *Energy Environ. Sci.*, 2014, **7**, 1307-1338.

(6) C. Yan and P. S. Lee, *Small*, 2014, **10**, 3443-3460.

(7) K. Xie and B. Wei, *Adv. Mater.*, 2014, **26**, 3592-3617.

(8) S.-Y. Lee, K.-H. Choi, W.-S. Choi, Y. H. Kwon, H.-R. Jung, H.-C. Shin and J. Y. Kim, *Energy Environ. Sci.*, 2013, **6**, 2414-2423.

(9) X. Lu, M. Yu, G. Wang, Y. Tong and Y. Li, *Energy Environ. Sci.*, 2014, **7**, 2160-2181.

(10) A. M. Gaikwad, A. C. Arias and D. A. Steingart, *Energy Technol.*, 2015, **3**, 305-328.

(11) B. C. Kim, J.-Y. Hong, G. G. Wallace and H. S. Park, *Adv. Energy Mater.*, 2015, **5**, 1500959.

(12) X. Wang, X. Lu, B. Liu, D. Chen, Y. Tong and G. Shen, *Adv. Mater.*, 2014, **26**, 4763-4782.

(13) E. H. Kil, K. H. Choi, H. J. Ha, S. Xu, J. A. Rogers, M. R. Kim, Y. G. Lee, K. M. Kim, K. Y. Cho and S. Y. Lee, *Adv. Mater.*, 2013, **25**, 1395-1400.

(14) S. H. Kim, K. H. Choi, S. J. Cho, S. Choi, S. Park and S. Y. Lee, *Nano Lett.*, 2015, **15**, 5168-5177.

(15) Y. Xu, M. G. Schwab, A. J. Strudwick, I. Hennig, X. Feng, Z. Wu and K. Müllen, *Adv. Energy Mater.*, 2013, **3**, 1035-1040.

(16) L. Hu, H. Wu, F. La Mantia, Y. Yang and Y. Cui, *ACS Nano*, 2010, **4**, 5843-5848.

(17) N. Singh, C. Galande, A. Miranda, A. Mathkar, W. Gao, A. L. Reddy, A. Vlad and P. M. Ajayan, *Sci. Rep.*, 2012, **2**, 481-485.

(18) A. M. Gaikwad, G. L. Whiting, D. A. Steingart and A. C. Arias, *Adv. Mater.*, 2011, **23**, 3251-3255.

(19) K. T. Braam, S. K. Volkman and V. Subramanian, *J. Power Sources*, 2012, **199**, 367-372.

(20) X. Wang, B. Liu, Q. Xiang, Q. Wang, X. Hou, D. Chen and G. Shen, *ChemSusChem*, 2014, **7**, 308-313.

(21) Y. Cheng, L. Huang, X. Xiao, B. Yao, L. Yuan, T. Li, Z. Hu, B. Wang, J. Wan and J. Zhou, *Nano Energy*, 2015, **15**, 66-74.

(22) J. Li, K. Liu, X. Gao, B. Yao, K. Huo, Y. Cheng, X. Cheng, D. Chen, B. Wang, W. Sun, D. Ding, M. Liu and L. Huang, *ACS Appl. Mater. Interfaces*, 2015, **7**, 24622-24628.

(23)Q. P. Luo, L. Huang, X. Gao, Y. Cheng, B. Yao, Z. Hu, J. Wan, X. Xiao and J. Zhou, *Nanotechnology*, 2015, **26**, 304004.

(24)B.-J. D. Gans, P. C. Duineveld and U. S. Schubert, *Adv. Mater.*, 2004, **16**, 204-213.

(25)M. Singh, H. M. Haverinen, P. Dhagat and G. E. Jabbour, *Adv. Mater.*, 2010, **22**, 673-685.

(26)H. Sirringhaus, T. Kawase, R. H. Friend, T. Shimoda, M. Inbasekaran, W. Wu and E. P. Woo, *Science*, 2000, **290**, 2123-2126.

(27)V. Dua, S. P. Surwade, S. Ammu, S. R. Agnihotra, S. Jain, K. E. Roberts, S. Park, R. S. Ruoff and S. K. Manohar, *Angew. Chem. Int. Ed.*, 2010, **49**, 2154-2157.

(28)G. Azzellino, A. Grimoldi, M. Binda, M. Caironi, D. Natali and M. Sampietro, *Adv. Mater.*, 2013, **25**, 6829-6833.

(29)J. Li, F. Ye, S. Vaziri, M. Muhammed, M. C. Lemme and M. Ostling, *Adv. Mater.*, 2013, **25**, 3985-3992.

(30)C. C. Ho, J. W. Evans and P. K. Wright, *J. Micromech. Microeng.*, 2010, **20**, 104009-104017.

(31)W. YongQing, G. YuGuo and W. LiJun, *Chin. Sci. Bull.*, 2013, **58**, 3227-3232.

(32)K. Sun, T. S. Wei, B. Y. Ahn, J. Y. Seo, S. J. Dillon and J. A. Lewis, *Adv. Mater.*, 2013, **25**, 4539-4543.

(33)P. Chen, H. Chen, J. Qiu and C. Zhou, *Nano Res.*, 2010, **3**, 594-603.

(34)Y. Xu, I. Hennig, D. Freyberg, A. James Strudwick, M. Georg Schwab, T. Weitz and K. Chih-Pei Cha, *J. Power Sources*, 2014, **248**, 483-488.

(35)D. Pech, M. Brunet, P.-L. Taberna, P. Simon, N. Fabre, F. Mesnilgrente, V. Conédéra and H. Durou, *J. Power Sources*, 2010, **195**, 1266-1269.

(36)M. H. Ervin, L. T. Le and W. Y. Lee, *Electrochim. Acta*, 2014, **147**, 610-616.

(37)S. Wang, N. Liu, J. Tao, C. Yang, W. Liu, Y. Shi, Y. Wang, J. Su, L. Li and Y. Gao, *J. Mater. Chem. A*, 2015, **3**, 2407-2413.

(38)S.-J. Chun, E.-S. Choi, E.-H. Lee, J. H. Kim, S.-Y. Lee and S.-Y. Lee, *J. Mater. Chem.*, 2012, **22**, 16618.

(39)K. H. Choi, S. J. Cho, S. J. Chun, J. T. Yoo, C. K. Lee, W. Kim, Q. Wu, S. B. Park, D. H. Choi, S. Y. Lee and S. Y. Lee, *Nano Lett.*, 2014, **14**, 5677-5686.

(40)D. J. Finn, M. Lotya and J. N. Coleman, *ACS Appl. Mater. Interfaces*, 2015, **7**, 9254-9261.

(41)M. Kuang, L. Wang and Y. Song, *Adv. Mater.*, 2014, **26**, 6950-6958.

(42)J. Z. Wang, Z. H. Zheng, H. W. Li, W. T. Huck and H. Sirringhaus, *Nat. Mater.*, 2004, **3**, 171-176.

(43)D. Tian, Y. Song and L. Jiang, *Chem. Soc. Rev.*, 2013, **42**, 5184-5209.

(44)K. H. Chu, R. Xiao and E. N. Wang, *Nat. Mater.*, 2010, **9**, 413-417.

(45) J. Lessing, A. C. Glavan, S. B. Walker, C. Keplinger, J. A. Lewis and G. M. Whitesides, *Adv. Mater.*, 2014, **26**, 4677-4682.

(46) L. Hu and Y. Cui, *Energy Environ. Sci.*, 2012, **5**, 6423.

(47) M. M. Hamedi, A. Hajian, A. B. Fall, K. Hakansson, M. Salajkova, F. Lundell, L. Wagberg and L. A. Berglund, *ACS Nano*, 2014, **8**, 2467-2476.

(48) R. J. Moon, A. Martini, J. Nairn, J. Simonsen and J. Youngblood, *Chem. Soc. Rev.*, 2011, **40**, 3941-3994.

(49) H. Sehaqui, Q. Zhou, O. Ikkala and L. A. Berglund, *Biomacromolecules*, 2011, **12**, 3638-3644.

(50) A. Russo, B. Y. Ahn, J. J. Adams, E. B. Duoss, J. T. Bernhard and J. A. Lewis, *Adv. Mater.*, 2011, **23**, 3426-3430.

(51) A. Kamyshny and S. Magdassi, *Small*, 2014, **10**, 3515-3535.

(52) M. S. Dresselhaus, G. Dresselhaus, A. Jorio, A. G. Souza Filho and R. Saito, *Carbon*, 2002, **40**, 2043-2061.

(53) L. Cui, Z. Du, W. Zou, H. Li and C. Zhang, *RSC Adv.*, 2014, **4**, 27591.

(54) N. R. Pallas and Y. Harrison, *Colloids Surf. B*, 1990, **43**, 169-194.

(55) M. F. El-Kady and R. B. Kaner, *Nat. Commun.*, 2013, **4**, 1475.

4.2. Direct-Writable Zn-Air Batteries on Paper towards On-The-Fly Power Sources

4.2.1. Introduction

Printed electronics is of great interest as a scalable platform owing to the prospect of low-cost, ubiquitous integrated systems with arbitrary constructs, such as flexible/wearable electronics and the Internet of things (IoT) devices[1-5]. In the printed electronics, recent attention has been focused on the pen-drawing platform that allows for end users to design and fabricate inexpensive yet reliable self-serviced circuits in biomedical and electrochemical detection devices[6-8]. However, the practical implementation of the pen-drawing platform requires advanced power sources on-the-fly under ambient conditions to fully exploit the potential of the pen-drawing electronics.

The on-the-fly power sources, which can be fabricated "on-demand" and "on-site" under ambient conditions, enable the simple integration with arbitrary constructs, thus facilitating the rapid prototyping of low-cost, ubiquitous integrated systems. Recently, various techniques have been developed to fabricate the on-the-fly power sources, such as spray coating[9-10], screen printing[11-13], inkjet printing[14], and extrusion-based three-dimensional (3D) printing[15-16]. However, these sophisticated techniques limit the emerging demand of low cost, easy accessibility and rapid prototyping for flexible electronics fabrication, due to the long processing period, the high energy consumption, and the inevitable enrollment of expensive professional equipment of printing[6]. These constraints related to fabrication, therefore, present formidable challenges to developing the on-the-fly power sources.

4.2.2. Experimental

4.2.2.1. Direct-Writable Zn Anode Inks

The direct-writable Zn anode ink was prepared by mixing a linseed oil (Aldrich) with Zn nanoparticles (particle size ~ 50 nm, Aldrich) using a Thinky Planetary Centrifugal Mixer (Thinky USA, Inc.), to which wood turpentine oil (Aldrich) was mixed as a thinning agent. The ink was loaded into the pen (Gelly Roll, Sakura, Inc.) using a disposable pipette, where the pen was cleaned prior to use. After pen writing was performed, printed Zn patterns were allowed to UV irradiation (Hg UV-lamp, Lichtzen) for 10 min to result in the polymerization reaction of the linseed oil, where the resulting linseed oil-induced polymers can act as a water-repelling binder.

4.2.2.2. Fabrication of Direct-Writable Zn-Air Batteries

To fabricate the direct-writable Zn-air batteries, current collector patterns were drawn on A4 paper, using a commercial conductive silver pen (Circuit Scribe). On top of one side of the current collector, the Zn anode was drawn and then subjected to the UV irradiation for curing. On top of the other side of the current collector pattern, the air cathode was drawn by using a pencil (8B, Staedtler). Finally, a gel electrolyte, wherein the weight-based composition ratio of PAA/6 M KOH solution was 2.5/97.5 w/w, was overwritten on the electrodes to produce the direct-writable Zn-air batteries.
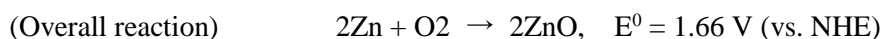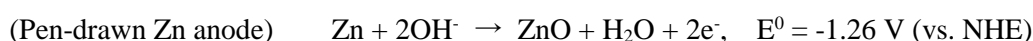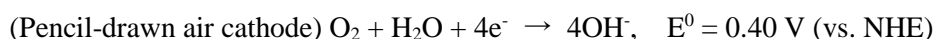
4.2.2.3. Structural/Rheological/Physical/Electrochemical Characterization of Direct-Writable Zn-Air Batteries

The dispersion state of the Zn anode ink was examined via optical microscopy (OLS3100, Olypus) analysis. The rheological properties of the ink were measured using a rheometer (Haake MARS 3, Thermo Electron GmbH). The polymerization reaction of the ink was verified using fluorescence microscope (IX71, Olympus). The variation in the surface morphologies of the Zn anodes under the high-humidity and high-temperature (at 95% RH/80 °C for 10 hr) was investigated by field emission scanning electron microscopy (S-4800, Hitachi). The mechanical flexibility of the direct-writable Zn-air batteries was quantitatively measured using a universal tensile tester (DA-01, Petrol LAB). The cell performance of the direct-writable Zn-air batteries was measured using a potentiostat/galvanostat (VSP classic, Bio-Logic) at various charge/discharge conditions.

4.2.3. Results and Discussion

4.2.3.1. Architecture Design of Writable Zn-Air Batteries

Here, we demonstrate a direct-writable Zn-air battery that can be fabricated by using a simple pen writing technique (Figure 51). The writable Zn-air battery is composed of four parts; pen-drawn current collectors[7], a pen-drawn Zn anode, a pencil-drawn air cathode, which is divided into a percolated graphitic carbon catalytic layer[17] and paper substrate as a gas diffusion layer, and a gel electrolyte. The writable Zn-air batteries were fabricated in 2-series connection directly on A4 paper (Figure 52). On top of the pen-drawn current collectors, the respective electrodes (e.g., pencil-drawn air cathodes and Zn anodes) were drawn. On top of each battery, gel electrolytes were finally drawn to form two batteries in series connection to power a LED lamp mounted directly on the printed electrical circuit. During discharge, the writable Zn-air battery functions as a power generator through the following electrochemical reaction of the Zn anode to the air electrode in an alkaline electrolyte[18-19].

(Pencil-drawn air cathode) $O_2 + H_2O + 4e^- \rightarrow 4OH^-$, $E^0 = 0.40$ V (vs. NHE)

(Pen-drawn Zn anode) $Zn + 2OH^- \rightarrow ZnO + H_2O + 2e^-$, $E^0 = -1.26$ V (vs. NHE)

(Overall reaction) $2Zn + O2 \rightarrow 2ZnO$, $E^0 = 1.66$ V (vs. NHE)

Both half cell reactions are thermodynamically spontaneous and produce a theoretical voltage of 1.66 V[18], enabling the writable Zn-air battery as the on-the-fly power source that does not require the additional charging process.
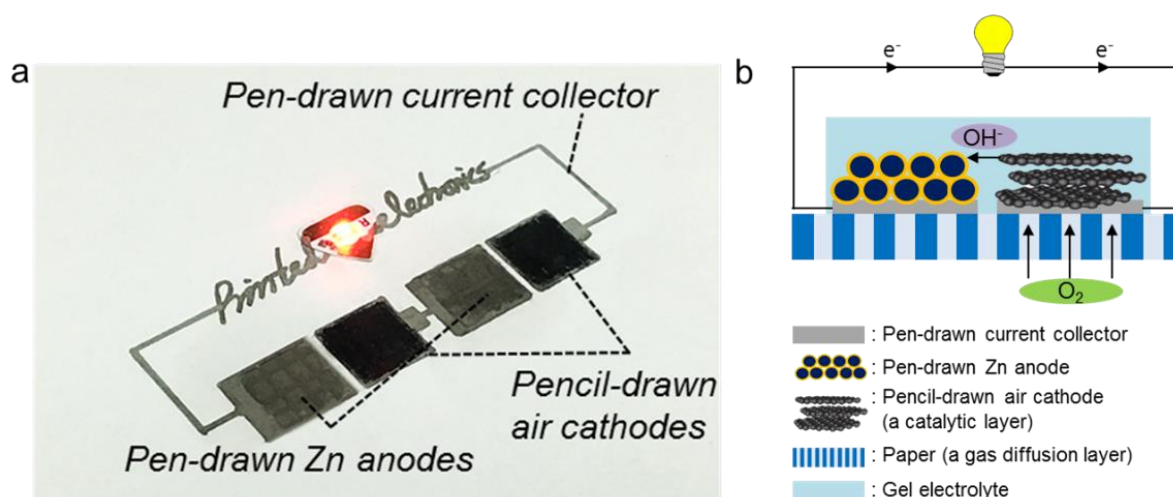

Figure 51. (a) Photograph of writable Zn-air batteries in two series connection to power a LED lamp mounted on the printed circuit, wherein the cell components were consecutively drawn in a layered configuration. (b) Schematic representation depicting the working principle of the writable Zn-air battery.
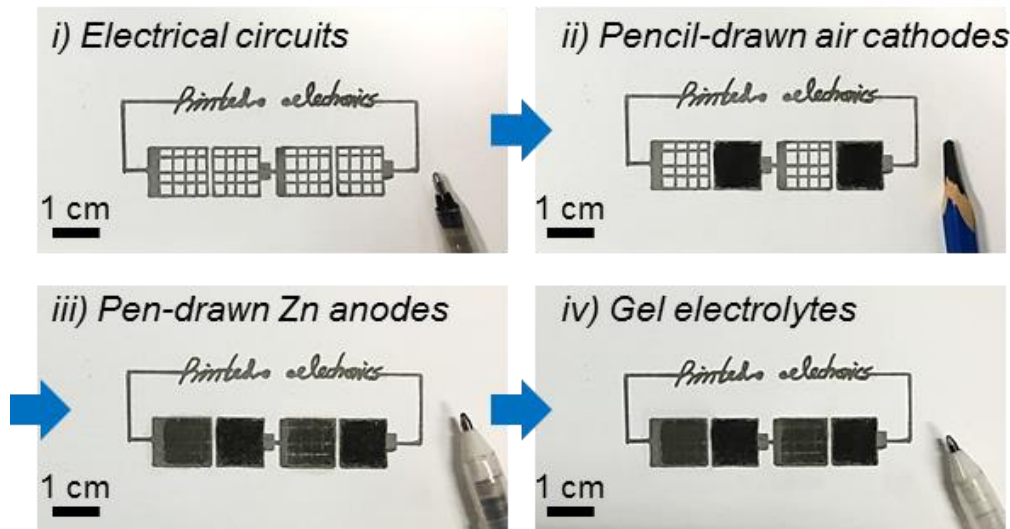
Figure 52. Photographs showing the stepwise fabrication procedure of writable Zn-air batteries in 2-series connection.

4.2.3.2. Oil Painting-Inspired Design of Direct-Writable Zn Anode Inks

Central to the direct-writable Zn-air battery is the design of a Zn anode ink (Figure 53a) that readily flows through the rollerball pen tip during writing, and can be stored without chemical changes or coagulation of colloidal particles within the pen to secure a long shelf life[6-8]. However, Zn metal easily undergoes oxidation reaction at ambient conditions to produce the formation of a ZnO passive layer on the Zn surface[20-22], which presents challenges to formulating stable Zn anode inks. To create the Zn anode ink with ideal attributes, we introduced the oil painting-inspired design concept (Figure 53b), in which a drying oil medium can act as a carrier solvent to stabilize the dispersion of Zn nanoparticles; a functional binder able to protect Zn nanoparticles after the oil was dried. Oil painting is the process of painting pigment particles with a medium of drying oil as a binder, in which the use of drying oil led to the Renaissance era due to its advantages over other painting mediums. Among various painting oils, linseed oil, in particular, is an edible oil as a nutritional supplement; it has a distinctive feature for its exceptionally large amount of α-linolenic acid, which has di- and tri-unsaturated esters to be particularly susceptible to polymerization reactions upon exposure to oxygen in the air[23-24]. The intrinsic water-repelling nature of the resulting hydrocarbon-based polymers can play a viable role in the mechanical and chemical integrity of the Zn anode, which will be further discussed in the following section.
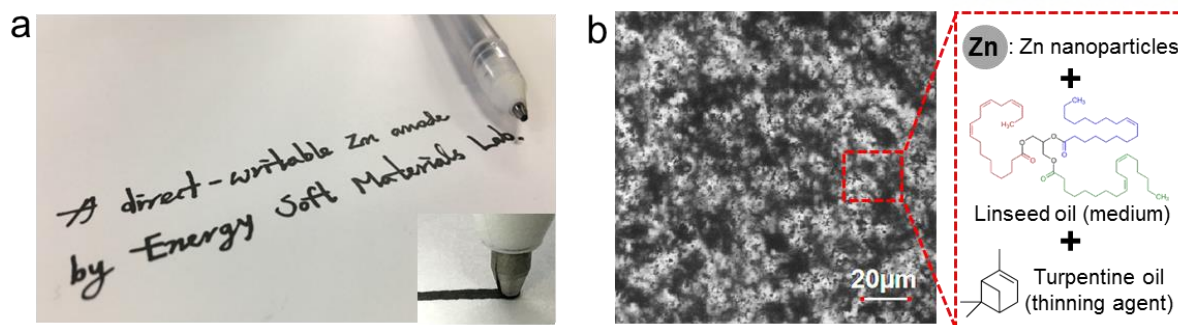
Figure 53. (a) Photograph of a rollerball pen loaded with a Zn anode ink, where the inset shows the rollerball pen tip during writing a Zn anode track. The background shows metallic Zn text directly written on A4 paper. (b) Optical microscope image demonstrating the dispersion state of Zn nanoparticles in the Zn anode ink. The Zn anode ink was composed of Zn nanoparticles, linseed oil as a carrier solvent and functional binder, and turpentine oil as a thinning agent.

Figure 54 shows the apparent viscosity (η) at a shear rate of 1 s^{-1} as a function of Zn solid contents. The apparent viscosity tends to increase with Zn concentration. At a Zn concentration of 60%, the viscosity was ~10 cP. A further increase in the Zn content to 70 wt% resulted in a significant increase in viscosity by an order of magnitude. Of these compositions, those inks with 40-60 wt% of Zn nanoparticles reliably flowed through the pen without leaking, skipping, or clogging. Meanwhile, this high Zn concentration (= 60 wt%) can be achieved by introducing wood turpentine oil as a shear-thinning medium (Figure 55). At the fixed Zn concentration at 60 wt%, the addition of the thinning medium resulted in a decrease in the viscosity, and thus yielding occured at lower shear stress by an order of magnitude. Notably, these inks were stable over a month when stored in a sealed container and can flow through the pen after a month (Figure 56). These results demonstrate the oil painting-inspired design of the Zn anode ink is effective in formulating the writable Zn anode ink with the stable dispersion state.
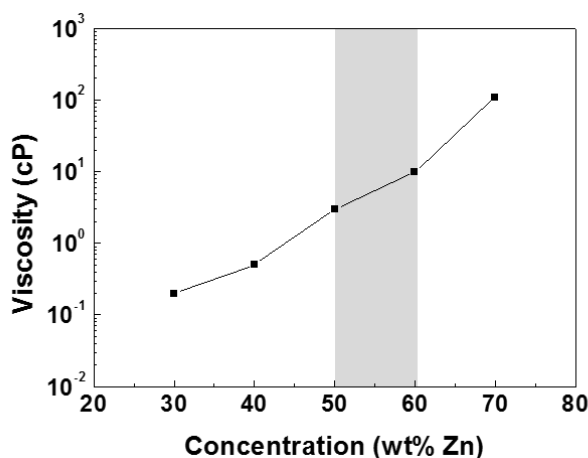

Figure 54. Apparent viscosity (η, measured at a shear rate of 1 s^{-1}) of Zn anode inks as a function of Zn concentration.
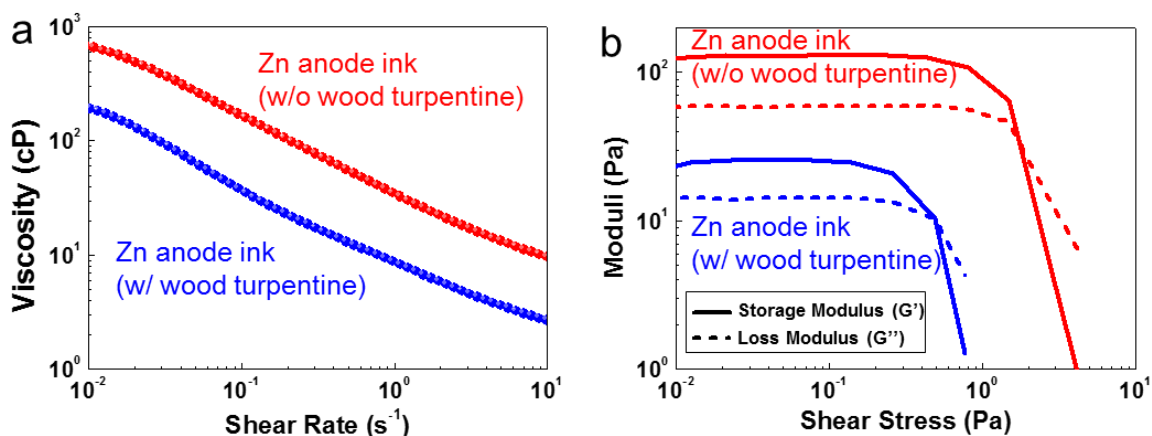
Figure 55. Effect of adding wood turpentine oil as a shear-thinning medium on the rheological properties of the Zn anode ink: (a) viscosity; (b) moduli (G', G'').
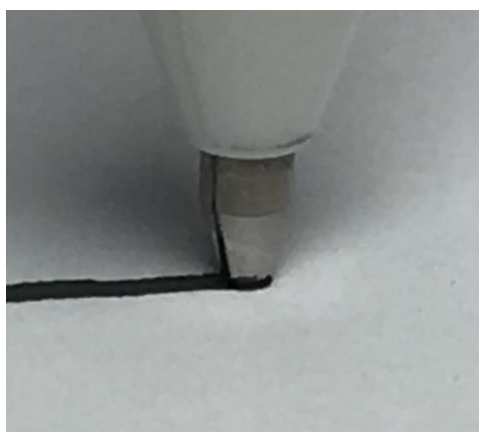

Figure 56. Photograph showing the dispersion stability of the Zn anode ink, where the pen writing was performed after a month when stored in a sealed container.

4.2.3.3. Direct-Writing and UV-Curing of Zn Anodes

As aforementioned before, the drying or curing of the linseed oil is the result of autoxidation, the addition of oxygen to an organic compound and the subsequent crosslinking[23-24]. This reaction initiates with an oxygen molecule in the air inserting into -C-H- bonds adjacent to one of the double bonds (-C=C-) within the unsaturated linolenic acid. The resulting hydroperoxides are susceptible to crosslinking reactions between neighboring linolenic acids, resulting in a polymer network. This polymerization results in elastic yet stable films that do not flow or deform readily. Compared to di- and tri-unsaturated linolenic acids, monounsaturated linolenic acids in the oil are sluggish to undergo curing, thus determining the rate of polymerization. The unreacted monounsaturated linolenic acids associated with the polymer network constitute the mobile phases. In the presence of the mobile phase,

the resulting Zn anodes can be easily damaged, which should be avoided in the on-the-fly power sources. The linseed oil, like some other drying oils, is known to be susceptible to crosslinking reactions in the presence of the ultraviolet (UV)[25]. Thus, we introduced the UV-curing of linseed oil to reduce the time scale of reaction kinetics, in which the UV irradiation enabled a substantial decrease in the curing time of linseed oil from a week to 10 min (Figure 57a).

The crosslinking reaction of linseed oil was monitored by measuring the fluorescence spectroscopy after the UV irradiation onto written Zn anodes was performed. The fluorescence spectroscopy can be an effective tool for identifying of crosslinking reaction in the linseed oil because it exhibits fluorescence under UV light after crosslinking reaction[26]. Before the UV irradiation, the Zn anode did not exhibit any fluorescence intensity within the measured wavelength range of 400 to 700 cm^{-1} (Figure 57b). In comparison, it was observed that the fluorescence intensity showing two peaks at 500 and 570 cm^{-1} gradually increased with the exposure time and finally reached a saturation point at 10 min, where the peaks are similar to that observed in the previous report[26]. Besides, the fluorescence mapping images revealed the large-scale uniformity of the crosslinking reaction as shown in Figure 57c. As a result, we demonstrate the UV-induced curing of the oil-based inks that can provide a simple yet effective route within a shorter period (up to 10 min).
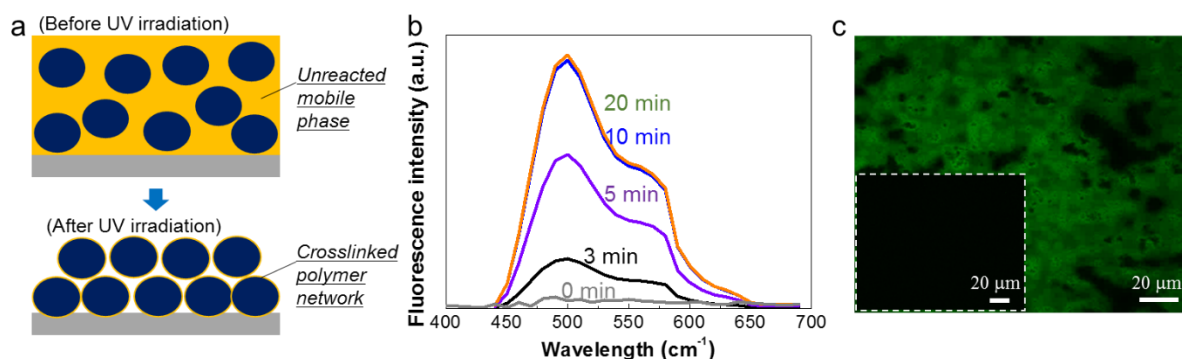

Figure 57. (a) Schematic illustration of UV-curing mechanism of the Zn anode after writing was performed, where the linseed oil is susceptible to crosslinking under UV irradiation. (b) Fluorescence spectra of the written Zn anodes as a function of UV irradiation time. (c) Fluorescence mapping images of the written Zn anodes before (see the inset) and after UV irradiation.

The resultant Zn anodes were successfully realized regarding exceptional dimensional integrity and chemical stability. Neither peel-off nor detachment of the Zn traces was found after the mechanical rubbing test by using an eraser (Figure 58a). Moreover, the Zn anode highly repelled the water (Figure 58b), due to the resulting hydrophobic polymer network after the UV irradiation. This water-repelling nature can protect the Zn anode even at harsh conditions. To investigate the chemical stability, the morphological changes of the Zn anodes were monitored for 10 hr under the high-humidity and high-temperature (at 95% RH, 80 °C) (Figure 58c,d). Notably, the UV-cured Zn anode

showed no appreciable change in the surface morphology, while the large amount of the crystalline ZnO was observed at the uncured Zn anode. These results demonstrate the UV-cured polymer network in the Zn anode can act as a multifunctional binder with the exceptional mechanical integrity and chemical stability.
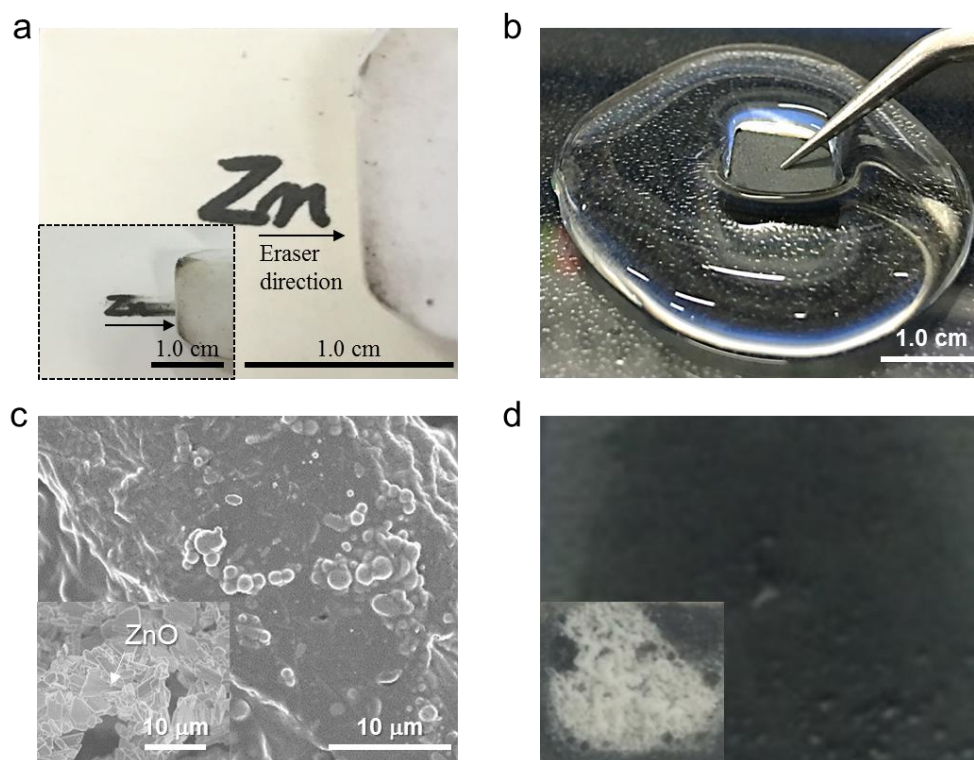

Figure 58. (a) The mechanical rubbing test of the written Zn anodes before (see the inset) and after UV irradiation. (b) Photograph showing the water-repelling nature of the written Zn anodes. (c, d) SEM images (c) and photographs (d) showing the variation in the surface morphology of the UV-cured Zn anode and the uncured Zn anode (see the insets) after the high-humidity and high-temperature test (at 95% RH/80 °C for 10 hr).

4.2.3.4. Electrochemical Characterization of Writable Zn-Air Batteries

The unique electrochemical properties of the writable Zn-air batteries appeared in **Figure 4**. The writable Zn-air batteries showed a well-defined voltage plateaus at around 1.2 V (Figure 59a), corresponding potentials of the electrochemical coupling of the Zn anode to the air cathode in the alkaline condition[18-19]. The specific capacity was ~ 600 mAh g^{-1} (the Zn mass ~ 8.3 mg cm^{-2}) and thus areal capacity of 5 mAh cm^{-2} at a discharge current density of 1.0 mA cm^{-2}. To underscore the superior air stability of the Zn anode (Figure 58b-d), we compared the electrochemical properties of the writable Zn-air batteries before/after exposure to ambient conditions for a month, where the gel electrolyte was applied just before the electrochemical measurement. Importantly, the writable Zn-air battery retained the electrochemical characteristics after the test, demonstrating an exceptional stability under ambient conditions. Besides, the mechanical flexibility was investigated as a function

of bending radii. Even at the bending radius of 2 mm, the writable Zn-air batteries retained their structural integrity without impairing the electrochemical characteristics (Figure 59b,c).
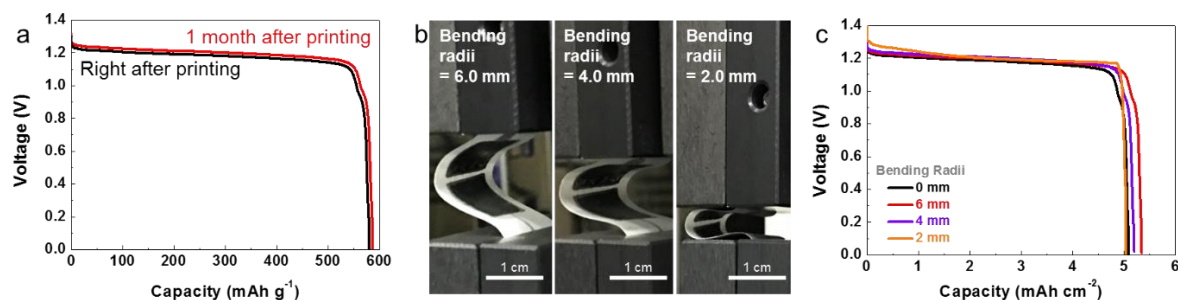

Figure 59. (a) Discharge profiles (current density = 1.0 mA cm^{-2}) of the writable Zn-air batteries before/after exposure to ambient conditions for a month. (b-c) The mechanical stability of the writable Zn-air batteries upon bending as a function of bending radii: (b) photographs; (c) discharge profiles at a discharge current density of 1.0 mA cm^{-2}.

One of the most appealing advantages of the direct-writable Zn-air batteries is the provision of design versatility. The direct-writable Zn-air batteries can be readily connected in series or parallel without the use of metallic interconnects (Figure 60). Compared to the single cell (~1.2 V and ~5 mAh), the 2-cells connected in series showed a 2-fold increase in voltage (~2.4 V), while the 2-cells connected in parallel showed a 2-fold increase in cell capacity (~10 mAh). This result demonstrates that the writable Zn-air batteries proposed herein allow the voltage and current of the resulting power sources to be easily controlled by simply writing batteries when needed.
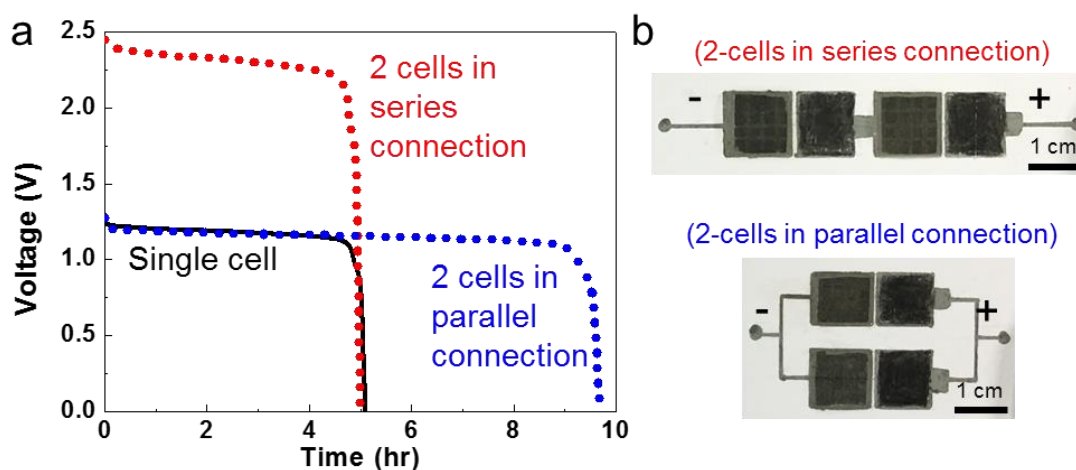

Figure 60. (a) Discharge profiles (current density = 1.0 mA cm^{-2}) of the writable Zn-air batteries connected in series or parallel. (b) Photographs of the writable Zn-air batteries: (top) 2-cells in series connection; (bottom) 2-cells in parallel connection.

To explore the feasibility of the practical implementation of the writable Zn-air batteries, their power and energy density were investigated. Figure 61a shows the output power of the writable Zn-air

battery as a function of discharge current densities (1.0, 2.0, 5.0, and 10.0 mA cm^{-2}). At the highest current density of 10.0 mA cm^{-2}, the writable Zn-air battery delivered the output power density of ~4.5 mW cm^{-2}, which is higher than those required to operate computer-sensor devices for the IoT[27]. Moreover, the areal mass of the writable Zn-air battery was ~21 mg cm^{-2} for the whole battery components including the paper substrate, thus the writable Zn-air battery exhibited a notable specific energy of ~284 Wh kg^{-1}, which is much higher than those of other conventional power sources[19] that require packaging substances (Figure 61b).

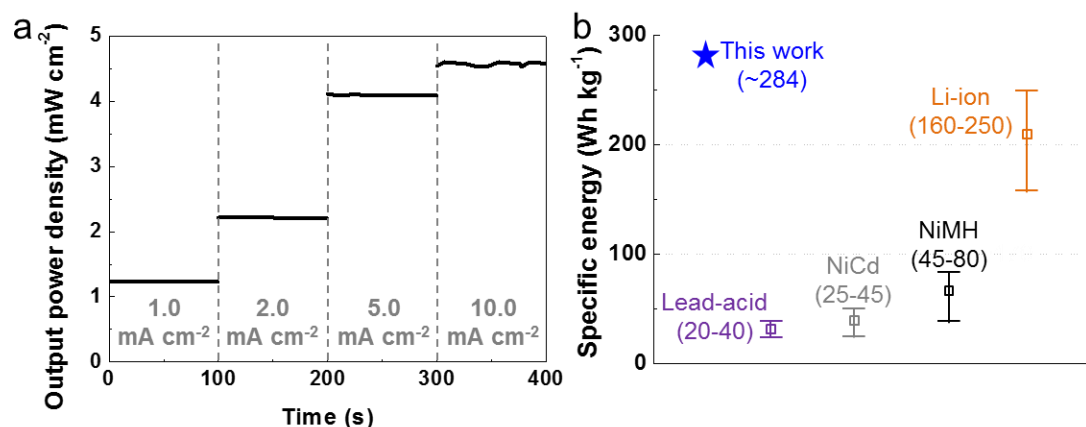**Figure 61.** (a) Output power densities of the writable Zn-air batteries as a function of discharge current densities from 1.0 to 10.0 mA cm^{-2}. (b) The specific energy of the writable Zn-air batteries was compared to those of other conventional power sources[19].

4.2.3.5.   Aesthetic Versatility of Writable Zn-Air Batteries as On-The-Fly Power Sources for IoT Applications

To demonstrate the device fabrication capabilities afforded the writable Zn-air batteries, we produced electronic artworks and IoT devices on paper substrates by using rollerball pens and other office supplies. As an example, an electronic sketch of the light bulb was drawn on A4 paper (Figure 62a). The background sketch was first drawn. The writable Zn-air batteries in 2-series connection were drawn on the sketch and then connected with the printed circuit. The writable Zn-air batteries in the sketch exhibited a normal discharge profile showing a voltage of ~1.2 V and a capacity of ~0.95 mAh (Figure 62b), eventually powering a LED lamp mounted on the circuit.
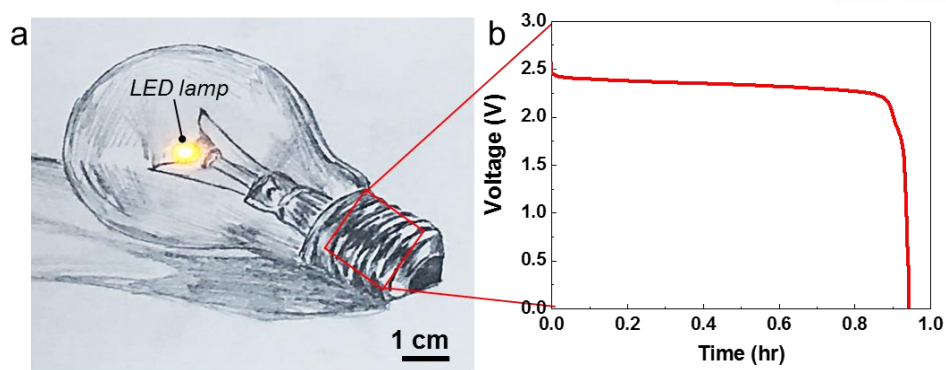
Figure 62. (a) Photograph of the electronic sketch of the light bulb, wherein the writable Zn-air batteries in 2-series connection (marked by a red box) were connected to a LED lamp via direct writing. (b) Discharge profile (current density = 1.0 mA cm^{-2}) of the 2-series connected Zn-air batteries in the electronic sketch.

To highlight the unique functions of the writable Zn-air batteries as on-the-fly power sources for the IoT, we fabricated a smart paper lamp that can respond to the illumination intensity stimuli. Specifically, electrical components, which include a transistor, illumination sensor, and a LED lamp, were embedded in the kirigami paper with pre-designed cuts and then connected via a silver pen. On the circuit-embedded kirigami paper, the writable Zn-air batteries in 3-series connection were drawn to yield the device-integrated kirigami paper (Figure 63a), where the batteries delivered a voltage of ~3.5 V and a capacity of ~4.8 mAh (Figure 63b). The smart lamp was successfully fabricated by transforming the device-integrated kirigami paper into the pre-designed 3D architecture without impairing the structural defects (Figure 63c), because the integrated device is flexible and light in weight. In contrast, the smart paper lamp cannot support its 3D structure when applying a conventional AAA-sized battery due to the higher mass, compared to that of the writable Zn-air batteries. Notably, the smart paper lamp was off in the presence of the light illumination (Figure 64d), while it started to operate in the absence of the light illumination. These results underline the exceptional applicability of the writable Zn-air batteries as the on-the-fly power sources.
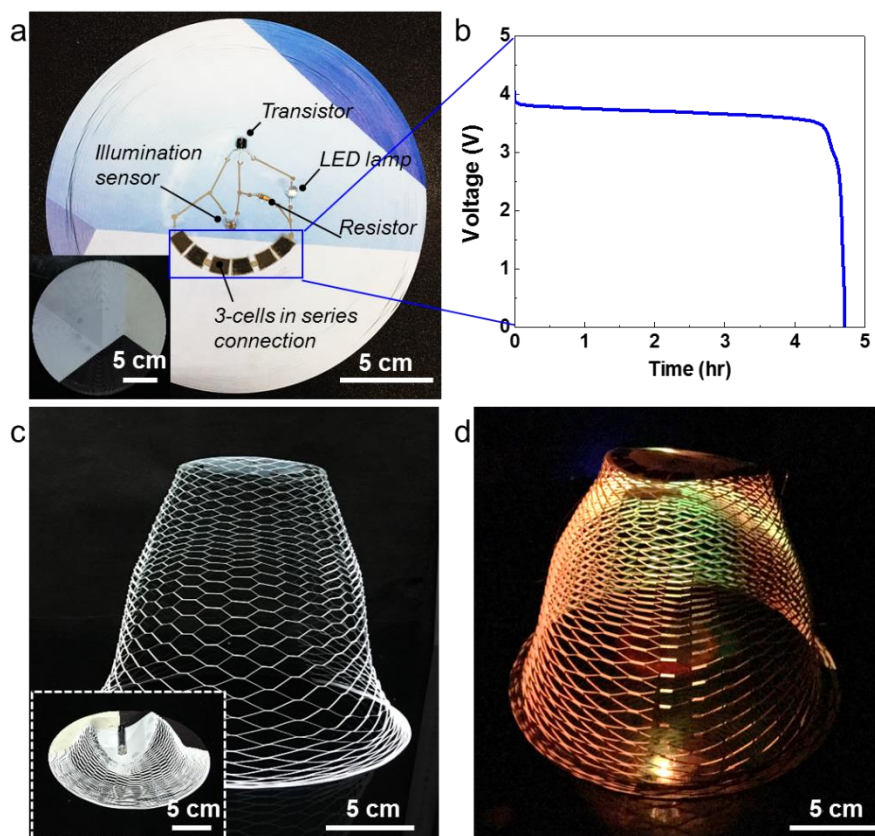
Figure 63. (a) Photographs depicting the light sensing circuit integrated with the 3-series connected Zn-air batteries on the kirigami paper, where the inset is the opposite side; it does show a seamless integration of electrical components with the kirigami paper. (b) Discharge profile (current density = 1.0 mA cm^{-2}) of the 3-series connected Zn-air batteries in the kirigami paper. (c) Photographs depicting the smart paper lamp that was off in the present of light. The kirigami paper integrated with the circuit was successfully transformed into the pre-designed 3D architecture to produce the smart paper lamp, while the inset shows that the paper cannot support its 3D structure when applying a conventional AAA-sized battery due to its higher mass. (d) Photograph depicting the operation of the smart paper lamp in the absence of the light illumination.

4.2.4. Conclusion

In summary, we demonstrated the direct-writable Zn-air batteries as on-the-fly power sources that can be fabricated on-site and on-demand under ambient conditions. The oil painting-inspired Zn ink chemistry enabled the simple deposition method of metallic Zn tracks via the pen writing technique, thus facilitating the rapid prototyping of the Zn-air batteries with exceptionally structural integrity. The writable Zn-air batteries acted as a power generator to deliver the useful power density ($\sim$4.5 mW cm^{-2} at 10 mA cm^{-2}). Notably, the Zn-air batteries can be easily connected in series or parallel, leading to user-customized control of power and energy density. To demonstrate the device fabrication capabilities, the writable Zn-air batteries were integrated with the printed electrical circuits, eventually powering the devices (e.g., an electronic sketch and smart paper lamp). Therefore, we envision that this approach offers a low-cost, portable fabrication route for the practical implementation of printed electronics and IoT devices.

4.2.5. References

(1) Y. Zhang, F. Zhang, Z. Yan, Q. Ma, X. Li, Y. Huang, J. A. Rogers, *Nat. Rev. Mater.* **2017**, *2*, 17019.

(2) D. Akinwande, *Nat. Nanotechnol.* **2017**, *12*, 287-288.

(3) A. G. Kelly, T. Hallam, C. Backes, A. Harvey, A. S. Esmaeily, I. Godwin, J. Coelho, V. Nicolosi, J. Lauth, A. Kulkarni, S. Kinge, L. D. A. Siebbeles, G. S. Duesberg, J. N. Coleman, *Science* **2017**, *356*, 69-73.

(4) K. Fu, Y. Yao, J. Dai, L. Hu, *Adv. Mater.* **2017**, *29*.

(5) R. L. Truby, J. A. Lewis, *Nature* **2016**, *540*, 371-378.

(6) Z. Li, H. Liu, C. Ouyang, W. Hong Wee, X. Cui, T. Jian Lu, B. Pingguan-Murphy, F. Li, F. Xu, *Adv. Funct. Mater.* **2016**, *26*, 165-180.

(7) A. Russo, B. Y. Ahn, J. J. Adams, E. B. Duoss, J. T. Bernhard, J. A. Lewis, *Adv. Mater.* **2011**, *23*, 3426-3430.

(8) A. J. Bandodkar, W. Jia, J. Ramirez, J. Wang, *Adv. Healthcare Mater.* **2015**, *4*, 1215-1224.

(9) N. Singh, C. Galande, A. Miranda, A. Mathkar, W. Gao, A. L. Reddy, A. Vlad, P. M. Ajayan, *Sci. Rep.* **2012**, *2*, 481-485.

(10) M. Kaempgen, C. K. Chan, J. Ma, Y. Cui, G. Gruner, *Nano Lett.* **2009**, *9*, 1872-1876.

(11) R. Kumar, J. Shin, L. Yin, J.-M. You, Y. S. Meng, J. Wang, *Adv. Energy Mater.* **2017**, *7*, 1602096.

(12) Y. Xu, M. G. Schwab, A. J. Strudwick, I. Hennig, X. Feng, Z. Wu, K. Müllen, *Adv. Energy Mater.* **2013**, *3*, 1035-1040.

(13) S. Suren, S. Kheawhom, *J. Electrochem. Soc.* **2016**, *163*, A846-A850.

(14) K.-H. Choi, J. Yoo, C. K. Lee, S.-Y. Lee, *Energy Environ. Sci.* **2016**, *9*, 2812-2821.

(15) K. Sun, T. S. Wei, B. Y. Ahn, J. Y. Seo, S. J. Dillon, J. A. Lewis, *Adv. Mater.* **2013**, *25*, 4539-4543.

(16) K. Fu, Y. Wang, C. Yan, Y. Yao, Y. Chen, J. Dai, S. Lacey, Y. Wang, J. Wan, T. Li, Z. Wang, Y. Xu, L. Hu, *Adv. Mater.* **2016**, *28*, 2587-2594.

(17) Y. Wang, H. Zhou, *Energy Environ. Sci.* **2011**, *4*, 1704.

(18) J. Fu, Z. P. Cano, M. G. Park, A. Yu, M. Fowler, Z. Chen, *Adv. Mater.* **2017**, *29*.

(19) J.-S. Lee, S. Tai Kim, R. Cao, N.-S. Choi, M. Liu, K. T. Lee, J. Cho, *Adv. Energy Mater.* **2011**, *1*, 34-50.

(20) J. Chen, F. Cheng, *Acc. Chem. Res.* **2009**, *42*, 713-723.

(21) M. N. Masri, A. A. Mohamad, *J. Electrochem. Soc.* **2013**, *160*, A715-A721.

(22) R. Shivkumar, G. P. Kalaignan, T. Vasudevan, *J. Power Sources* **1995**, *55*, 53-62.

(23) J. Mallegol, J. Lemaire, J. Gardette, *Prog. Org. Coat.* **2000**, *39*, 107-113.

(24) N. A. Porter, S. E. Caldwell, K. A. Mills, *Mechanisms of free radical oxidation of unsaturated lipids, Vol. 30*, Springer, **1995**.

(25) S. Boyatzis, E. Ioakimoglou, P. Argitis, *J. Appl. Polym. Sci.* **2002**, *84*, 936-949.

(26) E. Rie, *Fluorescence of paint and varnish layers (Part II), Vol. 27*, Taylor & Francis, Ltd., **1982**.

(27) R. Haight, W. Haensch, D. Friedmand, *Science* **2016**, *353*, 124-125.